Analytical and Experimental Studies of Plant-Flow Interaction at Multiple Scales

by

Mitul Luhar

B.A., M.Eng., Cambridge University (2007)

Submitted to the Department of Civil and Environmental Engineering
in partial fulfillment of the requirements for the degree of

Doctor of Philosophy

at the

MASSACHUSETTS INSTITUTE OF TECHNOLOGY

September 2012

Author .....
Department of Civil and Environmental Engineering
July 5, 2012

Certified by .....
Heidi M. Nepf
Professor, MacVicar Faculty Fellow
Thesis Supervisor

Accepted by .....
Heidi M. Nepf
Chair, Departmental Committee for Graduate Students

Analytical and Experimental Studies of Plant-Flow Interaction at Multiple Scales

by

Mitul Luhar

Submitted to the Department of Civil and Environmental Engineering
on July 5, 2012, in partial fulfillment of the
requirements for the degree of
Doctor of Philosophy

Abstract

Across scales ranging from individual blades to river reaches, the interaction between water flow and vegetation has important ecological and engineering implications. At the reach-scale, vegetation is often the largest source of hydraulic resistance. Based on a simple momentum balance, we show that the resistance produced by vegetation depends primarily on the fraction of the channel cross-section blocked by vegetation. For the same blockage, the specific distribution of vegetation also plays a role; a large number of small patches generates more resistance than a single large patch.

At the patch-scale, velocity and turbulence levels within the canopy set water renewal and sediment resuspension. We consider both steady currents and wave-induced flows. For steady flows, the flow structure is significantly affected by canopy density. We define sparse and dense canopies based on the relative contribution of turbulent stress and canopy drag to the momentum balance. Within sparse canopies, velocity and turbulent stress remain elevated and the rate of sediment suspension is comparable to that in unvegetated regions. Within dense canopies, velocity and turbulent stress are reduced by canopy drag, and the rate of sediment resuspension is lower. Unlike steady flows, wave-induced oscillatory flows are not significantly damped within vegetated canopies. Further, our laboratory and field measurements show that, despite being driven by a purely oscillatory flow, a mean current in the direction of wave propagation is generated within the canopy. This mean current is forced by a wave stress, similar to the streaming observed in wave boundary layers.

At the blade-scale, plant-flow interaction sets posture and drag. Through laboratory experiments and numerical simulations, we show that posture is set by a balance between the hydrodynamic forcing and the restoring forces due to blade stiffness and buoyancy. When the hydrodynamic forcing is small compared to the restoring forces, the blades remain upright in flow and a standard quadratic law predicts the relationship between drag and velocity. When the hydrodynamic forcing exceeds the restoring forces, the blades are pushed over in steady flow, and move with oscillatory flow. For this limit, we develop new scaling laws that link drag with velocity.

Thesis Supervisor: Heidi M. Nepf
Title: Professor, MacVicar Faculty Fellow

Acknowledgments

First and foremost, I would like to thank my advisor, Heidi Nepf, for her guidance, patience, and support over the past five years. As a research mentor, Heidi has been an incredible resource: knowledgeable, creative, and generous with her time and expertise. As a teacher, Heidi has been a fantastic role model. Thanks must also go to members of my thesis committee, Roman Stocker and Chiang Mei, for their questions, advice, and critical insights into my work. At times, Roman has been a wonderfully approachable and enthusiastic auxiliary research mentor too.

I would also like to express my gratitude to Nepf lab colleagues for equipment tutorials, experimental advice, and help in the laboratory: Yukie Tanino, Kevin Zhang, Jeff Rominger, Sylvain Coutu, Eduardo Infantes, Aleja Ortiz, and Elizabeth Finn. Assistance provided by Tiffany Cheng, Samantha Fox, and Columbus Leonard, through the MIT undergraduate research opportunities program was invaluable. Further, the broader Environmental Fluid Mechanics group (including the Adams, Madsen, and Stocker labs) was a fantastic sounding board for ideas.

Outside of research, my time at MIT has been immensely enjoyable, and a lot of the credit must go to the wider Parsons community. Parsons is a truly supportive and inspiring place, and I have been lucky enough to call many Parsons lab members (past and present) friends. Finally, I am immensely thankful to my parents and brother for their steady encouragement, and to my lovely wife, Aarti, for her patient support.

Financial support from MIT (Presidential Fellowship, Teaching Assistantship), the Martin Family Foundation, and National Science Foundation grant OCE 0751358 is gratefully acknowledged.

THIS PAGE INTENTIONALLY LEFT BLANK

Contents

List of Figures

THIS PAGE INTENTIONALLY LEFT BLANK

List of Tables

THIS PAGE INTENTIONALLY LEFT BLANK

Chapter 1

Introduction

Historically, aquatic vegetation was viewed as little more than a source of hydraulic resistance that exacerbated flooding and impeded the transport of potable and irrigation water [19, 50]. As a result, it was often removed entirely from river channels, streams, and canals. It is now recognized that aquatic vegetation provides important ecological services that make it a vital part of freshwater and coastal ecosystems. By creating regions of low flow, aquatic vegetation provides habitat for economically important fish and shellfish [46], reduces sediment suspension [4], and stabilizes the substrate [94]. By taking up excess nutrients from the water and producing oxygen, vegetation improves water quality [11]. In coastal zones, mangrove forests, seagrass beds, and salt marshes offer vital protection by dissipating wave energy [8].

Some of the ecosystem services mentioned above (e.g., stabilizing the substrate, providing habitat, dissipating wave energy) arise because the presence of the vegetation canopy changes the local flow conditions [7]. Others, such as nutrient cycling and oxygen production, are mediated by the rate of mass transfer between the canopy and the surrounding water [49]. At the scale of individual blades, hydrodynamic forces dictate plant posture, which influences light availability [105]. An upright posture exposes the vegetation to higher light intensities, whereas a streamlined posture increases the projected leaf area absorbing the incoming light but makes self-shading among neighboring plants more likely. Posture can also control nutrient [42] and oxygen [63] exchange between the vegetation and the surrounding water. Faster flows

perpendicular to the vegetation lead to thinner diffusive boundary layers around the vegetation, which enhances nutrient and oxygen transfer. Finally, excessive hydrodynamic forces can lead to stem rupture [19] or dislodgement from the substrate [85].

Because of its importance to flood and ecosystem management, the interaction between water flow and aquatic vegetation has received significant attention recently [74]. Previous studies have successfully described fully developed, steady flow through submerged (see e.g., [32, 33, 34, 35]) and emergent (see e.g., [52, 95, 100]) canopies of vegetation. Yet, many important gaps in our knowledge remain. Despite the fact that predicting vegetation resistance is of vital importance to effective flood management, little of the physical understanding gleaned from the canopy-scale work has been transferred to reach-scale field studies. Field studies have focused primarily on developing empirical relationships linking friction coefficients such as Manning's n_M with vegetation properties such as blockage (i.e., the fraction of the channel cross-section blocked by vegetation, e.g., [38, 75]) and biomass (e.g., [17, 18]). For coastal habitats such as seagrass beds, which are some of the most valuable [11] natural systems in the world, waves rather than currents are the dominant hydrodynamic forcing. However, unsteady wave-induced flows through vegetated canopies are not very well described. Finally, most aquatic plants are flexible, which means that they are pushed over (reconfigured) by steady currents, and move in response to wave-induced oscillatory flows [98]. Relative to rigid vegetation, this leads to a reduction in the hydrodynamic forces generated. However, the behavior of flexible plants in steady and oscillatory flows is not well understood. In fact, the drag generated by flexible plants has been the subject of significant recent debate [87]. Through a series of experimental and analytical studies, we address these open questions.

1.1 Outline

In §2, we describe steady flows through aquatic vegetation, at the scale of individual canopies or patches, and at the scale of entire river reaches. We discuss the impact of vegetation density on the flow structure and sediment suspension, and develop a sim-

ple two-layer momentum balance model to predict the flow rate through submerged canopies. We also extend this simplified momentum balance model for application at the reach-scale. We use this model to consider the effect of vegetation patchiness (i.e., number of individual patches across the channel cross-section) on flow, and to yield estimates for hydraulic resistance in the field. Note that most of §2 is derived from the publication Luhar and Nepf (2012) [57]. However, we also include excerpts from Luhar et al. (2008) [59].

§3 describes laboratory and field studies investigating the wave-induced flow structure within seagrass beds. The laboratory study, published as Luhar et al. (2010) [56], employed flexible model vegetation, scaled to be dynamically similar to real seagrasses. The field study was carried out in Cala Millor, located on the eastern coast of Mallorca Island in the Mediterranean Sea. Our measurements reveal that a mean current is generated within the seagrass canopies, similar to the streaming observed in wave boundary layers. To predict the magnitude of this streaming velocity, we develop a simple momentum- and energy-balance model. Further, we also investigate the degree to which wave-induced oscillatory flow is reduced within canopies of vegetation.

In §4, we characterize the drag generated by flexible aquatic vegetation in steady, uniform flow. We develop a model that calculates vegetation posture based on a force balance involving vegetation stiffness, buoyancy, and the hydrodynamic forcing. For simplicity, we develop the model for individual blades with rectangular cross-sections, characteristic of seagrasses. However, we show that this model is able to predict posture and drag for laboratory experiments with model blades, as well as real seagrasses, and marine macroalgae of more complex morphology. Finally, to study the effect of vegetation reconfiguration on flow resistance, we extend the two-layer model developed in §2 to account for plant flexibility. The majority of this chapter is published as Luhar and Nepf (2011) [58].

§5 describes the motion of flexible blades in wave-induced oscillatory flows. We extend the blade reconfiguration model developed in §4 to account for time-varying flow, and unsteady hydrodynamic forces. In general, this model adequately repro-

duces the observed blade motion and measured hydrodynamic forces for laboratory experiments with model blades (§5.2). Interestingly, our experiments show that in some cases, the force generated by flexible blades can be greater than that expected for rigid blades. Finally, in §6, we provide a brief summary of our findings, and discuss possible environmental and engineering implications.

Chapter 2

Steady flows through aquatic vegetation

This chapter describes steady flows through aquatic vegetation, at the scale of individual canopies or patches, and at the scale of entire river reaches. In §2.1, we discuss the impact of vegetation density on flow structure and sediment suspension, and develop a simple two-layer momentum balance model that predicts the flow rate through submerged canopies. In §2.2, we extend this simplified momentum balance model for application at the reach-scale. We use this model to consider the effect of vegetation patchiness (i.e., number of individual patches across the channel cross-section) on flow, and to yield estimates for hydraulic resistance in the field. Except §2.1.2, all of this chapter appears in Luhar and Nepf (2012) [57]. §2.1.2 is an excerpt from Luhar et al. (2008) [59].

2.1 Flow at the canopy-scale

2.1.1 Canopy architecture and momentum balance

Aquatic vegetation most often exists in canopies or meadows, i.e., close groupings of individual plants. To understand stem-scale processes, such as flux across the boundary layer of an individual leaf, one must parametrize the morphology of the leaf.

However, at the scale of an entire canopy, the complex morphology of individual plants is less important and the vegetation can be characterized by an average parameter: the frontal area per unit volume, a. When the vegetation has a blade-like morphology, the frontal area per unit volume is $a = nb$, where n is the number of blades per unit bed area, and b is the blade width. The parameter a can only be defined over a horizontal scale larger than several blade spacings. So, using this representation for the canopy, we cannot resolve the flow at scales smaller than several blade spacings. Within the canopy, the solid volume fraction occupied by the vegetation is $\phi = ad$ where d is the blade thickness. For steady, uniform flows through porous ($\phi \ll 1$) canopies, the following simplified momentum balance applies [59]:

$$0 = \rho g S + \frac{\partial \tau}{\partial z} - 1/2 \rho C_D a |u| u \tag{2.1}$$

Here, ρ is the water density, the slope $S = \partial(H + z_b)/\partial x$ is the gradient in water depth, H, and bed elevation, z_b, in the streamwise (x) direction, τ is the turbulent shear stress, C_D is the drag coefficient for the vegetation, and $u(z)$ is the streamwise velocity. The coordinate z is normal to the bed, and g is the acceleration due to gravity.

For the case where the vegetation is submerged (canopy height smaller than water depth, $h < H$), the momentum balance above the patch can be expressed at $\rho g S + \partial \tau / \partial z = 0$. This momentum balance is identical to that for turbulent flows over rough boundaries, for which the velocity profile is described by the well known logarithmic law of the wall. Given the poor scale separation between plant height and flow depth, it is unlikely that a genuine logarithmic layer exists in aquatic flows over vegetation. However, previous studies (e.g., [59, 76, 66]) have shown that a modified logarithmic profile provides a reasonable description of the velocity field above the canopy:

$$u(z) = \frac{u^*}{\kappa} \ln \left(\frac{z - z_m}{z_0} \right) \tag{2.2}$$

Here, $u^* = \sqrt{gS(H - z_m)}$ is the friction velocity and $\kappa = 0.4$ is the von Karman constant, while z_m and z_0 are the displacement and roughness heights, respectively. The

displacement height, $z_m = h - \delta$, depends on the length scale, δ, over which turbulent stresses penetrate into the canopy. Scaling analyses and experimental observations suggest that this penetration scale is inversely proportional to the canopy drag, with $\delta \approx 0.1(C_D a)^{-1}$ [71]. In general, the parameter $(C_D a)^{-1}$ represents the length scale over which any momentum transferred into the canopy is dissipated by drag. For submerged canopies, the length scale δ splits the canopy into two zones. Turbulent momentum and mass transfer are important in the upper region of the canopy, i.e., for $(h - \delta) < z < h$. However, for $z < (h - \delta)$, the turbulent stress term in Eq. 2.1 can be assumed negligible, and so the velocity is:

$$u = \sqrt{\frac{2gS}{C_D a}} \tag{2.3}$$

Lightbody and Nepf [52] show that turbulent stresses can also be neglected for dense patches of emergent vegetation (i.e., $h \geq H$), for which case Eq. 2.3 successfully describes the flow field over the entire water depth.

2.1.2 Sparse versus dense canopies

If the canopy is sparse enough such that the length scale of turbulence penetration is approximately equal to the canopy height, $\delta \approx 0.1(C_D a)^{-1} \approx h$, the displacement height for the logarithmic overflow becomes $z_m = h - \delta \approx 0$. At this limit, where $C_D a h \leq 0.1$, the entire flow resembles a turbulent boundary layer (see Fig. 2-1). This is often referred to as sparse canopy behavior (see e.g., [72]). For dense canopies, with $C_D a h > 0.1$, the drag discontinuity at the top of the canopy creates an inflection point in the velocity profile. This inflection point leads to the generation of large, coherent vortices via the Kelvin-Helmholtz instability [77], which dominate mass and momentum exchange between the canopy and the overlying water (e.g., [22, 32, 35]). Indeed, the length scale δ is set by the distance to which these coherent structures penetrate into the canopy (see Fig. 2-1).

Although the drag coefficient, C_D, varies with flow and morphology, it is typically of $O(1)$. Therefore, the transition between sparse and dense canopies can be taken at

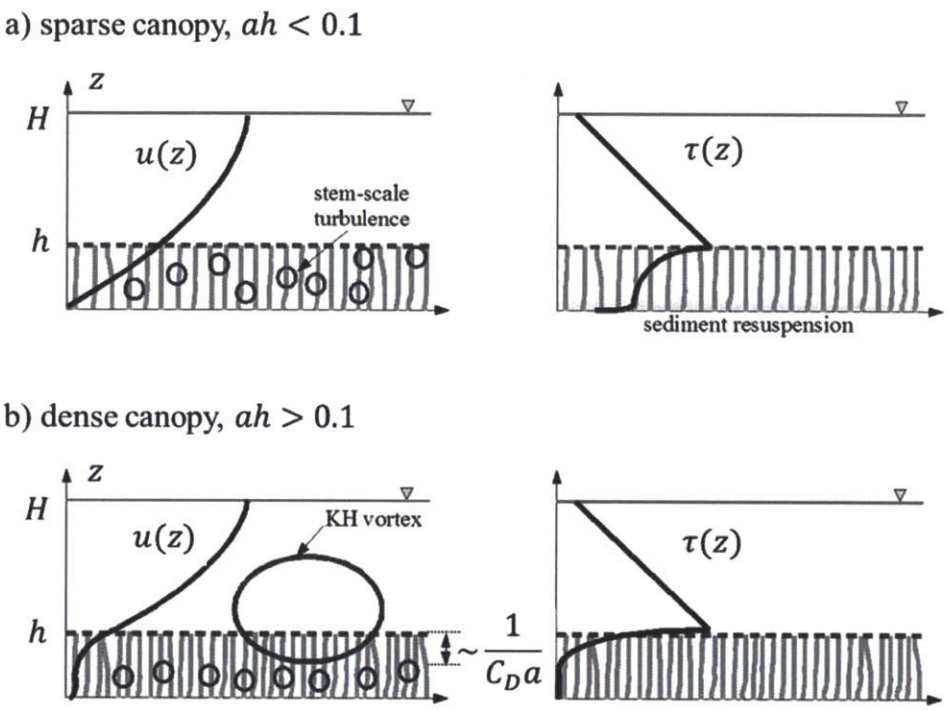

Figure 2-1: Flow within and above a submerged canopy. Profiles of mean velocity and turbulent stress are shown. (a) For a sparse canopy, the profile resembles a turbulent boundary layer, and the turbulent stress remains elevated at the bed. (b) For a dense canopy, an inflection point at the top of the canopy generates vortices via the Kelvin-Helmholtz (KH) instability. The turbulent stress near the bed is significantly reduced due to canopy drag.

$ah \approx 0.1$. Note that this parameter is essentially the frontal area per unit bed area for the vegetation canopy. In sparse canopies, we expect turbulence and turbulent stress to remain elevated close to the bed, whereas in dense canopies turbulence and turbulent stress near the bed are reduced due to canopy drag. Because the turbulent shear stress near the bed dictates sediment resuspension, we anticipate lower resuspension and reduced suspended sediment concentration within dense canopies (see Fig. 2-1). Observations from Moore (2004) [69] support this conjecture. Moore [69] investigated the influence of the seagrass *Zostera marina* on water quality by contrasting vegetated and unvegetated sites within the Lower Chesapeake Bay. His observations suggested that the difference in total suspended solids (TSS) inside and outside the grass beds, ΔTSS, depended on seagrass biomass. Further, he noted that the difference in TSS between the vegetated and unvegetated sites was negligible when the average aboveground biomass per unit area was less than 100 g m^{-2} (dry mass). The dry mass measure can be converted to frontal area index using:

$$Biomass/m^2 = \rho_v ahd \tag{2.4}$$

For Zostera Marina the characteristic blade thickness is $d = 0.3 \pm 0.05$mm [21], and the material density is $\rho_v \approx 760$ kg m^{-3} [23]. The difference in TSS between vegetated and unvegetated sites can now be considered in the context of the transition in flow structure described by Fig. 2-1. The threshold noted by Moore [69], 100 g m^{-2}, corresponds to $ah = 0.4$. A significant drop in TSS is observed for canopies with ah greater than this value (see Fig. 2-2). Thus, the observed transition in TSS is consistent with the transition threshold predicted from the momentum balance. Specifically, when $ah \geq 0.1$, the turbulent stress cannot penetrate close enough to the bed to generate sediment resuspension. Above this density, a meadow promotes sediment retention, thereby stabilizing the bed and improving light conditions. These two feedbacks may promote meadow survival. Conversely, a reduction in canopy density below this threshold sets off a negative feedback, with increased sediment resuspension leading to a loss of bed stability and a reduction in light availability,

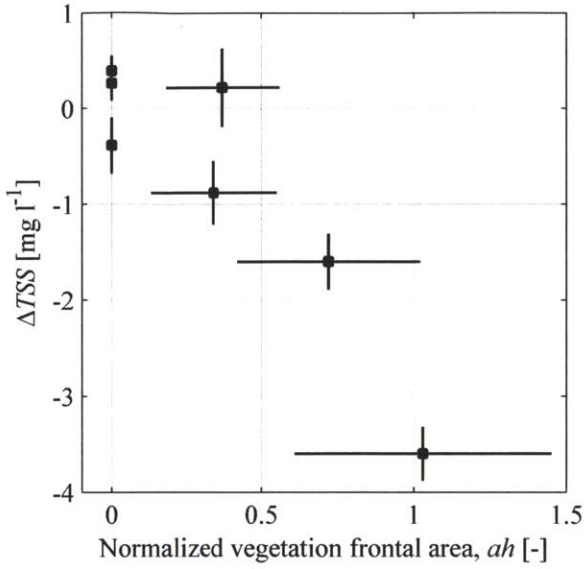

Figure 2-2: Difference in total suspended solids (TSS) between vegetated and unvegetated locations. The data is from [69]; Eq. 2.4 is used to convert the reported dry mass values to frontal area. Note that $ah = 0$ corresponds to an inshore site with no vegetation.

both of which can lead to further canopy deterioration.

2.1.3 A simple two-layer momentum balance

To develop a two-layer model, we integrate Eq. 2.1 over z assuming constant (i.e., vertically-averaged) velocities U_o and U_v in the in the overflow ($h < z < H$) and vegetated ($0 < z < h$) layers, respectively. Further, we assume that there is no shear stress at the water surface. This yields the following physically intuitive momentum balances for the overflow and for the patch:

$$0 = \rho g S(H - h) - \tau_h \tag{2.5}$$

$$0 = \rho g S h + \tau_h - \tau_b - (1/2)\rho C_D a h {U_v}^2 \tag{2.6}$$

In Eq. 2.5 and Eq. 2.6, τ_h is the shear stress at the interface between the patch and the overflow, τ_b is the bed stress. Strictly, with this two-layer formulation, the friction velocity is $u^* = \sqrt{\tau_h/\rho} = \sqrt{gS(H-h)}$, which is not consistent with the form

shown earlier ($u^* = \sqrt{gS(H - z_m)}$, see Eq. 2.2). In essence, the following additional assumption is being made: the canopy is dense enough such that $\delta \approx 0.1(C_D a)^{-1} \ll h$, and so the displacement height for the logarithmic profile is $z_m = h - \delta \approx h$. To arrive at estimates of U_o and U_v, appropriate parameterizations for the interfacial stress and bed stress are required. We employ constant friction coefficients at the interface, C_v, and at the bed, C_f, such that $\tau_h = (1/2)\rho C_v {U_o}^2$ and $\tau_b = (1/2)\rho C_f {U_v}^2$. This expression for τ_h is appropriate when the velocity within the patch is much smaller than the overflow velocity, i.e., $U_v \ll U_o$. However, as discussed above, for sparse vegetation the in-patch velocity is likely to be comparable to the overflow velocity, and so the shear stress will depend on the difference, i.e., $\tau_h = (1/2)\rho C_v (U_o - U_v)^2$. If the canopy is sparse enough such that the length scale of turbulence penetration is approximately equal to the patch height, $\delta \approx 0.1(C_D a)^{-1} \approx h$, the entire flow resembles a turbulent boundary layer, and the two-layer assumption breaks down.

The stress parameterizations discussed above yield the following expressions for the overflow and in-patch velocities:

$$U_o = \left(\frac{2gS(H - h)}{C_v} \right)^{1/2} \tag{2.7}$$

$$U_v = \left(\frac{2gSh + C_v {U_o}^2}{C_D a h + C_f} \right)^{1/2} = \left(\frac{2gSH}{C_D a h + C_f} \right)^{1/2} \tag{2.8}$$

The depth-averaged velocity is:

$$U_T = \frac{U_o(H - h) + U_v h}{H} \tag{2.9}$$

Cheng [10] uses a similar approach to predict the flow through submerged vegetation, but assumes that the interfacial friction factor $f_s (= 4C_v)$ varies with vegetation properties. Such an assumption is reasonable physically; however, the laboratory data aggregated by Cheng [10] show only a weak relationship between f_s and vegetation properties. Similarly, Murphy et al. [70] show that the interfacial friction coefficient is not a strong function of either meadow density or depth of submergence for $H/h > 2$. As a simpler alternative, we employ a constant friction coefficient,

$C_v = 0.04$ ($f_s = 0.16$), which is in the middle of the range ($f_s \approx 0.02 - 0.5$ or $C_v \approx 0.005 - 0.13$) suggested by Cheng. Huthoff et al. [43], also use a similar framework to the one described here. However, they allow C_v to vary as a function of the submergence ratio, H/h, to ensure physically reasonable behavior at the limit of emergent vegetation. For constant C_v, Eq. 2.7 predicts that $U_o \to 0$ as $h \to H$, which is not realistic as one would expect that $U_o \geq U_v$, even if the overflow is very shallow.

Despite these simplifications, Fig. 2-3 shows that the two-layer model described by Eq. 2.7-2.9, with $C_v = 0.04$, predicts depth-averaged velocities well for multiple sets of laboratory experiments measuring flow through submerged patches of vegetation (data aggregated by [10]). Note that, to arrive at the predicted velocities shown in Fig. 2-3, we made a few additional assumptions. Specifically, the laboratory experiments employed rigid cylinders, and so we assumed that the height of the vegetated layer is equal to cylinder length, $h = l$, and that $a = nd_c$, where n is the number of cylinders per unit bed area and d_c is the cylinder diameter. Further, we used the well-known drag coefficient for cylinders, $C_D = 1$. We also assumed that vegetation drag is the dominant momentum sink within the patch and so the bed stress may be neglected, $C_f \ll C_D ah$, such that Eq. 2.8 simplifies further to $U_v = [(2gSH)/(C_D ah)]^{1/2}$. This assumption is justified because typically $C_D ah > O(0.1)$ for the laboratory experiments, while we expect that $C_f \sim O(0.01)$ for the relatively smooth beds characteristic of laboratory flumes. The data collected by Poggi et al. [76], for which $C_D ah < 0.1$, notably deviates from the line of good fit. As discussed above, at this sparse vegetation limit, the entire flow resembles a turbulent boundary layer and the two layer model described by Eq. 2.7-2.9 is inappropriate.

Eq. 2.5-2.9 are valid for both rigid and flexible vegetation, assuming that the vegetation frontal area per unit volume, a, and canopy height, h, are known. For rigid vegetation, a and h are constants but for flexible vegetation, which can be pushed over by the flow, a and h vary with the canopy velocity, U_v. Having shown that the model developed above successfully predicts velocities for patches of rigid vegetation where $C_D ah \geq 0.1$, we apply it to patches of flexible vegetation in §4.4.2, by explicitly accounting for changes in drag and canopy height with velocity.

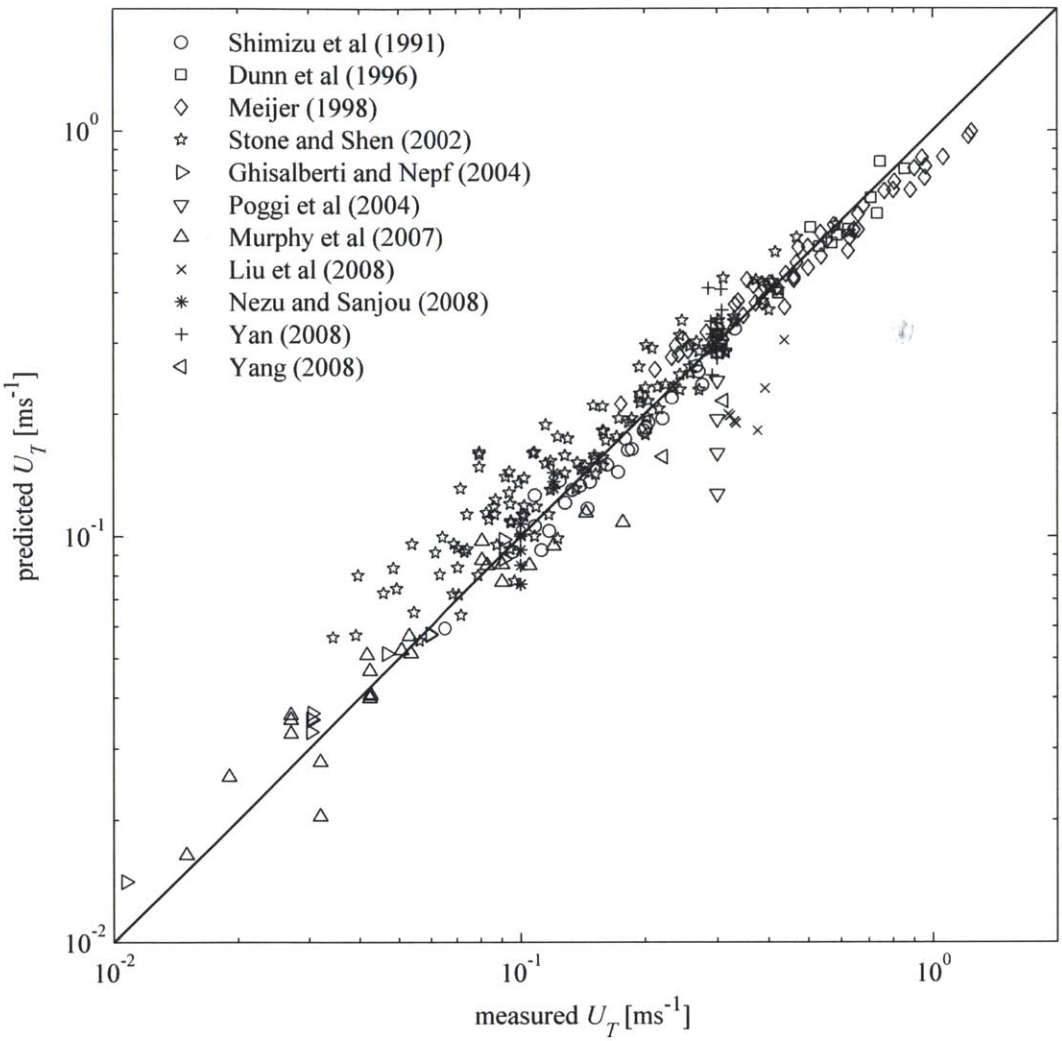

Figure 2-3: Velocity predicted by Eq. 2.7-2.9 compared with laboratory measurements. Laboratory data from [86, 20, 65, 91, 34, 76, 70, 53, 73, 102, 103] aggregated by Cheng [10]. Note that the predicted velocities are significantly higher than the some of the measurements from Stone and Shen (2002) [91]. This study employed densely packed cylinder arrays, for which the effective drag coefficient is likely to be higher than the assumed value of $C_D = 1$ (see e.g. [95]).

2.1.4 Finite patches

Strictly, the preceding two-dimensional analysis applies only for flows through vegetation patches that fill the channel width. For patches that do not fill the channel width, momentum exchange at the lateral boundaries of the patch can also be important. Laboratory observations, made by White and Nepf [100] for emergent patches adjacent to open water, suggest that a constant friction coefficient is appropriate at this interface as well. Specifically, White and Nepf [100] show that, over a range of flow speeds and vegetation configurations, $C_v = 2\tau_w/(\rho U_o{}^2) \approx 0.02$, where τ_w is the shear stress at the lateral interface between the patch and the open water, and U_o is velocity in the open water. This value for the friction coefficient is within the range ($C_v = 0.005 - 0.13$) reported by Cheng [10], suggesting that, as a first approximation, the shear stress at all the interfaces between vegetated patches and open water may be represented by a single friction coefficient. In §2.2, we use such an approach to calculate velocity in vegetated river reaches.

Note that the momentum balances developed here only consider fully developed flow. In many cases, vegetation exists in patches that have width and length scales much smaller than the channel width and reach length. Rominger and Nepf [79] show that at the leading edge of an emergent patch of finite width, flow development takes place over a length scale L_x that depends both on the scale of momentum dissipation due to drag, $(C_D a)^{-1}$, and the width of the patch, w. Specifically, they show that for dense or wide patches where $C_D a w > 4$, the flow inside the patch adjusts over a length scale set by the patch width, $L_x \sim w$. While for sparse or narrow patches with $C_D a w < 4$, the adjustment length is set by the momentum dissipation length scale, $L_x \sim (C_D a)^{-1}$. For the patches of rigid vegetation considered in Rominger and Nepf [79], the scale factors for these length scales were $L_x \approx 2.5w$ or $L_x \approx 5(C_D a)^{-1}$.

Finally, it is also important to distinguish between the development of flow inside and outside the patch of vegetation. Rominger and Nepf [79] consider the length scale over which the interior flow adjusts. For submerged canopies, Ghisalberti and Nepf [34] show that the exterior flow adjusts over a distance that is roughly ten times

the canopy height, $10h$. Data shown in Rominger and Nepf [79] suggest a similar scale to reach fully developed flow around emergent patches. That is, the exterior flow adjusts over a length scale of about $5w$, or 10 times the patch half-width. Assuming flow symmetry about the patch centerline, the half-width of an emergent patch (in the $x-y$ plane) is geometrically equivalent to the height of a submerged patch (in the $x-z$ plane).

2.2 Vegetation resistance at the reach-scale

In general, vegetation resistance is influenced by a number of factors including plant morphology, stiffness, and the distribution of vegetation within the channel. However, recent field studies by Green [38] and Nikora et al. [75] suggest that at the scale of river reaches, flow resistance due to vegetation is determined primarily by the blockage factor, B_X, which is the fraction of the channel cross-section blocked by vegetation. Both studies show strong correlations between B_X and simple measures of hydraulic resistance such as the Manning roughness coefficient, n_M, noting that the relationship between n_M and B_X is nonlinear. These observations are also in agreement with those made by Ree [78] and later by Wu et al. [101], who showed that roughness in channels lined with vegetation is influenced primarily by the submergence ratio, H/h.

A few studies (e.g., Bal et al. (2011) [3]) also suggest that the particular distribution pattern of the vegetation within the channel can play a role in dictating vegetation resistance. To study the effect of different distribution patterns on channel resistance, in §2.2.1 we extend the two-layer model described in §2.1.3 by including lateral momentum exchange between patches of vegetation and regions of unobstructed flow. Specifically, we consider whether, for the same total blockage factor B_X, the distribution of vegetation, in terms of the number of distinct patches, affects the hydraulic resistance. The discussion below is presented primarily in terms of dimensionless velocities (e.g., $U_T/(gSH)^{1/2}$). However, note that for natural channels, the volumetric flow is likely to be constant, set by the boundary conditions of the drainage basin. So, changes in hydraulic resistance lead to changes in both velocity and water depth.

2.2.1 Effect of vegetation distribution

To study the effect of vegetation distribution patterns on flow, and to evaluate whether this refinement to momentum balance models is warranted, we consider the following simplified scenario. We assume that at the scale of an entire reach, vegetated channels may be modeled using a single representative cross-section, despite the fact that patches of vegetation in natural channels can be of finite length and width, as well as heterogeneously distributed. This assumption is justified because any measure of hydraulic resistance at the reach scale must, by definition, be an integrated quantity. Specifically, we consider a rectangular channel with width W and depth H, and we assume that within this channel there are N identical patches of vegetation, each of height $h(< H)$ and width w/N, so that the total cross-sectional area of vegetation in the channel is wh, and the blockage factor is $B_X = wh/WH$, irrespective of N (see Fig. 2-4). The velocity in the unobstructed regions is U_o, while the velocity within each patch is U_v. Further, we assume that at all interfaces between the unobstructed flow and the vegetation patches, the shear stress is $\tau_v = (1/2)\rho C_v {U_o}^2$. The bed stress is given by $\tau_b = (1/2)\rho C_f {U_o}^2$ in the unobstructed regions. Within the patches, the bed stress is assumed to be negligible compared to vegetation drag. With these assumptions, the momentum balance in the unobstructed region is:

$$0 = \rho g S(WH - wh) - \tau_v L_v - \tau_b L_b \tag{2.10}$$

where L_v $(= 2Nh + w$ for $w < W, h < H)$ is the total interfacial area per unit channel length between the unobstructed flow and the patches, and L_b $(= 2H + W - w$ for $w < W)$ is the contact area per unit channel length between the unobstructed flow and the bed (see Fig. 2-4, inset). The momentum balance for each patch is:

$$0 = \rho g S(w/N)h + \tau_v L_v/N - (1/2)\rho C_D a h (w/N){U_v}^2 \tag{2.11}$$

For flexible vegetation, $C_D ah$ can vary with velocity. However, since accounting for these effects would require additional assumptions regarding the morphology and stiffness of the vegetation, for simplicity we assume that $C_D ah$ is a known value.

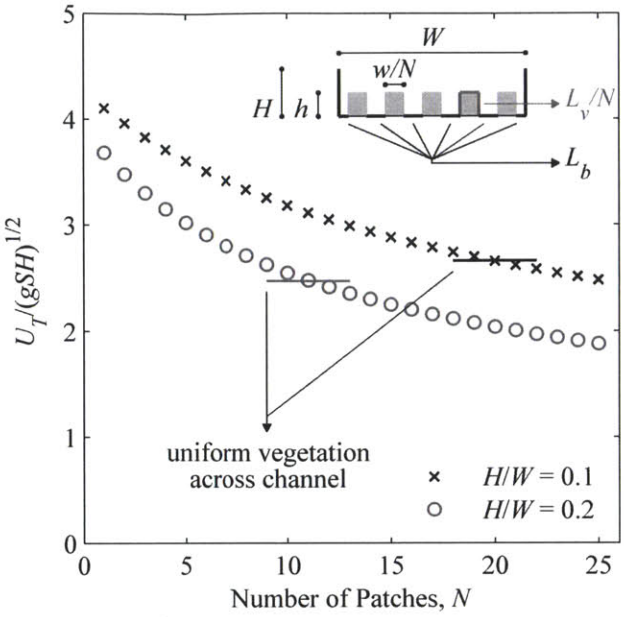

Figure 2-4: Dimensionless average velocity, $U_T/(gSH)^{1/2}$, plotted against number of individual patches, N, in channel. The inset shows the assumed channel geometry. L_v is the total length of the interface between the vegetation an open water (i.e., for all N patches). L_b is the total length of the interface between the unobstructed flow and the bed (i.e., summing all bold black lines).

Substituting the assumed expressions for the shear stresses into Eq. 2.10 and 2.11, and normalizing by the potential forcing, $(gSH)^{1/2}$, we have the following expressions for the dimensionless unobstructed flow and in-patch velocities:

$$U_o^* = \frac{U_o}{(gSH)^{1/2}} = \left(\frac{2W(1-B_X)}{C_f L_b + C_v L_v}\right)^{1/2} \tag{2.12}$$

$$U_v^* = \frac{U_v}{(gSH)^{1/2}} = \left(\frac{2WB_X + C_v L_v (U_o^*)^2}{C_D a W H B_X}\right)^{1/2} \tag{2.13}$$

A comparison of Eq. 2.12 and 2.13 with Eq. 2.7 and 2.8 shows that the momentum balance employed here is very similar in concept to that considered in 2.1.3, but incorporates more complex channel and patch geometry. Finally, the dimensionless average velocity in the channel is:

$$U_T^* = \frac{U_T}{(gSH)^{1/2}} = U_o^*(1-B_X) + U_v^* B_X \tag{2.14}$$

We solve the above system of equations for a typical channel of width $W = 5\text{m}$, and for two water depths, $H = 0.5\text{m}$ ($H/W = 0.1$) and $H = 1\text{m}$ ($H/W = 0.2$) (c.f. [38, 75]). We consider $N = 1 - 25$ patches distributed evenly across the channel, with the vegetation occupying half the channel width, $w = 0.5W$, and half the water depth, $h = 0.5H$. The blockage factor is therefore $B_X = 0.25$ (see Fig. 2-4). For simplicity, we assume that $C_D = 1$, and $C_f = C_v = 0.04$. The frontal area parameter, a, can vary greatly in natural systems. We use a value typical for dense channel vegetation, $a \approx 100\text{m}^{-1}$ [59].

Figure 2-4 shows that the dimensionless cross-sectional average velocity, $U_T/(gSH)^{1/2}$ (Eq. 2.14), decreases as the number of patches increases. This is because the interfacial area between the patches and the unobstructed flow increases when the patches are divided into smaller units (increasing N), leading to greater flow retardation due to the interfacial shear. This increase in the interfacial area is analogous to an increase in the wetted perimeter for the same cross-sectional area, i.e., it leads to a decrease in the hydraulic radius. Note that this simplified model breaks down for large values of N because, at this limit, the vegetation is essentially distributed uniformly across the channel with a lower spatial density, rather than in distinct patches. To account for this limitation, we also show in Fig. 2-4 (solid lines) the predicted velocities for the same amount of vegetation distributed uniformly across the channel, i.e., with $w = W$ (instead of $w = 0.5W$) and $a = 50\text{m}^{-1}$ (instead of 100m^{-1}). The predicted velocities for uniform vegetation and distinct patches coincide at $N = 20$ for the case where the channel aspect ratio is $H/W = 0.1$ (Fig. 2-4, black crosses and line) and at $N = 11$ for $H/W = 0.2$ (Fig. 2-4, gray circles and line). Beyond these points (at higher N), the model assumption of distinct patches breaks down. So, we interpret these velocities as the lower bounds for the systems considered.

Previous observations made in natural rivers and streams [40, 93] suggest that a more realistic upper bound for the number of distinct patches across a river channel is $N = 5$. Our simple model suggests that, for both channel aspect ratios, the velocity for $N = 5$ decreases by less than 20% relative to that for $N = 1$. For the more typical aspect ratio, $H/W = 0.1$, the velocity decreases by only 12%. Hence, we suggest that

$N = 1$ may be used to estimate velocities in the field for cases where blockage, B_X, is known but the exact distribution pattern of the vegetation is unknown, bearing in mind that this assumption introduces up to 20% uncertainty. Our results also provide some guidance as to what vegetation removal patterns would lead to the greatest decrease in hydraulic resistance. Flow resistance increases with increasing interfacial area between the vegetation and the unobstructed flow, and so vegetation removal strategies must try and minimize this interfacial area.

2.2.2 Predicting resistance coefficients in vegetated channels

Next, we use Eq. 2.12-2.14 to predict velocities for the field data collected by Green [38] and Nikora et al. [75]. Table 2.1 lists the variables reported by both studies, as well as the additional assumptions made to arrive at our predictions. The coefficients C_f and C_v were fitted to the data. Fig. 2-5 shows predicted average velocity plotted against the measurements, along with the best-fit values for C_f and C_v for each data set. The predicted velocities show good correlation with the measurements: $r^2 = 0.87$ for Green [38], and $r^2 = 0.57$ for Nikora et al. [75]. Further, the fitted coefficients for the Nikora et al. data, $C_f = 0.041$ and $C_v = 0.05$ lie within the expected range ($C_f \approx 0.015-0.19$ [38]; $C_v \approx 0.005-0.13$ [10]). However, the fitted value of $C_v = 0.21$ for the Green data is higher than the range suggested by the laboratory experiments. The interface between the vegetation and the unobstructed flow may be rougher for the high vegetation densities and complex plant morphologies typical of field conditions, leading to a higher C_v. The higher fitted value for C_v could also be due to the single-patch assumption, $N = 1$ (Table 2.1). Since the interfacial area between the vegetation and unobstructed flow increases as the number of distinct patches increases, a lower C_v would generate the same retarding shear force for larger N.

Unfortunately, it is often difficult to make field measurements that allow independent estimates for the bed friction coefficient, C_f (e.g., through measured grain size distributions), and for the drag parameter, $C_D a$ (e.g., through stem density and plant morphology studies). Further, the relationship between C_v and vegetation properties is not well defined (see e.g. [10]). As a result, the use of Eq. 2.12-2.14 to predict

Table 2.1: Field data reported by Green [38] and Nikora et al. [75], and the additional assumptions made to arrive at velocity predictions

Green [38]	
Reported	
U_T	Reported as V
S	
B_X	Reported as B^X
Assumptions	
$H = R_H$	Hydraulic radius, R_H reported
$W = 10R_H$	Assuming a typical aspect ratio, $H/W = 10$
$w = B^{SA}W$	Surface area blockage, B^{SA} reported
$C_D a = 100\text{m}^{-1}$	Typical for channel vegetation
$N = 1$	

Nikora et al. [75]	
Reported	
U_T	Reported as U
S	
H	
W	
h	Reported as h_c
w	Reported as W_c
Assumptions	
$C_D a = 100\text{m}^{-1}$	Typical for channel vegetation
$N = 1$	

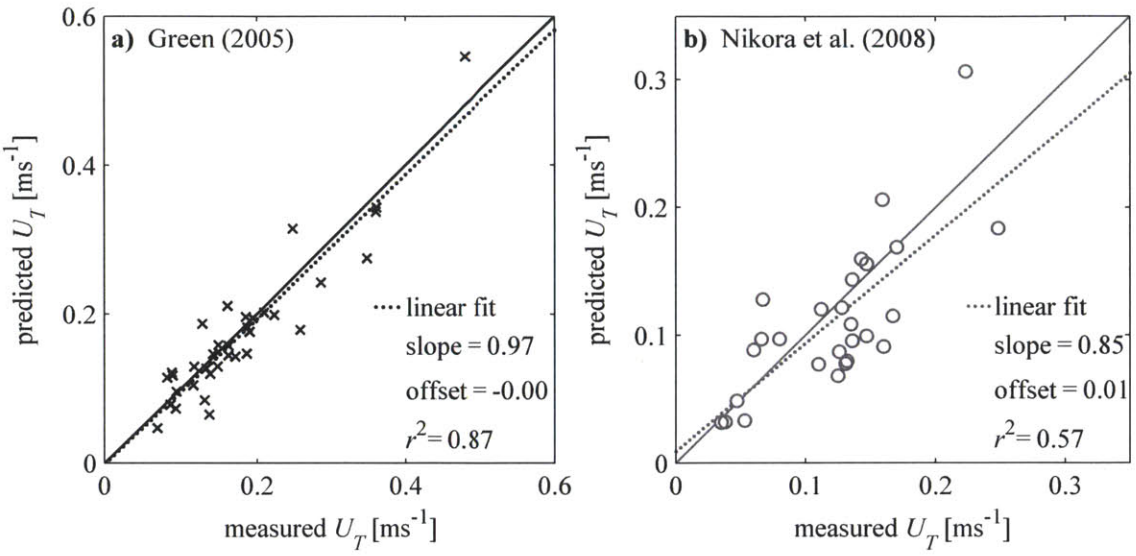

Figure 2-5: Velocities predicted by Eq. 2.12-2.14 plotted against measurements from (a) Green (2005) [38] and (b) Nikora et al. (2008) [75]. Best-fit values for the friction coefficients were $C_f = 0.052, C_v = 0.21$ for the Green (2005) data set, and $C_f = 0.041, C_v = 0.050$ for the Nikora et al. (2008) data set.

velocities in the field may not be practical. As an alternative, we further simplify the momentum balance for field application, where simple measures of hydraulic resistance such as the Manning roughness, n_M, are required. First, we assume that the friction coefficients at the bed and at the interface between the vegetation and open water are identical, $C_f = C_v = C$. This is reasonable given the natural variability expected for these parameters, and also because the field and laboratory observations considered in this paper suggest similar ranges for C_f $(= 0.015 - 0.19)$ and C_v $(= 0.005 - 0.13)$. Next, we assume that the channel is sufficiently shallow so that the sum of the interfacial areas per unit channel length approximately equals to the channel width, $L_v + L_b \approx W$. This is analogous to assuming that the channel hydraulic radius, R_H, is approximately equal to the channel depth, H. With these simplifications, the dimensionless velocities in the unobstructed region (Eq. 2.12) and within the patch (Eq. 2.13) become:

$$U_o^* = \frac{U_o}{(gSH)^{1/2}} = \left(\frac{2(1 - B_X)}{C}\right)^{1/2} \tag{2.15}$$

$$U_v^* = \frac{U_v}{(gSH)^{1/2}} = \left(\frac{2B_X + 2(L_v/W)(1-B_X)}{C_D a H B_X}\right)^{1/2} \tag{2.16}$$

The friction coefficient $C \sim O(0.1)$ is likely to be two orders of magnitude smaller than the drag parameter $C_D aH \sim O(10)$ (assuming $C_D = 1$, $a \approx 100\text{m}^{-1}$ and $H \sim O(0.1)\text{m}$). Hence, the velocity inside the patch of vegetation is likely to be an order of magnitude lower than that in the unobstructed flow, i.e., $U_v^* \ll U_o^*$. Therefore, as a first approximation, we assume that the in-patch velocity may be neglected, and so the expression for the average velocity in the channel cross-section (Eq. 2.14) becomes:

$$U_T^* \approx U_o^*(1-B_X) = \left(\frac{2}{C}\right)^{1/2}(1-B_X)^{3/2} \tag{2.17}$$

The Manning roughness is defined as $n_M = (KR_H^{2/3}S^{1/2})/U_T$, where the constant $K = 1\ \text{m}^{1/3}\text{s}^{-1}$ is required to make the equation dimensionally correct, and the hydraulic radius is approximately equal to channel depth, $R_H \approx H$, for shallow channels. Therefore, Eq. 2.17 suggests the following relationship between the Manning roughness and blockage factor:

$$n_M\left(\frac{g^{1/2}}{KH^{1/6}}\right) = \left(\frac{C}{2}\right)^{1/2}(1-B_X)^{-3/2} \tag{2.18}$$

Somewhat surprisingly, Eq. 2.18 suggests that n_M does not depend on the morphology of the vegetation itself (e.g. on the frontal area per unit volume, a). Instead, channel resistance is set primarily by the blockage factor. Conceptually, this is because the primary effect of dense patches of vegetation with regard to flow resistance is to redistribute the flow into a smaller region, thereby increasing the hydraulic radius and resistance.

Importantly, note that when a large fraction of the channel is blocked by vegetation, the assumption that the in-patch velocity does not contribute significantly to the total flow breaks down; so, Eq. 2.17 and 2.18 are no longer valid. In fact, for a channel cross-section that is completely vegetated, $B_X = 1$, we expect from Eq. 2.16 that the average velocity is:

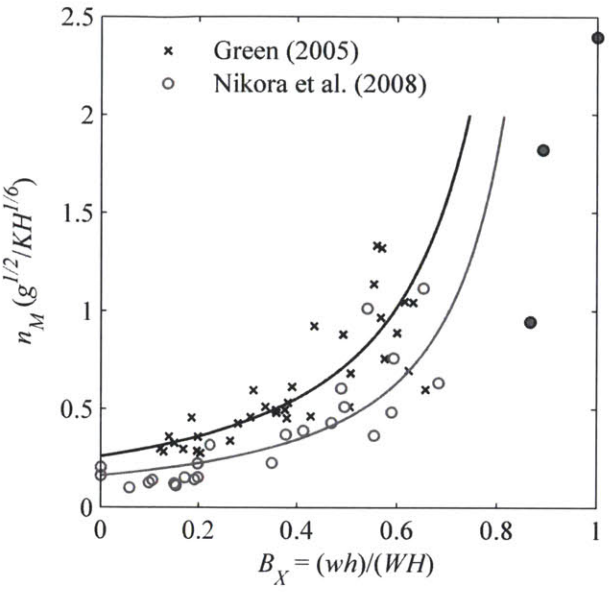

Figure 2-6: Normalized Manning roughness, $n_M(g^{1/2}/KH^{1/6})$, plotted against the blockage factor, B_X for the field data collected by Green [38] and Nikora et al. [75]. Solid lines show predictions based on Eq. 2.18 using fitted values for the friction coefficients, $C = 0.13$ (black line) and $C = 0.052$ (gray line). Filled gray circles denote cases with $B_X > 0.8$.

$$U_T^* = U_v^* = \left(\frac{2}{C_D a H}\right)^{1/2} \tag{2.19}$$

which is identical to the expression for emergent vegetation shown in Eq. 2.3. For a completely vegetation channel therefore, the Manning roughness is:

$$n_M \left(\frac{g^{1/2}}{KH^{1/6}}\right) = \left(\frac{C_D a H}{2}\right)^{1/2} \tag{2.20}$$

Figure 2-6 shows $n_M(g^{1/2}/KH^{1/6})$ plotted against the blockage factor, B_X, for the Green ([38], black crosses) and Nikora et al. ([75], gray circles) data sets. Also shown are the predictions made using Eq. 2.18, with a fitted value of the friction coefficient, C, for each dataset. The best fit suggests that $C = 0.13 \pm 0.03$ for the Green data (solid black line) and $C = 0.05 \pm 0.02$ for the Nikora et al. data (solid gray line). Both values for C are physically consistent since they fall between the observed ranges for C_f and C_v. The roughness predicted from Eq. 2.18 captures the observed nonlinear relationship between n_M and B_X. Further, the velocities predicted

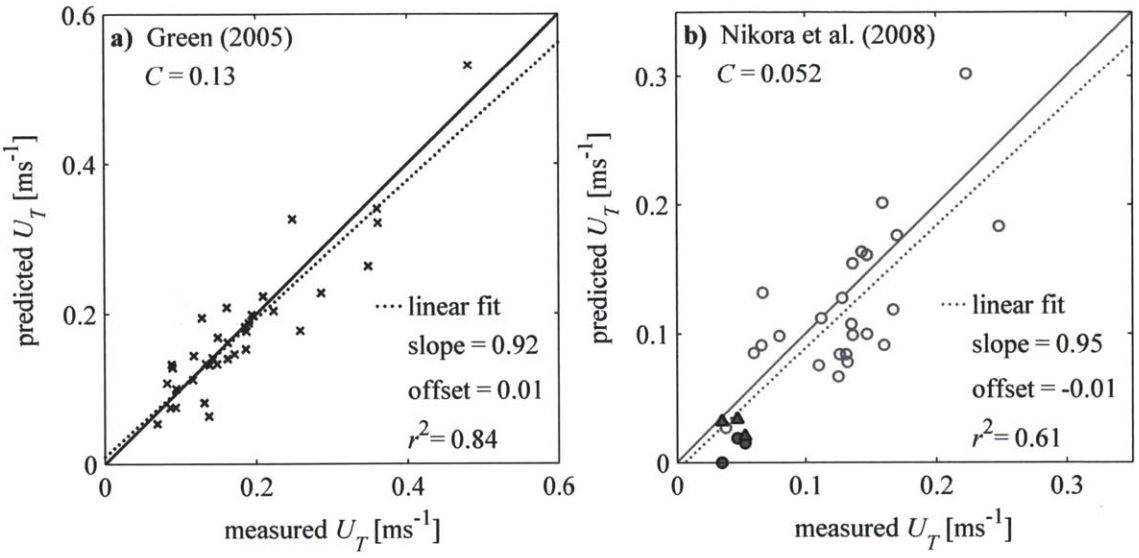

Figure 2-7: Velocities predicted by Eq. 2.17 plotted against measurements from Green [38] and Nikora et al. [75]. Fitted values for the friction coefficient, C, are shown on the plots. The filled gray circles in (b) show velocities predicted by Eq. 2.17 for the three cases with $B_X > 0.8$ (see Fig. 2-6). The filled gray triangles show predictions made using Eq. 2.19, which is more appropriate for $B_X > 0.8$.

using the simplified Eq. 2.17 are just as well correlated with the measurements as the velocities predicted using Eq. 2.12-2.14. Specifically, $r^2 = 0.84$ for Green [38], and $r^2 = 0.61$ for Nikora et al. [75] (compare Fig. 2-5 and Fig. 2-7).

As discussed above, when a large fraction of the channel cross section is blocked by vegetation, the assumptions that led to Eq. 2.17 and 2.18 are no longer valid; Eq. 2.19 and 2.20 are likely to apply instead. As a result, we excluded the three observations where more than 80% of the channel cross-section was blocked by vegetation ($B_X > 0.8$, filled gray circles in Fig. 2-6 and 2-7) in order to estimate C for the Nikora et al. [75] data set. For $C_D aH \approx 10$, we expect that from Eq. 2.20 that $n_M(g^{1/2}/KH^{1/6}) \approx 2.2$ when the channel is completely vegetated, $B_X = 1$. The observations shown in Fig. 2-6 are consistent with this prediction. Specifically, for $B_X = 1$, the normalized Manning roughness is $n_M(g^{1/2}/KH^{1/6}) = 2.4$. Similarly, Fig. 2-7 shows that velocities predicted using the blocked channel assumption, Eq. 2.19 (gray triangles), for the three cases with $B_X > 0.8$ are closer to the measured velocities compared to the predictions made using Eq. 2.17 (gray circles).

Chapter 3

Wave-induced flows inside seagrass canopies

This chapter describes laboratory and field studies investigating the flow structure within seagrass beds subject to propagating waves. The laboratory study (§3.2) employed flexible model vegetation, scaled to be dynamically similar to real seagrasses [33]. The field study (§3.3) was carried out in Cala Millor, located on the eastern coast of Mallorca, one of the Balearic Islands in the Mediterranean Sea. Our measurements reveal that a mean current is generated within seagrass canopies forced by purely oscillatory, wave-driven flow. Further, the hydrodynamic drag exerted by the vegetation leads to a reduction of the in-canopy oscillatory velocity. However, the ratio of in-canopy to above-canopy velocity is significantly higher for oscillatory flows (tested here) compared to the unidirectional case tested by Ghisalberti and Nepf [35]. Most of this chapter is derived from the article Luhar et al. (2010) [56]. The field study (§3.3) is as yet unpublished.

3.1 Theory

For waves propagating over a flat bed in the absence of a canopy, linear wave theory (e.g. [64]) leads to the following solutions for the horizontal (u_w) and vertical (w_w) oscillatory velocity fields:

$$u_w = a_w \omega \frac{\cosh(kz)}{\sinh(kH)} \cos(kx - \omega t) \tag{3.1}$$

$$w_w = a_w \omega \frac{\sinh(kz)}{\sinh(kH)} \sin(kx - \omega t) \tag{3.2}$$

and wave-induced dynamic pressure

$$p_w = \rho \frac{\omega}{k} u_w = \rho g a_w \frac{\cosh(kz)}{\cosh(kH)} \cos(kx - \omega t) \tag{3.3}$$

In the equations above, ρ is the water density, g is the acceleration due to gravity, a_w is the wave amplitude, ω is the wave radian frequency, k is the wavenumber, H is the mean water depth, x and z are the horizontal and vertical coordinates ($z = 0$ at the bed), and t is time. Wave frequency, wave number, and water depth are related by the dispersion relation: $\omega^2 = kg \tanh(kH)$. Throughout this chapter, the subscript w refers to purely oscillatory flows (i.e., time average of zero). When we refer specifically to unidirectional flows (currents) the subscript c is used. Further, for oscillatory velocities we use upper case symbols to denote amplitude, e.g., $u_w = U_w \cos(kx - \omega t)$. Turbulent, fluctuating velocities are represented by lower case letters with prime symbols (u', w').

In addition to neglecting the nonlinear terms in the Navier-Stokes equations, linear wave theory assumes perfectly inviscid, irrotational motion. Under these assumptions, the horizontal and vertical velocities are exactly 90° out of phase with each other, as evidenced by Eq. 3.1 and 3.2. However, this solution does not satisfy the no-slip boundary condition at the bed. While the inviscid assumption is valid for most of the water column, viscosity is important in the bottom boundary layer, which is of thickness $O(\sqrt{\nu/\omega})$ for laminar flow. Here, ν is the kinematic viscosity of water. The horizontal oscillatory velocity decays from the inviscid value, given by Eq. 3.1, at the outer edge of the boundary layer to zero at the bed because of viscosity. This modification to the inviscid solution causes a phase shift in the oscillatory velocities. The horizontal and vertical velocities are no longer exactly 90° out of phase, creating a steady, non-zero wave stress, $\overline{u_w w_w} \neq 0$ (the over-bar denotes a time average).

This wave stress is analogous to turbulent Reynolds stress. It represents a steady momentum transfer out of the oscillatory flow, and generates a mean current in the boundary layer. For laminar flows, the magnitude of this current, U_c, at the outer edge of the boundary layer is [54]

$$U_c = \frac{3}{4}(ka_w)\frac{a_w\omega}{\sinh^2(kH)} \tag{3.4}$$

The forces exerted by seagrass canopies also lead to a phase shift between the oscillatory velocities, resulting in a non-zero wave stress. Below, we present an overview of the forces exerted by seagrass canopies on wave flow (based on Lowe et al. [55]) followed by a new analysis estimating the wave-induced mean current generated within seagrass canopies.

3.1.1 Canopy momentum balance

Lowe et al. [55] described the water motion within a rigid canopy (a model coral reef) relative to the undisturbed flow above the canopy. Here, we consider the application of their model to a flexible canopy (a seagrass meadow). For seagrass blades of width b, and thickness d, the geometry of the canopy is described by two dimensionless parameters: the frontal area per unit bed area, ah, and the solid volume fraction, $\phi = ad$ (c.f. §2.1). Here, $a = nb$ is the frontal area per unit volume and h is the height of the canopy; n is the number of individual blades per unit bed area. Because of the forces exerted by the vegetation, the velocity scale within the meadow, $\hat{U}_{w,m}$, is reduced relative to that above the meadow, $U_{w,\infty}$. Note that the velocity scale inside the meadow, $\hat{U}_{w,m}$, represents a vertical average over the canopy height.

The velocity ratio, $\alpha = \hat{U}_{w,m}/U_{w,\infty}$, depends on the relative importance of the shear stress at the top of the meadow, $(1/2)\rho C_v|u_{w,\infty}|u_{w,\infty}$, the drag exerted by the meadow, $(1/2)\rho C_D ah|\hat{u}_{w,m}|\hat{u}_{w,m}/(1-\phi)$, and the inertial forces including added mass, $\rho C_M(\phi/(1-\phi))(\partial\hat{u}_{w,m}/\partial t)$. C_M is the added mass coefficient. As before, C_v is friction coefficient at the top of the canopy, and C_D is the vegetation drag coefficient. These three forces are characterized by the following length scales: the shear length scale:

$$L_S = \frac{2h}{C_v} \tag{3.5}$$

the drag length scale:

$$L_D = \frac{2h(1-\phi)}{C_D a h} \tag{3.6}$$

and the oscillation length scale, which is simply the wave orbital excursion above the meadow, $A_{w,\infty} = U_{w,\infty}/\omega$. Conceptually, the drag and shear length scales describe the scale at which the effects of drag and shear begin to influence fluid motion. Note that the drag length scale L_D is proportional to the length scale $\delta \approx 0.1(C_D a)^{-1}$ introduced in §2.1, which describes the distance over which the momentum transferred into the canopy from the overflow is dissipated by vegetation drag. So, in some ways, the ratio L_S/L_D, which represents the relative magnitude of the shear stress and drag, is analogous to δ/h, which is the fraction of the canopy over which momentum transfer due to turbulent shear is important.

Following Lowe et al. [55], the canopy-averaged momentum balance based on the force formulation shown above is:

$$\frac{\partial(\hat{u}_{w,m} - u_{w,\infty})}{\partial t} = \frac{|u_{w,\infty}|u_{w,\infty}}{L_S} - \frac{|\hat{u}_{w,m}|\hat{u}_{w,m}}{L_D} - C_M \frac{\phi}{1-\phi}\frac{\partial \hat{u}_{w,m}}{\partial t} \tag{3.7}$$

Eq. 3.7 assumes that the horizontal velocity varies minimally over the height of the canopy, such that $u_w(z = h) \approx u_w(z = 0)$. From Eq. 3.1, we see that for this to be true, $kh \ll 1$ such that $\cosh(kh) \approx 1$. By considering only the first Fourier harmonic, and introducing the complex notation $\hat{u}_{w,m} = \Re\{\beta U_{w,\infty} \exp(i\omega t)\}$ and $u_{w,\infty} = \Re\{U_{w,\infty} \exp(i\omega t)\}$, Eq. 3.7 can be written as:

$$i(\beta - 1) = \frac{8}{3\pi}\frac{A_{w,\infty}}{L_S} - \frac{8}{3\pi}\frac{A_{w,\infty}}{L_D}|\beta|\beta - iC_M\frac{\phi}{1-\phi}\beta \tag{3.8}$$

To obtain Eq. 3.8, we assume that $U_{w,\infty}$ and $A_{w,\infty}$ are real and positive, while β may be complex. The ratio of in-canopy velocity to the velocity above the canopy is $\alpha = \hat{U}_{w,m}/U_{w,\infty} = |\beta|$.

From Eq. 3.8, we see that if the wave excursion is smaller than the drag and shear length scales, $A_{w,\infty} \ll (L_S, L_D)$, the wave motion is unaffected by the drag and shear stress, and the flow is dominated by inertia. At this limit, the velocity ratio is:

$$\alpha_i = |\beta| = \frac{1-\phi}{1+(C_M-1)\phi} \tag{3.9}$$

with subscript i used to emphasize inertia-dominated conditions. At the other limit of flow behavior, when the wave excursion is much longer than L_S and L_D, the flow resembles a steady current. At this limit, the inertial forces are negligible, and flow within the meadow is determined by a balance between shear and drag. Using a subscript c to denote this current-type limit, we have the following velocity ratio:

$$\alpha_c = \sqrt{\frac{L_D}{L_S}} \tag{3.10}$$

For the intermediate case, where the effects of both drag and inertia are important, Eq. 3.8 must be solved iteratively to yield $\alpha = |\beta|$. Lowe et al. [55] solved Eq. 3.7 numerically by providing an initial condition and marching forward in time until a quasi-steady state was achieved. Alternatively, we propose the use of the Fourier decomposition shown in Eq. 3.8, which yields identical results for the inertia and current limits, but can be solved more easily for the general case.

Finally, note that Eq. 3.7 assumes that the canopy elements are rigid, which is not the case with flexible seagrasses. However, incorporating the impact of wave-induced blade movement in a predictive model is difficult and requires a coupled flow-structure interaction model. We develop a simple dynamic blade model in §5, which suggests that a rigid canopy model may be used to capture the forces exerted by flexible seagrasses as long as an effective canopy height is used. This effective height is defined as the vertical extent of the canopy over which the flexible blades do not move significantly relative to the water. For simplicity, throughout this chapter, we assume that the effective canopy height is equal to the blade length, $h = l$.

3.1.2 Wave-induced current

We propose that the forces generated within a seagrass meadow lead to a nonzero wave stress at the top of the canopy, which drives a mean current through the meadow. To estimate the magnitude of this wave stress, we consider the time-averaged energy balance for the meadow. Wave energy is transferred from the outer flow into the meadow via the work done by the wave induced pressure at the top of the meadow, $-\overline{p_{w,\infty} w_{w,\infty}}$, and the work done by the shear stress at the interface, $\overline{\tau_{w,\infty} u_{w,\infty}}$. The energy transfer is balanced by dissipation within the meadow, $\overline{E_D}$:

$$-\overline{p_{w,\infty} w_{w,\infty}} + \overline{\tau_{w,\infty} u_{w,\infty}} = \overline{E_D} \tag{3.11}$$

Note that E_D includes dissipation due to the forces exerted by the vegetation, dissipation due to bed stress, and shear-induced viscous dissipation.

Above the meadow, we assume the horizontal oscillatory velocity, $u_{w,\infty}$, and dynamic pressure, $p_{w,\infty}$, are specified by the linear wave solution; hence, $p_{w,\infty} = \rho(\omega/k) u_{w,\infty}$ as shown in Eq. 3.3. Then, Eq. 3.11 may be rearranged to yield the time-averaged wave stress at the top of the canopy:

$$\rho\overline{u_{w,\infty} w_{w,\infty}} = \frac{k}{\omega}\left(\overline{\tau_{w,\infty} u_{w,\infty}} - \overline{E_D}\right) \tag{3.12}$$

Next, we assume that energy dissipation is dominated by the drag force, f_D, exerted by the vegetation i.e., excluding bed friction and viscous dissipation (see e.g., Mendez and Losada [67], Bradley and Houser [8]),

$$\overline{E_D} = \overline{\int_0^h f_D u_m \, dz} \tag{3.13}$$

where $u_m = u_{w,m} + U_{c,m}$ is the velocity within the meadow, anticipating the presence of a mean current, $U_{c,m}$. We ignore the contribution of the inertia force since this tends to be in phase with the flow acceleration, leading to a zero time-average when multiplied by the velocity. Further, for typical values of C_v and $C_D a h$ the energetic contribution of the work done by the shear stress, which is of $O(\rho C_v U_{w,\infty}^3)$, is negligible

compared to the total energy dissipation, which is of $O(C_D a h \hat{U}_{w,m}^3)$. Specifically, the magnitude of the in-canopy velocity, $\hat{U}_{w,m}$, is comparable to the outer flow velocity, $U_{w,\infty}$, (see Table 3.1) but $C_v \sim O(0.01 - 0.1)$ while $C_D a h \sim O(1 - 10)$. With these assumptions, the time-averaged wave stress at the top of the canopy simplifies to:

$$\rho\overline{u_{w,\infty} w_{w,\infty}} = -\frac{k}{\omega}\overline{\int_0^h f_D u_m \, dz} \tag{3.14}$$

Integrating the time-averaged momentum equation over the canopy height leads to the following, physically intuitive balance (see e.g., Fredsoe and Deigaard [31])

$$-\rho\overline{u_{w,\infty} w_{w,\infty}} + \overline{\tau}(z = h) - \overline{\tau}(z = 0) = \overline{\int_0^h f_D \, dz} \tag{3.15}$$

where $\overline{\tau}$ is the mean shear stress. For simplicity, the $\partial/\partial x$ convective acceleration term, caused by slow wave decay in the x-direction and the mean pressure gradient have been assumed negligible. Assuming that the shear stresses are negligible compared to the vegetation drag, Eq. 3.14 and 3.15 can be combined to yield:

$$\frac{k}{\omega}\overline{\int_0^h f_D u_m \, dz} = \overline{\int_0^h f_D \, dz} \tag{3.16}$$

The drag force, using a standard quadratic formulation, is $f_D = (1/2)\rho C_D a|(u_{w,m} + U_{c,m})|(u_{w,m} + U_{c,m})$. However, experimental results [81] and numerical simulations [104] suggest that a two-term formulation is more appropriate in combined wave-current flows. Following Zhou and Graham [104], we decompose the drag force into its steady and time-varying components with separate drag coefficients:

$$f_D = f_{Dc} + f_{Dw}(t) = \frac{1}{2}\rho a \left(C_{Dc} U_{c,m}^2 + C_{Dw}|u_{w,m}(t)|u_{w,m}(t) \right) \tag{3.17}$$

Both C_{Dc} and C_{Dw} depend on the Reynolds number, $Re = U_{w,m} b/\nu$, the Keulegan-Carpenter number, $KC = U_{w,m} T_w / b$ (T_w is the wave period), and the ratio of mean to oscillatory velocity, $U_{c,m}/U_{w,m}$. However, the two drag coefficients are typically comparable in magnitude.

Substituting Eq. 3.17 into Eq. 3.16, and time averaging under the assumption that the parameters C_{Dw}, C_{Dc}, and a are constants leads to:

$$\overline{\frac{k}{\omega}\int_0^h C_{Dc}U_{c,m}^3 + \frac{4}{3\pi}C_{Dw}U_{w,m}^3\,dz} = \overline{\int_0^h C_{Dc}U_{c,m}^2\,dz} \tag{3.18}$$

The mean current is a second-order phenomenon, generated because of nonlinear interaction between the oscillatory velocities, and so we anticipate $U_{c,m}^3 \ll U_{w,m}^3$. For simplicity, we also assume that the mean and oscillatory velocity do not vary over the height of the canopy, i.e., $U_{c,m} = \hat{U}_{c,m}$ and $U_{w,m} = \hat{U}_{w,m}$ (the over-hat denotes a canopy-average). With these further assumptions, Eq. 3.18 can be solved to yield a simple estimate for the mean current generated within the meadow:

$$\hat{U}_{c,m} = \sqrt{\frac{4}{3\pi}\frac{C_{Dw}}{C_{Dc}}\frac{k}{\omega}\hat{U}_{w,m}^3} \tag{3.19}$$

Equation 3.19 indicates that the magnitude of the mean current is controlled primarily by wave parameters (k, ω, and $\hat{U}_{w,m}$) and does not depend on the canopy parameters (a and h). However, below we discuss how the conditions under which Eq. 3.19 applies is dependent on the ratio of blade spacing and wave excursion, i.e., it will have some dependence on a. In addition to the wave conditions, an important quantity governing the magnitude of the mean current is the ratio of drag coefficients, C_{Dw}/C_{Dc}. Zhou and Graham [104] carried out numerical simulations estimating the force acting on a single, circular cylinder in combined wave-current flows. Simulation results for $U_c/U_w = 0.25$ showed the drag coefficient ratio to decrease from $C_{Dw}/C_{Dc} \approx 1.8$ for $KC = 0.2$ ($Re = 40$) to $C_{Dw}/C_{Dc} \approx 0.5$ for $KC = 26$ ($Re = 5200$), with Re and KC based on cylinder diameter. For the laboratory experiments described in this chapter, the Keulegan-Carpenter number based on blade width and near-bed orbital velocity, ranges from $KC \approx 14$ ($Re \approx 90$) to $KC \approx 94$ ($Re \approx 590$). If the stem diameter is used instead of blade width, which might be more appropriate near the base of the model plants used for the experiments (see §3.2), the ranges are $KC \approx 5.8 - 39$ ($Re \approx 220 - 1400$). Given the overlap in range between the experiments conditions considered here, and the numerical simulations carried out by

Zhou and Graham [104], it is reasonable to assume that $C_{Dw}/C_{Dc} \sim O(1)$.

3.2 Laboratory study

3.2.1 Experimental methods

The experiments were performed in a 24 m-long, 38 cm-wide and 60 cm-deep flume equipped with a paddle-type wave maker. The vertical paddle was actuated using a hydraulic piston driven by a Syscomp WGM-101 arbitrary waveform generator. The waveform generator was programmed to produce surface waves of the desired amplitude and frequency based on the closed-form solution for paddle motion described in Madsen [60] (see Appendix A). A plywood beach of slope 1:5, covered with rubberized coconut fiber, limited reflections to less than 10% of the incident wave. The model canopy was 5 m long (see Fig. 3-1). The canopy comprised of model plants placed in four pre-drilled baseboards 1.25 m long. Two additional baseboards were placed both upstream and downstream of the model vegetation to ensure a uniform bed roughness across the test section. Each model plant consisted of six polyethylene (density $\rho_v = 920$ kg m^{-3}; elastic modulus $E = 3 \times 10^8$ Pa) blades of length $l = 13$ cm, width $b = 3$ mm, and thickness $d = 0.1$ mm attached to a 2 cm long wooden dowel of diameter 0.64 cm using rubber bands. With the rubber bands in place, the maximum diameter of the dowels was distributed with a mean 0.92 cm and standard deviation 0.03 cm. Where necessary, a mean stem diameter, $d_c = 0.78$ cm, is used. When inserted into the baseboards the stems (dowels) protruded 1 cm above the bed.

Velocity measurements were made with a 3-dimensional Acoustic Doppler Velocimeter (ADV, Nortek Vectrino). Synchronous measurements of the wave height were made at the same x-location using a wave gage of 0.2 mm accuracy. The analog output from the wave gage was amplified and logged to a computer using an analog-digital converter (National Instruments NI-USB6210). Both the ADV and wave gage were mounted on a trolley moving on precision rails. Vertical profiles of velocity were measured at two longitudinal locations: midway through the canopy and upstream of

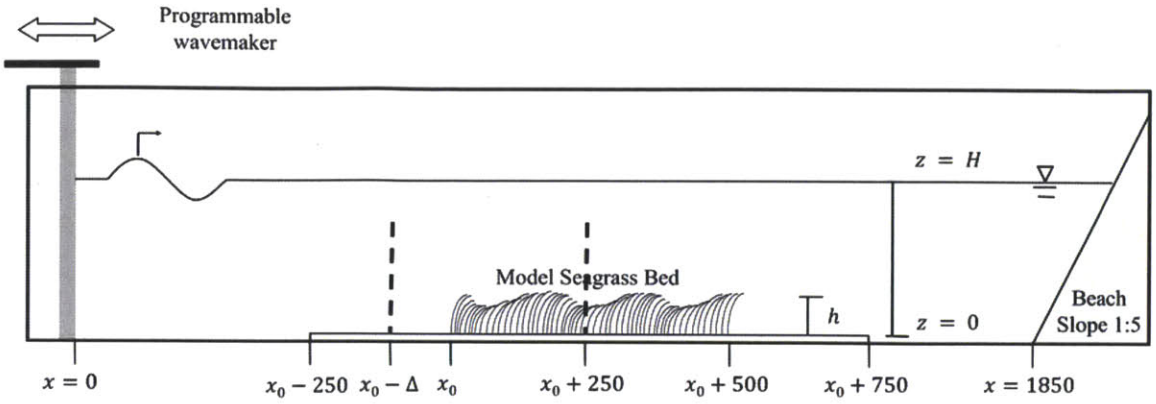

Figure 3-1: Schematic showing experimental setup. The bold dashed line indicates measurement locations for the vertical profile of velocity. Not to scale.

the canopy. The model bed was shifted longitudinally along the flume to ensure that the measurement location midway through the canopy corresponded to an anti-node of the partially standing waves created by reflections from the downstream end of the flume. The other measurement location was chosen to be an anti-node at least half a wavelength upstream of the canopy. This eliminated the lower order, spatially periodic variation in wave and velocity amplitude associated with the 10% reflection. Velocities were measured at 1-cm vertical intervals. At each location, velocities and surface displacement were measured for 6 minutes at 25 Hz. The height of the lowest measurement location varied between 0.1 and 0.9 cm above the bed ($z = 0$).

A schematic of the setup is shown in Fig. 3-1. Wave period ($T_w = 0.9 - 2.0$ s) and amplitude ($a_w = 0.8 - 5.3$ cm), water depth ($H = 16 - 39$ cm) and vegetation density ($n_s = 300 - 1800$ stems m^{-2}, or $n = 1800 - 10800$ blades m^{-2}) were varied systematically. These parameter ranges were chosen based on typical field values for the dimensionless parameters a_w/H, kH, h/H and ah. The conditions for each experimental run are shown in Table 3.1. In order to measure velocities close to the bed within the meadow, all vegetation was removed from a circular area approximately 10 cm in diameter, which was the minimum cleared area necessary to prevent blades from entering the ADV measurement control volume. To test if the clearing had an appreciable impact on the velocity structure near the bed, three runs were repeated with the wooden dowels (with rubber bands, but no blades attached) left in place in

Table 3.1: Wave and vegetation parameters for the laboratory experiments. The last row indicates typical uncertainty.

Run	n_s [cm^{-2}]	H [cm]	T_w [s]	a_w [cm]	$A_{w,\infty}/S$	α ‡ ($z = 1$ cm)	α (3.8) **	α_i (3.9) **	$\hat{U}_{c,m}$ ‡ [cm s^{-1}]	$z(U_c = 0)$ ‡ [cm]	$\hat{U}_{c,m}$ (3.19) ** [cm s^{-1}]
D1	0.03	39	1.4	3.2	0.5	0.95	0.97	0.97	0.5	11.2	2.1
D2	0.06	39	1.4	3.1	0.7	0.92	0.94	0.94	0.9	12.7	1.9
D3	0.09	39	1.4	3.1	0.8	0.92	0.91	0.92	1.0	13.1	1.9
D4*	0.12	39	1.4	3.1	1.0	0.94	0.87	0.89	1.8	10.9	1.9
D5	0.15	39	1.4	3.0	1.1	0.94	0.84	0.87	1.9	13.3	1.9
D6	0.18	39	1.4	2.9	1.1	0.92	0.82	0.84	1.6	14.1	1.8
D6†	0.18	39	1.4	3.1	1.2	0.79	0.81	0.84	1.9	11.1	2.0
H1	0.12	16	1.4	0.9	0.6	0.95	0.89	0.89	0.3	5.2	1.0
H2	0.12	24	1.4	1.7	0.8	0.94	0.88	0.89	0.8	9.0	1.5
H3	0.12	32	1.4	2.4	0.9	0.93	0.88	0.89	1.4	9.2	1.7
H4*	0.12	39	1.4	3.1	1.0	0.94	0.87	0.89	1.8	10.9	1.9
T1	0.12	39	0.9	2.8	0.4	0.93	0.89	0.89	0.4	1.9	0.7
T2	0.12	39	1.1	3.3	0.7	0.92	0.88	0.89	1.1	9.1	1.6
T3*	0.12	39	1.4	3.1	1.0	0.94	0.87	0.89	1.8	10.9	1.9
T4	0.12	39	2.0	3.2	1.6	0.89	0.85	0.89	2.2	13.4	2.5
A1	0.12	39	1.4	0.8	0.2	0.94	0.89	0.89	0.1	1.7	0.3
A1†	0.12	39	1.4	0.8	0.3	0.92	0.89	0.89	0.1	4.9	0.3
A2	0.12	39	1.4	1.7	0.5	0.95	0.89	0.89	0.4	10.2	0.8
A3*	0.12	39	1.4	3.1	1.0	0.94	0.87	0.89	1.8	10.9	1.9
A4	0.12	39	1.4	4.3	1.4	0.94	0.86	0.89	3.3	12.0	3.2
A5	0.12	39	1.4	5.2	1.6	0.91	0.85	0.89	4.2	11.9	4.2
A5†	0.12	39	1.4	5.3	1.7	0.80	0.85	0.89	4.3	12.2	4.3
	[0.003]	[0.5]	[0.05]	[0.2]	[0.1]	[0.03]			[0.3]	[0.5]	

* Identical runs; listed in multiple locations for clarity

† Repeats with wooden dowels left in place in the clearing

** Indicates equations used to arrive at the predicted values

‡ Indicates measurements from experiment

the cleared area. These runs are marked with a superscript b in Table 3.1. The dynamic influence of this cleared area on both unsteady and steady velocity components is discussed shortly.

The velocity measurements were decomposed into mean (U_c, W_c), root-mean square (RMS) oscillatory ($U_{w,RMS}$, $W_{w,RMS}$) and turbulent (u', w') components using a phase-averaging technique. The velocity readings were binned into different phases based on the upward zero-crossings ($\Phi = 0$ rad) of the synchronous wave elevation measurements. Wave elevation is defined as the instantaneous surface displacement minus the mean water level. The wave crest and wave trough correspond to $\Phi \approx \pi/2$ rad and $\Phi \approx 3\pi/2$ rad respectively. The velocity measurements for each phase bin where then ensemble-averaged for the entire record (180-396 waves, depending on frequency) to yield the phase-averaged velocity values, $u(\Phi)$ and $w(\Phi)$. The mean and RMS velocities were then calculated by performing the following operations (only x-velocities shown for brevity):

$$U_c = \frac{1}{2\pi} \int_0^{2\pi} u(\Phi)\, d\Phi \tag{3.20}$$

$$U_{w,RMS} = \sqrt{\frac{1}{2\pi} \int_0^{2\pi} (u(\Phi) - U_c)^2\, d\Phi} \tag{3.21}$$

Similarly, the turbulent Reynolds stress, $u'w'(\Phi)$, was calculated by subtracting the phase-averaged velocities from the instantaneous velocities, multiplying the vertical and horizontal components, and ensemble-averaging over all data within that phase bin. The time-averaged turbulent Reynolds stress was then calculated as:

$$\overline{u'w'} = \frac{1}{2\pi} \int_0^{2\pi} u'w'(\Phi)\, d\Phi \tag{3.22}$$

3.2.2 Results

A qualitative overview of the observations at the scale of the entire meadow is presented in Fig. 3-2. Upstream of the model seagrass meadow, the RMS oscillatory

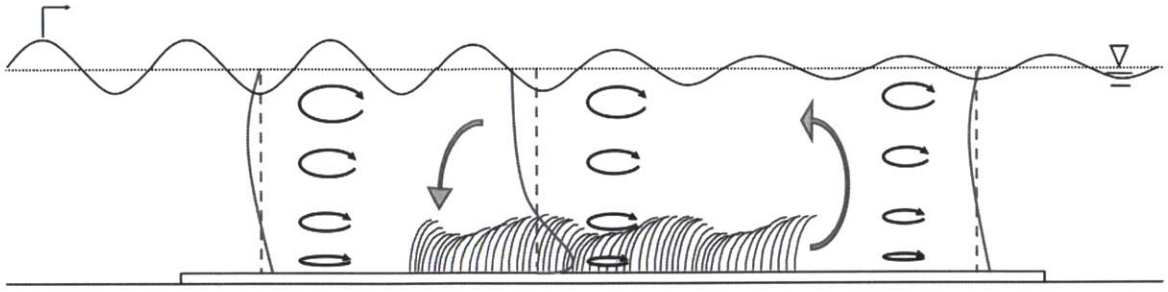

Figure 3-2: A qualitative overview of the flow pattern at the meadow scale. The decay in wave height (fine black line) along the meadow results in a proportional decrease in the oscillatory velocity fields. The black ellipses with arrows indicate the wave orbitals. Vertical profiles of the mean current (heavy gray lines) are shown at an upstream, downstream, and in-meadow position. At each position the vertical dashed lines indicates the axis position for the profile. The local circulation pattern, shown by the large gray arrows results from the difference in the velocity profile within and outside the meadow. The direction of wave propagation is from left to right.

velocities match predicted values based on linear wave theory. A small mean flow is generated close to the bed; the magnitude of this mean current is in reasonable agreement with the Longuet-Higgins [54] solution for induced drift in laminar wave boundary layers. Within the meadow, the waves induce a mean current; this mean current is stronger and extends over a larger vertical distance than the boundary layer drift observed upstream of the meadow. Qualitative observations using a passive tracer (food coloring) indicate that the mean current is established within ~50 cm of the start of the meadow and persists for a similar distance downstream of the meadow, beyond which the velocity structure resembles the observations made upstream of the meadow. Because the flume is a closed system, the wave-induced mean current drives the local circulation pattern indicated by large gray arrows in Fig. 3-2.

The velocity measurements shown in Fig. 3-3 support this qualitative description of the velocity structure. Upstream of the meadow, the RMS oscillatory velocities are predicted to within 5% by linear wave theory (Fig. 3-3a), and the mean velocity is maximum at the measurement location closest to the bed (Fig. 3-3b). The magnitude of this mean current, $U_c = 2.4$ cm s^{-1}, is roughly consistent with the laminar boundary layer solution (Eq. 3.4), which predicts that the induced drift will be $U_c = 1.9$ cm s^{-1} outside the wave boundary layer. For laminar flows, the boundary layer thickness

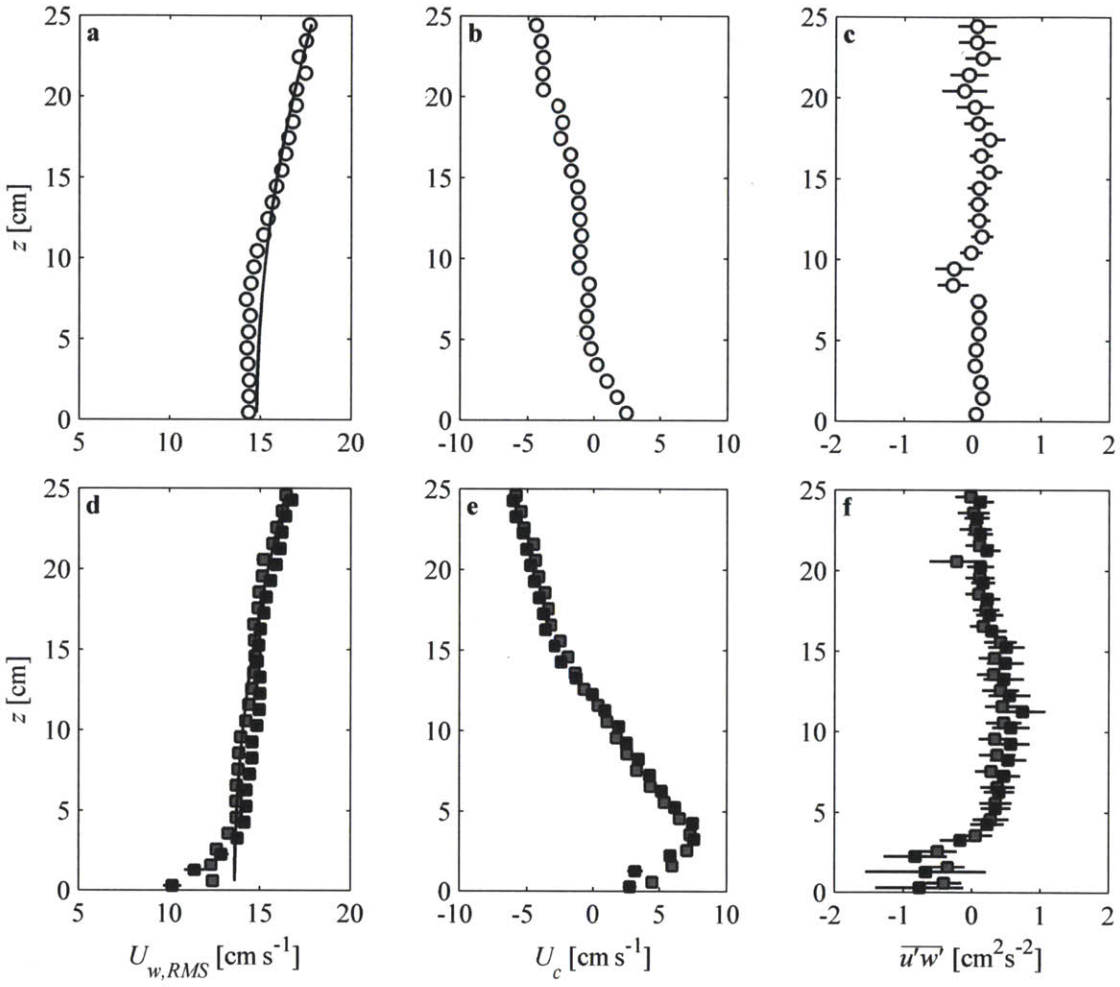

Figure 3-3: Vertical profiles of RMS wave velocity, mean velocity, and Reynolds stress for Run A5 (see Table 3.1). (a-c) correspond to the measurement location upstream of the meadow. (d-f) show profiles for the measurement location within the meadow. Results for the case where a 5 cm radius circle was completely cleared of vegetation are plotted as gray squares. Black squares represent the case where stems were left in this clearing and only blades were removed. Solid lines in panels (a) and (d) represent RMS velocity profiles predicted by linear wave theory, Eq. 3.1.

is $O(\sqrt{\nu/\omega}) \sim 0.05$ cm. Over a smooth bottom, the boundary layer transitions from laminar to turbulent for a wave Reynolds number, $Re_w = U_w A_w/\nu > 5 \times 10^4$ (U_w, A_w correspond to near-bed values, e.g. [31]). For the wave conditions tested here, $Re_w \leq 10^4$. Hence, we expect the bottom boundary layer to remain laminar. Further, the turbulent Reynolds stress (Fig. 3-3c) is essentially zero within uncertainty throughout the water column as expected for linear waves. Note that the Reynolds stress measurements at heights $z = 8.4$ and 9.4 cm are not reliable because these locations correspond roughly to the *weak spots* of the ADV. At this height, acoustic reflections from the bed interfere with the signal from the measurement volume, resulting in occasional spikes in velocity. The spikes tend to be more frequent during set phases of the wave cycle, resulting in a coherent bias of the $\overline{u'w'}$ estimate.

Within the meadow, the RMS oscillatory velocity is reduced relative to predictions based on linear theory below $z \approx 4$ cm (Fig. 3-3d). For the 10 cm clearing completely devoid of model vegetation, the RMS orbital velocity is reduced to 91% of the predicted linear wave velocities at the lowest measurement location ($z = 0.6$ cm, gray squares). However, with the stems left in the clearing, the RMS orbital velocity is reduced to 73% of the value predicted by linear wave theory at $z = 0.3$ cm (black squares). The presence of wooden dowels in the clearing leads to an additional reduction in the RMS orbital velocity for $z \leq 1$ cm, suggesting that our measurements within the meadow underestimate the reduction of RMS velocity because of the clearing. The clearing does not affect the mean current significantly (Fig. 3-3e). The maximum measured mean current is $U_c = 7.3$ cm s^{-1} for the complete clearing and maximum $U_c = 7.6$ cm s^{-1} with the stems left in place; these values agree within experimental uncertainty. The mean current recorded at the lowest measurement location is close to that predicted for a laminar boundary layer. The magnitude of this mean current increases away from the bed and is greatest at $z \approx 4$ cm. Because the flume is a closed system, a return current develops above the meadow ($z > 13$ cm). Vertical profiles of the turbulent Reynolds stress are physically consistent with the profiles of mean velocity (Fig. 3-3f). The turbulent stress is opposite in sign to $\partial U_c/\partial z$, and it crosses zero at the same height as $\partial U_c/\partial z \approx 0$.

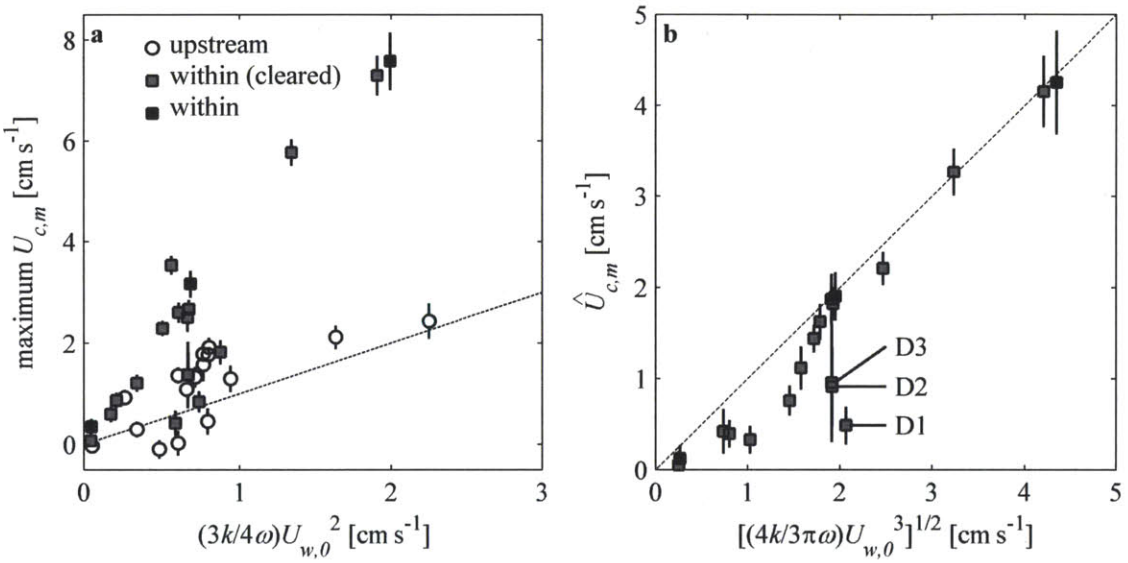

Figure 3-4: Measured mean currents plotted against theoretical predictions. (a) Compares the maximum mean currents with the current induced in laminar boundary layers, Eq. 3.4. White circles represent upstream measurements, gray squares indicate in-canopy measurements for the complete clearing and black squares represent repeat in-canopy measurements with the model stems left in place. (b) Compares the canopy-averaged measured current, $\hat{U}_{c,m}$, with the theoretical prediction shown in Eq. 3.19 (gray and black squares as before). Note the different axes scales.

Figure 3-4a compares the maximum mean current measured upstream of, and within, the canopy with the predicted mean velocity for laminar boundary layers Eq. 3.4. Consistent with Fig. 3-3, the maximum measured currents upstream of the canopy agree reasonably well with predicted values for boundary layers. However, the currents generated within the meadow can be 3 to 4 times larger than the laminar boundary layer prediction. The simple theory developed earlier (Eq. 3.19, Fig. 3-4b) gives a better prediction of the measured in-canopy currents. Note that Eq. 3.4 predicts the maximum current outside the boundary layer, while Eq. 3.19 predicts the vertically averaged mean flow in the seagrass meadow. To reflect this, the maximum mean current is plotted in Fig. 3-4a, while the canopy-averaged mean current, $\hat{U}_{c,m}$, is plotted in Fig. 3-4b. $\hat{U}_{c,m}$ is calculated as the vertical average of the measured mean flow profile below the zero crossing for U_c (e.g., $z \leq 13$ cm in Fig. 3-3e).

To arrive at a prediction for in-canopy currents using Eq. 3.19, the following assumptions were made: the in-canopy oscillatory velocity is equal to the near-bed velocity predicted by linear wave theory, $\hat{U}_{w,m} = U_{w,0} = a_w\omega/\sinh(kH)$ (Eq. 3.1), and that the ratio of drag coefficients is $C_{Dw}/C_{Dc} = 1$. With these assumptions, Eq. 3.19 is $\hat{U}_{c,m} = [(4k/3\pi\omega)U_{w,0}^3]^{1/2}$. The use of the near-bottom oscillatory velocity is reasonable because the increase in horizontal oscillatory velocities over the height of the canopy is modest. The ratio of the oscillatory velocity at the top of the canopy to the near-bed velocity based on linear theory (Eq. 3.1) is $\cosh kh < 1.2$ for all the laboratory experiments. Further, vegetation resistance only leads to a limited reduction of in-canopy oscillatory velocities as discussed below. The drag coefficient ratio $C_{Dw}/C_{Dc} = 1$ is chosen based on the range suggested by Zhou and Graham [104], $C_{Dw}/C_{Dc} \approx 0.5 - 1.8$.

For cases D1, D2 and D3 (Fig. 3-4b), the observed mean current is significantly lower than the values predicted. These cases correspond to the lowest stem densities (n_s in Table 3.1) tested here. Deviation at the lowest stem densities is not surprising, as the wave-induced drift must transition back to the boundary-layer streaming below some threshold density. We suggest that the ratio of orbital excursion, $A_{w,\infty}$, to stem center-center spacing, $S = n_s^{-1/2}$, dictates this transition. This is confirmed

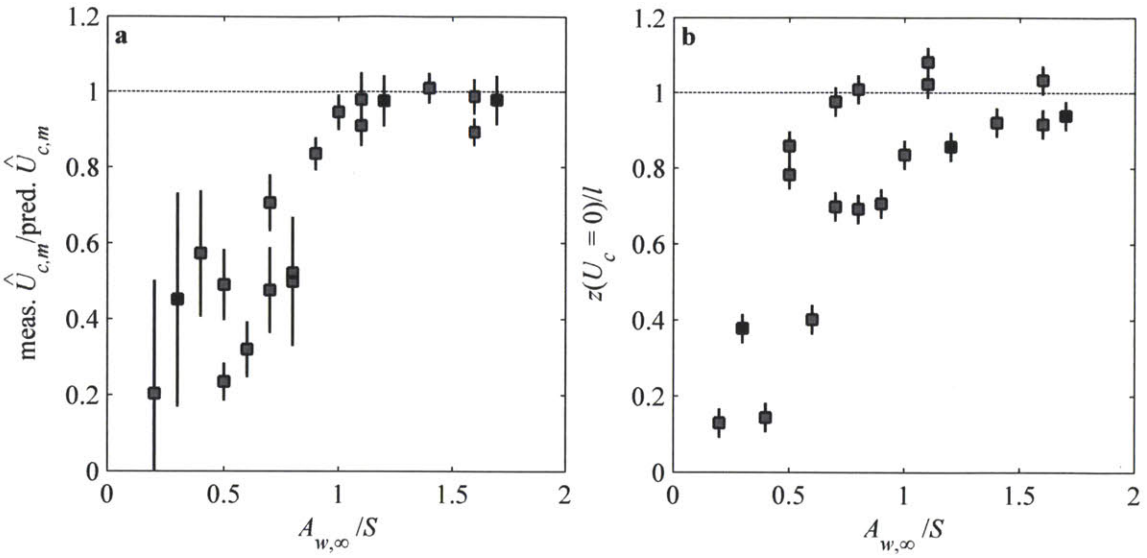

Figure 3-5: (a) Canopy-averaged mean current normalized by the theoretical prediction, plotted against the ratio of orbital excursion to stem center-center spacing. (b) Vertical elevation for the zero crossing in the mean current, $z(U_c = 0)$ normalized by the blade length, l, plotted against $A_{w,\infty}/S$. In both panels, gray squares indicate in-canopy measurements for the runs where a clearing was made for ADV access and black squares represent repeat in-canopy measurements with the model stems left in place.

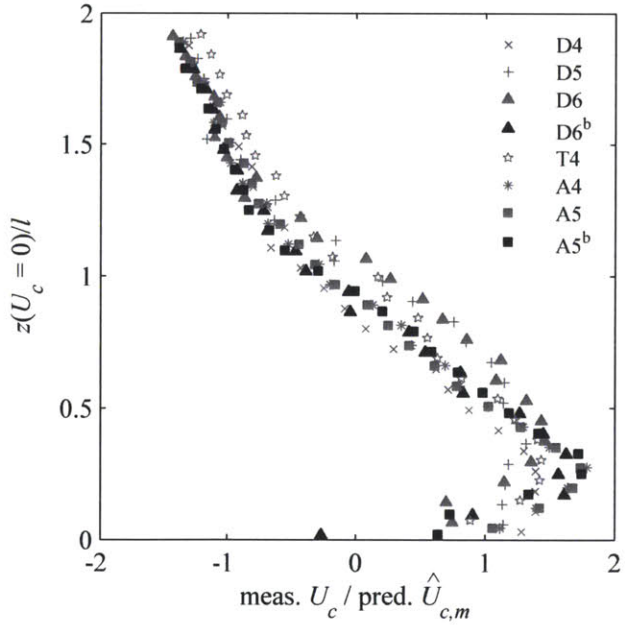

Figure 3-6: Vertical profiles of measured mean velocity, U_c, normalized by magnitude of the wave-driven current, $\hat{U}_{c,m}$ (Eq. 3.19), for all the runs with $A_{w,\infty}/S \geq 1$. The vertical co-ordinate, z, is normalized by blade length, l. Runs as denoted in the legend (see Table 3.1).

by Fig. 3-5a, which shows the observed canopy-averaged mean currents normalized by the predicted values plotted against the ratio $A_{w,\infty}/S$. The observed velocity matches the predictions very well for $A_{w,\infty}/S \geq 1$, while Eq. 3.19 over-predicts $\hat{U}_{c,m}$ for $A_{w,\infty}/S \leq 1$. The vertical extent over which the mean flow is positive within the canopy, $z(U_c = 0)$, is also a function of $A_{w,\infty}/S$ (Fig. 3-5b). The height $z(U_c = 0)$ is roughly equal to the blade length, l, for $A_{w,\infty}/S \geq 1$ but is smaller than the blade length for $A_{w,\infty}/S \leq 1$, consistent with a transition to boundary layer streaming.

If we consider only the cases for which $A_{w,\infty}/S \geq 1$, the measured profiles collapse to a similar form when normalized by the predicted velocity-scale (Fig. 3-6), further confirming the theoretical model. Physically, the large orbital excursions ensure that all the water parcels moving back and forth encounter the model vegetation for $A_{w,\infty}/S \geq 1$. Hence, the bulk representation of seagrass canopy drag employed here is accurate. In contrast, for $A_{w,\infty}/S < 1$, only the water parcels moving back and forth in the vicinity of the model plants interact with vegetation, and the hydrodynamic impact of the canopy on the wave-induced orbital velocities is diminished. In effect, a bulk representation of canopy drag is strictly valid only for $A_{w,\infty}/S \geq 1$. However, if we retain the distributed drag model for simplicity, the wave canopy drag coefficient is reduced for $A_{w,\infty}/S < 1$ but not the current drag coefficient, resulting in a lower ratio, C_{Dw}/C_{Dc} (and therefore, a lower predicted value for $\hat{U}_{c,m}$).

Next, we consider the reduction in oscillatory velocity within the canopy, which is characterized by the ratio of observed to predicted (from linear theory) RMS velocities. The velocity reduction is estimated for all cases at $z = 1$ cm. When measurements are not available at $z = 1$ cm, we interpolate linearly between the two lowest velocity measurements. The resulting velocity ratio, α ($z = 1$ cm) is listed in Table 3.1. Table 3.1 also lists velocity reductions predicted by Eq. 3.9 for the inertia-dominated limit, and by the general solution, Eq. 3.8. The elevation $z = 1$ cm was chosen as the basis for comparison for two reasons. First, velocity reductions were greatest near the bed, making the relative uncertainty smaller. Second, $z \leq 1$ cm corresponds to the stem region. For $z > 1$ cm, the forces exerted by the vegetation depend on the relative motion between the water and the flexible blades.

Table 3.2: Observed and predicted velocity ratio for unidirectional flow over seagrass model; data from Ghisalberti and Nepf [35]. Run numbers follow convention used by the above authors. The last row in the table indicates typical uncertainty.

Run	h [cm]	$C_D a$ [cm^{-1}]	C_v *	α_c *	α_c (3.10) †
F1	21.5	0.064	0.08	0.22	0.25
F2	21.3	0.060	0.06	0.23	0.21
F3	20.0	0.047	0.06	0.22	0.24
F4	18.6	0.045	0.06	0.23	0.27
F5	17.0	0.040	0.05	0.26	0.26
F6	15.5	0.034	0.04	0.28	0.27
	[0.5]	[0.003]	[0.01]	[0.01]	[0.01]

* Estimated based on measurements

† Indicates equation used

Since the elevation $z = 1$ cm corresponds to the stem-region, the velocity reduction for the inertia-only limit is calculated using a value of ϕ for the stems, $\phi = \pi n_s d_c^2/4$. The added mass coefficient is assumed to be $C_M = 1$, as is the case for cylinders. To estimate the velocity reduction using the general solution (Eq. 3.8), we assume to the frontal area parameter to be $ah = n_s d_c h_s + nlb$, where $h_s = 1$ cm is the height of the stem. Further, we use a drag coefficient, $C_D = 1$, based on the typical value for cylinders at $Re \geq O(100)$, and a shear coefficient, $C_v = 0.05$, based on velocity and Reynolds stress profiles measured by Ghisalberti and Nepf [35] for a similar model vegetation in unidirectional flow (see Table 3.2, and discussion below).

As Table 3.1 shows, for all the wave conditions tested here, there is very little difference between velocity reductions predicted by the general solution compared to the inertia-dominated limit. This is in agreement with Lowe et al. [55], who note that the general solution diverges substantially from the inertia-dominated limit only when the wave excursion to spacing ratio, $A_{w,\infty}/S$, is greater than unity; this ratio is smaller than 2 for all the cases tested here. Consistent with the observation made earlier, the measured velocity ratio is higher than predicted for most of the cases where the model vegetation was removed to allow ADV access. The wave-induced flow adjusts locally to the clearing; hence, the removal of the model vegetation results in higher velocities locally. For the cases where the model stems were left in place in

the clearing, agreement between the observed and predicted velocity ratios improves. Given that the smallest velocity ratio we observe is 80% (i.e., a reduction of 20%), the experiments suggest that the reduction in oscillatory velocities within seagrass meadows is limited for wave-dominated conditions, consistent with the assumptions made in predicting the wave-induced mean current.

In contrast, velocities are significantly reduced in seagrass meadows for unidirectional flows (Ghisalberti and Nepf [35]), as shown in Table 3.2. Ghisalberti and Nepf [35] measured unidirectional velocity profiles over a similar model seagrass meadow of density 230 stems m^{-2} (1380 blades m^{-2}). As expected for flexible meadows, the canopy height h decreased with increasing flow speed (Table 3.2). The compression of blades with increasing flow speed makes the interface with the overflow hydraulically smoother, reducing the friction coefficient of this interface (C_v), a trend that was also noted by Fonseca and Fisher [26]. The blade density considered by Ghisalberti and Nepf [35] is at the lower limit of the conditions used here for the wave experiments (Table 3.1), yet the velocity ratio is $\alpha_c \leq 0.28$, i.e., a reduction of 72% or more. With denser meadows, the reduction will be greater. For a typical dense canopy used here (1200 stems m^{-2}, $ah \approx 2.9$), Eq. 3.10 predicts a velocity ratio of $\alpha_c = 0.13$, a reduction of 87%. The implications of these vastly different in-canopy velocities under wave- and current-dominated conditions are discussed in §3.4.

3.3 Field investigation

3.3.1 Study site and methodology

The field study was conducted in Cala Millor, located on the eastern coast of Mallorca, one of the Balearic Islands in the Mediterranean Sea (Fig. 3-7). Cala Millor is an intermediate barred sandy beach in an open, micro-tidal bay (spring tidal range <0.25 m). The bay has an area of approximately 14 km^2, and is exposed to the incoming wind and waves from the East. Within the bay, the seagrass *Posidonia oceanica*, a species endemic to the Mediterranean Sea, forms an extensive meadow at depths

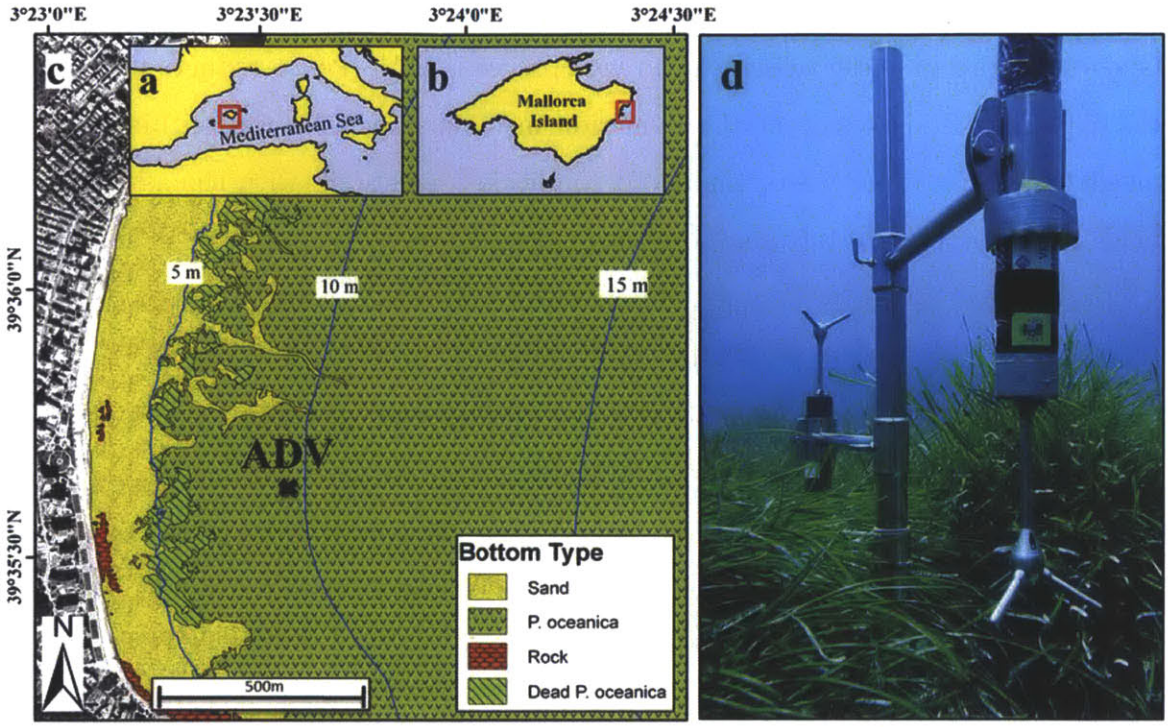

Figure 3-7: Field study location and setup. (a-c) Maps showing field site location. (c) shows depth contours and the bottom type at the measurement location, which is marked with an 'x'. (d) Photograph showing ADV setup.

between 6 m and 35 m [45]. Field measurements [44] suggest the following seagrass meadow properties: mean shoot density, $n = 620 \pm 30$ m^{-2}, mean shoot length, $l = 0.8 \pm 0.1$ m, and an average leaf area of $a'_v = 210 \pm 20$ cm^2 per shoot. The seagrass frontal area per unit bed area is therefore $ah = na'_v = 13 \pm 2$, and assuming a typical blade thickness of $d = 0.5$ mm [61], the seagrass solid volume fraction within the canopy is $\phi = na'_v d/l = 0.008 \pm 0.001$.

Two self-contained ADVs (Nortek Vector) were used to make pressure and velocity measurements at a water depth of $H = 9$ m from July 7th to July 23rd, 2009. The measurement location is shown in Fig. 3-7c. The ADVs were mounted on a stainless steel structure comprising a vertical pole and two horizontal arms. An upward facing ADV measured velocity above the seagrass meadow at a height $z \approx 1.4$ m above the bed, and a downward facing ADV measured velocity within the meadow at $z \approx 0.5$ m (Fig. 3-7d). The pressure sensors for both ADVs were located ≈ 1 m above the sea-bed. Pressure and velocity were measured in bursts of 15 min every two hours

at a sampling frequency of 4 Hz (i.e., $M_s = 3600$ samples in each burst). Each ADV was equipped with a built-in compass and tilt-sensor. So, velocities were recorded in an East-North-Vertical reference frame. Since the contours of bed elevation (and the shoreline, Fig. 3-7c) are oriented roughly North-South at the measurement location, we consider East-West to be the cross-shore direction.

For each burst, we calculated the mean (i.e., time averaged) East- and North-velocities, above and within the seagrass meadow, using a simple arithmetic average of all the individual samples, E_j and N_j, in the measurement burst, e.g.

$$E_c = \frac{1}{M_s} \sum_{j=1}^{M_s} E_j \tag{3.23}$$

The mean velocities were then subtracted from the record to calculate root-mean-square (RMS) oscillatory velocities, e.g.

$$E_{w,RMS} = \sqrt{\frac{1}{M_s} \sum_{j=1}^{M_s} (E_j - E_c)^2} \tag{3.24}$$

As before, we use the subscripts c and w to refer to the mean- and wave-components of velocity, respectively. The variables U_c and U_w refer to the total horizontal velocity, i.e., $|U_c| = \sqrt{E_c^2 + N_c^2}$ and $|U_{w,RMS}| = \sqrt{E_{w,RMS}^2 + N_{w,RMS}^2}$. The magnitude of the wave-induced oscillatory velocities was calculated from the measured RMS velocities assuming perfect sinusoids, i.e., $U_w = \sqrt{2} U_{w,RMS}$. Finally, we use a subscript m to denote in-meadow velocity and a subscript ∞ to denote above-meadow velocity.

The significant wave height, H_S, and peak wave period, T_P, for each burst, were estimated from the velocity measurements using the following procedure. First, the spectral densities, S_E and S_N, for the East- and North- velocities were calculated using Welch's method (MATLAB, MathWorks Inc.). The velocity spectra were then scaled to represent a surface elevation spectrum, S_H, assuming linear wave theory:

$$S_{Hj} = (S_{Ej} + S_{Nj}) \left(\frac{\sinh(k_j H)}{\omega_j \cosh(k_j z)} \right)^2 \tag{3.25}$$

S_{Hj}, S_{Ej}, and S_{Nj}, refer to the spectral densities corresponding to frequency ω_j; k_j

is the wave number. The peak period was estimated as $T_P = 2\pi/\omega_P$, where ω_P is the frequency corresponding to peak in the surface elevation spectrum. Using the standard definition, the significant wave height was calculated as:

$$H_S = 4\sqrt{\sum_j S_{Hj}\Delta\omega_j} \tag{3.26}$$

where $\Delta\omega_j$ is the bandwidth for frequency ω_j. Across all frequencies, the bandwidth was constant, $\Delta\omega_j = 0.0245$ rad, set by the sampling frequency and the algorithm used to calculate spectral densities.

Laboratory measurements described in §3.2.2 show that, above the meadow, oscillatory velocities are predicted reasonably well by linear wave theory. So, we estimated the significant wave height based on above-meadow ADV measurements. Since the velocities within the meadow are likely to be damped, we did not use the in-meadow measurements to calculate H_S and T_P. To limit the effect of any measurement noise on estimates of H_S and T_P, the surface elevation spectrum was restricted to frequencies for which the amplification factor in Eq. 3.25, $\sinh^2(k_jH)/(\omega_j\cosh(k_jz))^2$, was smaller than 200. In effect, this restricts the spectrum to waves of period greater than $T_w = 2.9$ s. The chosen cutoff amplification factor (200) is somewhat arbitrary; however, it does not significantly affect the estimates for H_S. H_S changes by less than 10% if the cutoff is chosen to be 100 ($T_w = 3.05$) or 400 ($T_w = 2.75$). Based on the reported accuracy for the ADVs, we anticipate an instrument uncertainty of approximately ± 0.005 m s^{-1}. Therefore, our subsequent analysis and discussion is limited to period of high wave activity, where $U_{w,RMS} > 0.05$ m s^{-1} (i.e., so that the measurements are $\sim$10 times greater than the uncertainty). Finally, most field studies typically infer surface elevation spectra, Eq. 3.25, from the measured dynamic pressure spectra (see e.g. [8]). Using a procedure similar to the one described above, significant wave heights calculated based on pressure measurements, H_{SP}, showed good agreement with the velocity based estimates, H_S. Specifically, over all the measurement bursts, $H_{SP}/H_S = 1.06 \pm 0.08$ (mean $\pm$ s.d., $N = 178$).

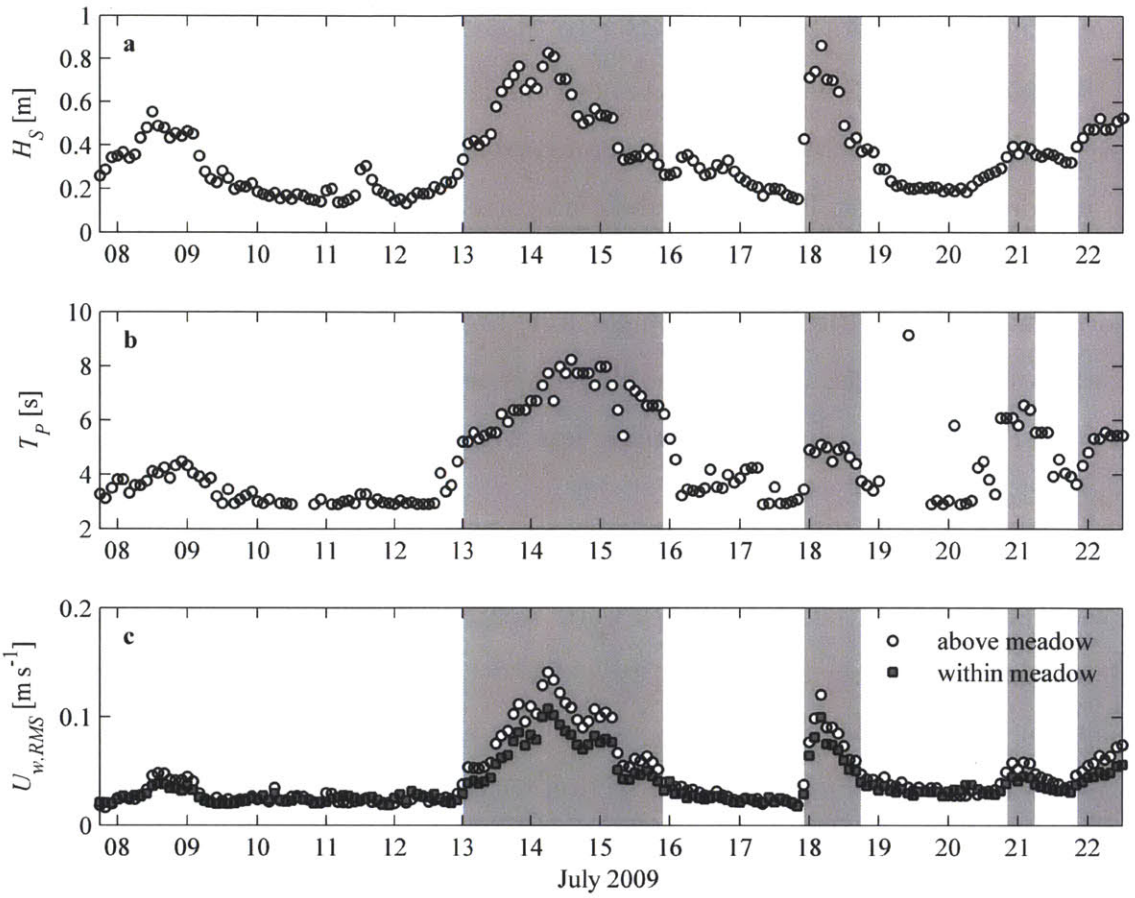

Figure 3-8: (a) Significant wave height, H_S, and (b) peak period, T_P, estimated from velocity measurements made above the meadow. (c) RMS horizontal velocities within and above the meadow (Eq. 3.24).

3.3.2 Results

Figure 3-8 shows the significant wave height, H_S, the peak period, T_P, and the RMS horizontal velocities within and above the meadow over the measurement period. The shaded regions indicate measurement periods with high wave activity, i.e., bursts with $U_{w,RMS} > 0.05$ m s^{-1}. This threshold corresponds roughly to bursts where wave heights exceeded $H_S > 0.35$ m (Fig. 3-8a), and peak periods exceeded $T_P > 4.5$s (Fig. 3-8b). We captured four such periods: on July 13-16, July 18, July 20-21, and July 22. Outside of these high-wave periods, the peak period was typically $T_P \approx 3$s, which is the cutoff frequency described earlier (see e.g., July 10-12). For most of the measurement bursts (and all of the high wave periods), the RMS velocities measured

within the canopy were reduced relative to those above the meadow (Fig. 3-8c).

The plots in Fig. 3-9a,b show that both the Eastern and Northern components of wave velocity measured within the meadow correlated well with those measured above the meadow. However, Fig. 3-9c,d show no correlation for the mean currents. Even during measurement bursts in which mean velocities $|U_{c,\infty}| > 0.05\text{ms}^{-1}$ were recorded above the meadow (Fig. 3-9c, see e.g., July 10-12), the mean currents within the meadow were small, $|U_{c,m}| < 0.01\text{ms}^{-1}$. This is not unexpected because, as discussed above, oscillatory velocities are damped less within vegetated canopies compared to unidirectional currents.

Importantly, our measurements clearly show that a mean current in the direction of wave propagation (i.e., in the Westward, onshore direction) was generated within the meadow during periods of high wave activity (Fig. 3-9d). For example, on July 14, mean currents as large as $|U_{c,m}| \approx 0.04$ m s^{-1} ($\sim$20% of the oscillatory velocity) were measured in the onshore direction within the meadow, while the measured currents above the meadow were smaller, $|U_{c,\infty}| < 0.02$ m s^{-1}. A visual comparison suggests that the magnitude of the onshore currents mirrors the magnitude of the wave velocities (c.f. Fig. 3-9a and b), which is indicative of a wave-driven, streaming phenomenon. During periods of low wave activity, the measured mean currents within the meadow were small, comparable to instrument uncertainty (Fig. 3-10).

Figure 3-10 compares the measured onshore currents, $-E_{c,m}$, with predictions based on the model developed in §3.1.2 (Eq. 3.19). The predictions assumed that the ratio of drag coefficients was $C_{Dw}/C_{Dc} = 1$ as before. The frequency was calculated from the peak period, $\omega_P = 2\pi/T_P$, and the wave number, k_P, was calculated based on the dispersion relation, $\omega_P^2 = k_P g \tanh(k_P H)$. Note that the total wave-velocity measured within the meadow, $U_{w,m}$, was used in Eq. 3.19 to calculate the total streaming velocity in the direction of wave propagation, $U_{c,m}$. The cross-shore component was assumed to be $-E_{c,m} = (E_{w,RMS}/U_{w,RMS})U_{c,m}$.

The predictions show the same trends as the measurements, but the magnitude of the streaming velocity is under-predicted. Fig. 3-11, which shows data from only the high wave periods, suggests that Eq. 3.19 under-predicts the measured currents by a

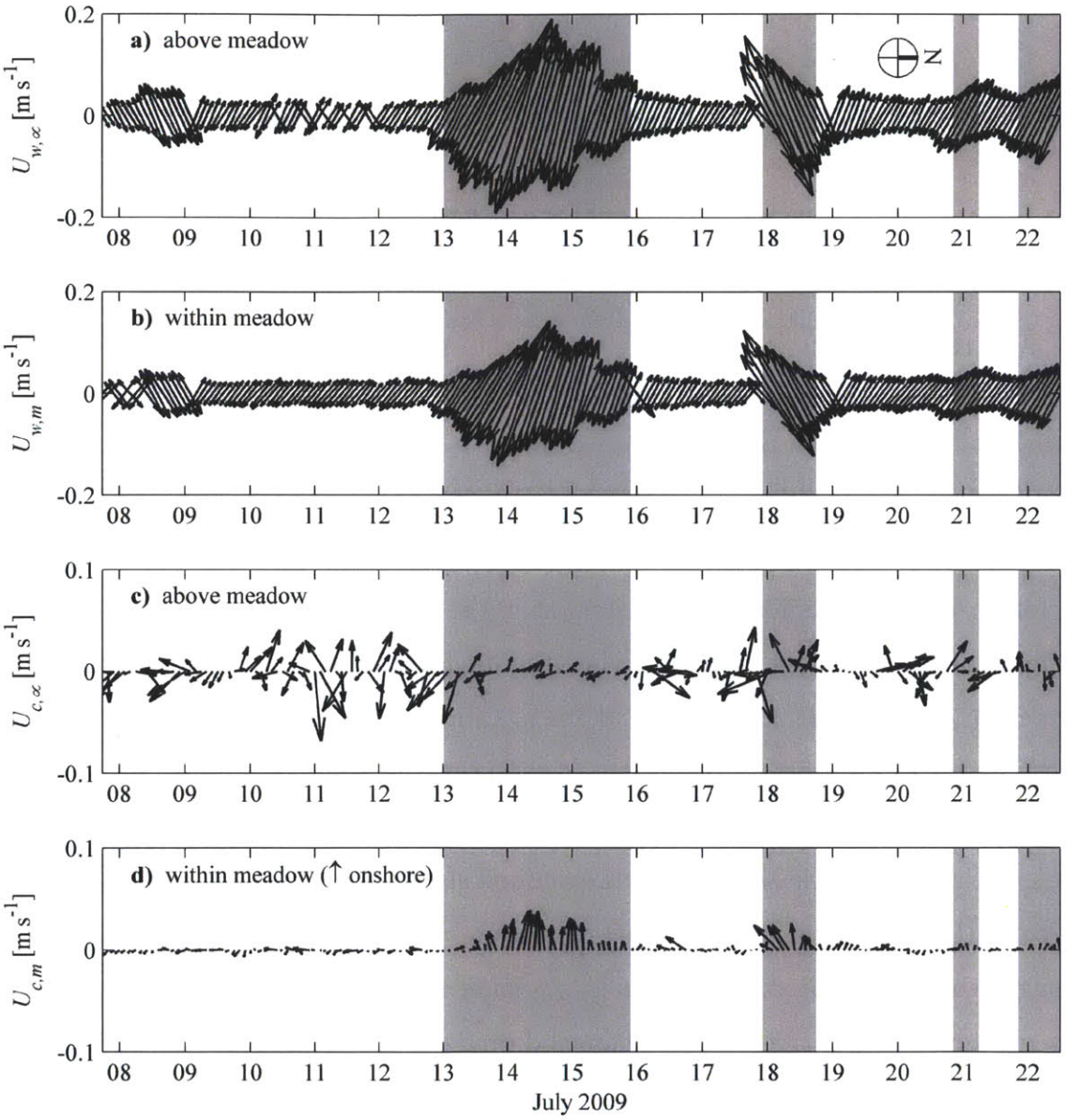

Figure 3-9: (a,b) Wave velocities measured above (a) and within (b) meadow. The shaded regions indicate periods of high wave activity, i.e., with $U_{w,RMS} > 0.05$ m s^{-1} above the meadow. (c,d) Mean velocities measured above (c) and within (d) meadow. North is as indicated in (a). Since the cross-shore direction is approximately East-West (Fig. 3-7), onshore is upwards in this figure (see panel d).

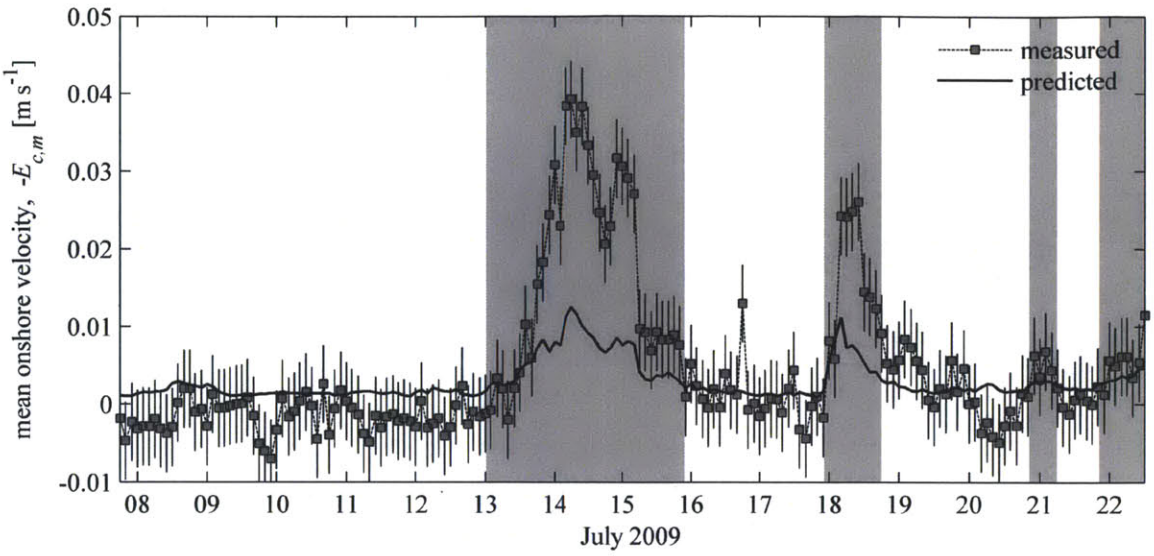

Figure 3-10: Measured onshore mean velocity, $-E_{c,m}$ during the two-week field deployment. Also shown is the predicted streaming velocity, Eq. 3.19 (solid line).

factor of ≈3.9. This difference may stem from the fact that we measured velocities at a single point within the meadow, while the model developed in §3.1.2 is for depth-averaged quantities. It is possible that the measured mean current, $U_{c,m}$, is not representative of the meadow-average, $\hat{U}_{c,m}$. However, we measured velocities at $z \approx 0.5$ m above the bed (or $z/l \approx 5/8$) and the laboratory experiments (Fig. 3-6) indicate that $\hat{U}_{c,m} \approx U_{c,m}$ at this elevation. The predictions also assume that the measured wave velocity ($U_{w,m}$) approximately equals the meadow-average ($\hat{U}_{w,m}$). This assumption, along with any measurement error in $U_{w,m}$, offers another possible explanation for the discrepancy between the measurements and predictions. Although, Eq. 3.19 suggests that $\hat{U}_{c,m} \propto \hat{U}_{w,m}^{3/2}$, and based on this scaling, the wave velocity would have to increase by a factor of ≈ 2.5 (250%) to offset the factor ≈ 3.9 under-prediction in the measured mean current. This is much larger than the measurement error, which was $< 10\%$ during the high-wave periods. Further, wave velocities measured above the meadow, $U_{w,\infty}$, were typically $< 30\%$ greater than the velocities measured within the meadow, $U_{w,m}$ (see Fig. 3-9a,b). Because $U_{w,\infty}$ sets the upper bound for the meadow-averaged wave velocity, $\hat{U}_{w,m}$, any uncertainty arising from the assumption that $\hat{U}_{w,m} \approx U_{w,m}$ is limited to 30% in the upward direction.

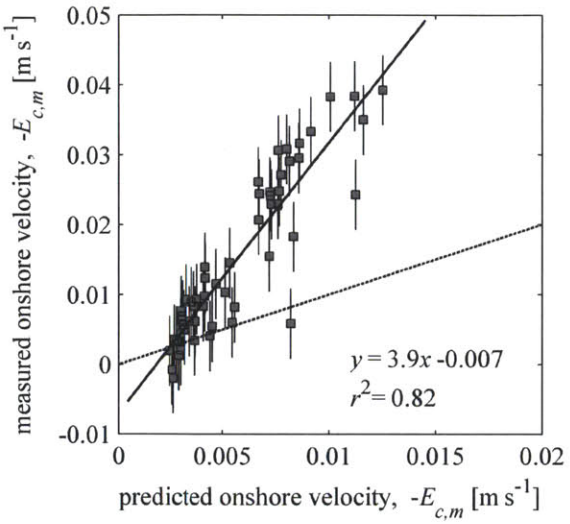

Figure 3-11: Measured onshore mean velocity plotted against the predictions. The dashed line indicates perfect agreement. The solid line and text show the best-fit between measurements and predictions. The main source of error in the measured values is the instrument uncertainty of 0.005 m s^{-1}.

Since experimental limitations do not provide a satisfactory explanation for the factor ≈ 3.9 discrepancy between measured and predicted mean velocities, some of the model assumptions that led to Eq. 3.19 must be reconsidered. Critically, Eq. 3.19 assumes that the vegetation within the meadow remains still and so the water velocity may be used to estimate drag. Natural seagrasses are flexible and move in response to flow, which alters the drag generated by the plants. To account for this effect, the relative velocity between the water and the plants may be used to characterize drag (see §5). Alternatively, retaining the model developed in §3.1.2, the drag coefficients C_{Dw} and C_{Dc} may be calibrated (i.e., lowered) to account for plant flexibility. Further, the predictions for $\hat{U}_{c,m}$ assumed that $C_{Dw}/C_{Dc} = 1$, which was based on numerical simulations for a rigid cylinder in isolation at Keulegan-Carpenter numbers, $KC \leq 26$ [104]. However, we use this value to predict mean currents through a canopy of flexible seagrass at $KC = U_w T_P/b \geq 25$ (assuming $U_w > 0.05$ m s^{-1}, $T_P > 4.5$s, $b = 9$ mm). Based on these factors, we believe that uncertainty in the value for C_{Dw}/C_{Dc} may explain the discrepancy between measured and predicted velocity. Since $\hat{U}_{c,m} \propto \sqrt{C_{Dw}/C_{Dc}}$ (Eq. 3.19), the measured streaming velocities indicate that for flexible seagrasses, the effective value for $C_{Dw}/C_{Dc} (\approx 3.9^2)$ is much higher than

the assumed value (= 1). Unfortunately, the motion of flexible plants in combined wave-current flows is still an open research problem, so we cannot provide a physical explanation for this higher effective ratio.

Figure 3-12 shows the ratio of the oscillatory velocities, $\alpha = U_{w,m}/U_{w,\infty}$. Also shown are the model predictions, Eq 3.8, along with the inertia- and drag- dominated limits, $\alpha_i = 0.87$ and $\alpha_c = 0.05$, given by Eq. 3.9 and Eq. 3.10. Given that seagrass blades resemble flexible flat plates, the predictions assume a flat plate drag coefficient, $C_D = 1.95$. Following Vogel [98], the added mass coefficient was assumed to equal the ratio of the typical blade width (9 mm) to thickness (0.5 mm) for *Posidonia oceanica*, $C_M \approx 18$. The friction coefficient was assumed to be $C_v = 0.05$, as in §3.2.2. In agreement with the predictions, the ratio of measured velocities decreased during periods of high wave activity, i.e., as the wave excursion increased and the effects of shear and drag become more pronounced. The velocity ratio for all the high wave periods was $\alpha = 0.78 \pm 0.03$ (mean $\pm$ s.d., $N = 55$). During the low wave periods, the velocity ratios were roughly unity with $\alpha = 0.95 \pm 0.14$ (mean $\pm$ s.d., $N = 123$), i.e., oscillatory velocities within and above the meadow were comparable. However, measurements made during the low wave periods carried significant uncertainty, and so these results must be interpreted with caution.

Note that, in general, the measured velocity ratios were larger than the predictions (Fig. 3-12). For example, when the predicted ratio was lowest, $\alpha = 0.50$ (July 14), the measured ratio was $\alpha = 0.76$. The following factors may explain why the measured velocity ratios were higher than the predictions. First, the predictions assumed a rigid, upright morphology and a drag coefficient, $C_D = 1.95$, for flat plates. As discussed above, and as we show in §5, for flexible blades moving with the flow, drag and added mass must be calculated based on the *relative* velocity and acceleration between the blade and the water. In effect, accounting for flexibility would decrease C_D (increase L_D), and therefore increase the predicted velocity ratio (see Eq. 3.8 and 3.10). Further, the model predictions are for depth-averaged quantities, while the measurements were made more than half-way up the canopy ($z/l \approx 5/8$). The oscillatory velocity is likely to be reduced to a larger extent lower in the meadow,

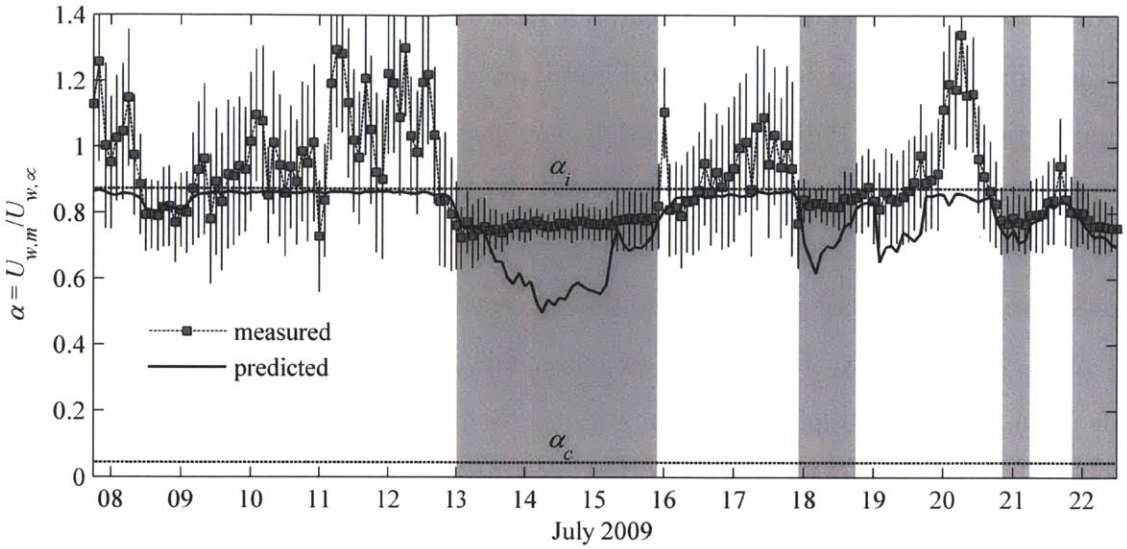

Figure 3-12: Measured ratio of oscillatory velocity within the meadow to that above the meadow, $U_{w,m}/U_{w,\infty}$. Also shown is the predicted ratio, based on Eq. 3.8. The inertia-dominated, α_i (Eq. 3.9), and current-only, α_c (Eq. 3.10), limits are shown as horizontal dashed lines.

where the seagrasses do not move as much.

3.4 Discussion

Perhaps the most interesting aspect of this study is the wave-induced mean current generated within (both model and real) seagrass canopies. A significant body of analytical, numerical and experimental work regarding wave-induced mean currents within laminar and turbulent boundary layers over smooth, rippled and rough beds already exists (see e.g., Davies and Villaret [12] and Marin [62] for relatively recent reviews). However, to our knowledge, this is the first instance of a similar current being observed within submerged canopies. For field applications, our results suggest that in addition to wind- and tidal-forcing, mean currents within submerged canopies can also be induced by wave forcing.

While the simple energy- and momentum-balance model (Eq. 3.19) developed in §3.1.2 predicts the mean currents measured in the laboratory reasonably well, it under-predicts the mean currents measured in the field by a factor of $\approx$4. Eq. 3.19

requires that the ratio of the wave and current drag coefficient, C_{Dw}/C_{Dc} be known. We assume that this ratio is equal to 1 based on numerical simulations performed for a single rigid cylinder [104]. Unfortunately, the drag generated by a single flexible plant in purely steady and oscillatory flows is still the subject of active research (see §4 and §5), and to our knowledge, no previous studies have considered combined wave-current flows. So, the value of C_{Dw}/C_{Dc} could be very different for a single flexible plant, let alone for a canopy of flexible vegetation. For example, qualitative observations of our model meadow indicate that the induced drift introduces an asymmetry in blade posture, whereby the blades lie stream-wise in the direction of wave propagation under the wave crest, and remain more upright under the wave trough. The resulting increase in frontal area may lead to greater drag under the wave trough, when the horizontal oscillatory velocity is negative, thereby reinforcing the mean current. For a plant canopy, wake interactions between neighboring plants could also influence the drag coefficients.

The generation of a mean current within submerged seagrass meadows has important implications for the health of meadows, and for the ecologic services provided by the seagrasses. For example, the mean current can lead to a bias in blade posture over a wave cycle. Blade posture can control light uptake and hence, productivity in seagrass meadows [105]. The mean current can also introduce a directional bias in the dispersal of spores, thereby dictating the direction of meadow expansion. Further, the mean currents induced within the meadow may play a role in mediating the economically important nutrient cycling services provided by seagrasses. Nutrient cycling slows down if the rate at which seagrasses extract nutrients from the water is faster than the rate at which the water, and hence nutrients, are replenished within the meadow as a whole. In oscillatory flows, one mechanism of water renewal for seagrass meadows is turbulent exchange with the overlying water column. By systematically flushing the meadow (see Fig. 3-2), a wave induced mean current may provide a second mechanism of water renewal. Notably, the wave-induced current also has the potential to transport sediment and organic matter in the direction of wave propagation. Oscillatory wave velocities can generate turbulence close to the

bed and suspend sediment, but can only move the suspended sediment back and forth. In contrast, the wave-induced current can advect the material away.

Finally, the weaker damping of in-canopy velocity observed for oscillatory flows compared to mean currents may lead to different horizontal spatial structure within a meadow. In the presence of currents, a meadow can greatly reduce the near-bed velocity (Table 3.2), and hence bed stress, e.g., as shown in Fig. 2.1.2. This can create a feedback that maintains a fragmented meadow structure. For unidirectional flows, an isolated patch of seagrass reduces the bed stress within the patch, and the diversion of flow away from the patch enhances the bed stress on the adjacent bare bed. Similarly, flow is enhanced locally within channels cutting through the meadow, inhibiting regrowth and thereby stabilizing the channels [96]. The scenario is different in wave-dominated conditions, because the meadow does not significantly reduce near-bed velocity (and bed stress) relative to the adjacent bare bed, e.g., as seen in Table 3.1. When a local area of meadow is lost, the bed stress in the bare patch does not increase appreciably, and the vegetation can grow back.

Based on this difference in wave- and current-dominated conditions, we anticipate that regions dominated by current will have more fragmented meadows, because any channels and cuts in the meadow will be maintained by the local adjustment in near-bed flow and bed stress. In contrast, regions dominated by waves will have more uniform vegetation distributions, because under waves there is little local flow adjustment to the meadow. Some support for the above hypothesis can be found in the field literature. Fonseca et al. [29] observed that as the hydrodynamic conditions became more current-dominated, the meadows became more fragmented. Similarly, Fonseca and Bell [24] measured the percent of meadow cover across 50 m $\times$ 50 m plots and found higher correlations in linear regression between percent cover and current ($r^2 = 0.60$) than between percent cover and wave exposure ($r^2 = 0.45$). Using a multiple regression, they found that percent cover was predominately explained by current ($r^2 = 0.54$) with only a minor contribution from wave exposure ($r^2 = 0.07$).

THIS PAGE INTENTIONALLY LEFT BLANK

Chapter 4

Reconfiguration of flexible aquatic vegetation in steady flow

This chapter characterizes the drag generated by flexible aquatic vegetation in steady, uniform flow. In §4.1, we develop a model that calculates vegetation posture based on a force balance involving vegetation stiffness, buoyancy, and the hydrodynamic forcing. For simplicity, we develop the model for individual blades with rectangular cross-sections, characteristic of seagrasses. However, the same physical principles hold for other morphologically complex salt- and freshwater vegetation. Indeed, the model is able to predict posture and drag for laboratory experiments with model blades (§4.3.1), as well as real seagrasses, and marine macroalgae of more complex morphology (§4.3.2). Most of this chapter is published as Luhar and Nepf (2011) [58]. However, in §4.4.2, we link blade-scale reconfiguration with canopy-scale hydrodynamics using the simplified two-layer framework developed in §2.1.3; this is an excerpt from Luhar and Nepf (2012) [57].

4.1 Theory

To develop a model describing the flow-induced reconfiguration of buoyant, flexible seagrass blades, we start with a few simplifying assumptions. First, we assume that the blades can be modeled as isolated, buoyant, inextensible elastic beams of constant

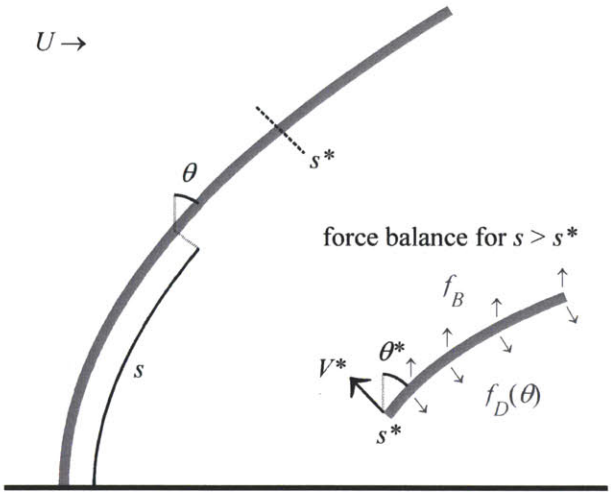

Figure 4-1: Schematic showing the coordinate system and force balance used to derive the mathematical model for the flow-induced reconfiguration of aquatic vegetation.

width b, thickness d, density ρ_v, and elastic modulus E. Second, the horizontal velocity U is uniform over depth. Third, we consider steady flow where the dominant hydrodynamic force is form drag. Viscous skin friction is assumed to be negligible. In §4.4, we discuss how the model can be modified to account for more complex vegetation morphologies as well as spatial variations in vegetation and flow properties. We also develop a formal criterion to indicate when skin friction becomes important. Unsteady flows, such as those induced by surface waves, are considered in §5.

We use the curvilinear coordinate system shown in Fig. 4-1, in which s is the distance along the blade from the base and θ is the local bending angle of the blade relative to the vertical ($\theta = 0$ denotes an upright posture). The blade length is l, so that $s = l$ represents the tip of the blade. Form drag, which derives from the velocity normal to the blade surface, is represented using a standard quadratic law. The drag force per unit blade length is:

$$f_D = (1/2)\rho C_D b U^2 \cos^2\theta \tag{4.1}$$

Where ρ is the density of the water and C_D is the drag coefficient [5, 84]. The drag force is resisted by blade stiffness and blade buoyancy. The blade-normal restoring

force due to stiffness (V) is the spatial derivative of the internal bending moment, $M = EI(d\theta/ds)$, i.e.,

$$V = -EI\frac{d^2\theta}{ds^2} \tag{4.2}$$

where $I(= bd^3/12)$ is the second-moment of area [2, 36]. The vertical buoyancy force per unit blade length is:

$$f_B = \Delta\rho g b d = (\rho - \rho_v) g b d \tag{4.3}$$

The inset in Fig. 4-1 shows the blade-normal force balance for $s \geq s^*$, where s^* is an arbitrary position along the blade. This force balance yields the governing equation for posture:

$$V^* + \int_{s^*}^{l} f_B \sin\theta^* \, ds = \int_{s^*}^{l} f_D \cos(\theta - \theta^*) \, ds \tag{4.4}$$

V^* is the blade-normal restoring force due to stiffness at $s = s^*$, and θ^* is the bending angle at $s = s^*$. The buoyancy force acts vertically and so the component of buoyancy acting in the direction of V^* is $f_B \sin\theta^*$ per unit blade length. Hence, the integral on the left-hand side of Eq. 4.4 represents the projection in the direction of V^* of the total buoyancy force for $s \geq s^*$. Similarly, f_D is the blade-normal drag force per unit length, and so the integral on the right-hand side represents the projection in the direction of V^* of the total drag force for $s \geq s^*$. A force balance parallel to the blade would yield an expression for the blade tension at s^*. However, we do not explicitly calculate blade tension here. Using the complete expressions for f_B (Eq. 4.3) and f_D (Eq. 4.1), and evaluating the integral on the left-hand side, Eq. 4.4 can be rewritten as:

$$-EI\frac{d^2\theta}{ds^2}\bigg|_{s^*} + \Delta\rho g b d(l - s^*)\sin\theta^* = \frac{1}{2}\rho C_D b U^2 \int_{s^*}^{l} \cos^2\theta \cos(\theta - \theta^*) \, ds \tag{4.5}$$

To make Eq. 4.5 dimensionless, we replace s with a normalized coordinate $\hat{s} = s/l$ so that $\hat{s} = 1$ represents the tip of the blade and $\hat{s}^* = s^*/l$ is an arbitrary position along the blade, as before. With this normalization, the curvature term in Eq. 4.5 scales as $|d^2\theta/ds^2| \sim 1/l^2$, and the restoring force due to blade stiffness scales as EI/l^2. This scaling is reasonable when the blade bends gradually over its entire length. For streamlined postures, however, the blades bend significantly over a short distance close to the bed, producing curvature that is much larger than $1/l^2$. Therefore, keep in mind that the scale EI/l^2 underestimates the restoring force due to blade stiffness when bending occurs locally, e.g., only near the bed.

Dividing Eq. 4.5 by the factor EI/l^2 yields the following dimensionless equation for posture, i.e., describing $\theta^* = f(\hat{s}^*)$

$$-\frac{d^2\theta}{d\hat{s}^2}\bigg|_{\hat{s}^*} + B(1-\hat{s}^*)\sin\theta^* = Ca\int_{\hat{s}^*}^{1}\cos^2\theta\cos(\theta-\theta^*)\,d\hat{s} \tag{4.6}$$

Posture is essentially controlled by two dimensionless parameters:

$$B = \frac{\Delta\rho g b d l^3}{EI} \tag{4.7}$$

$$Ca = \frac{1}{2}\frac{\rho C_D b U^2 l^3}{EI} \tag{4.8}$$

Physically, B represents the ratio of the restoring force due to buoyancy and the restoring force due to stiffness. We call this the buoyancy parameter. Ca is the Cauchy number, which indicates the relative magnitude of the hydrodynamic drag and the restoring force due to stiffness. Finally, we impose the following boundary conditions: the base of the blade is a clamped joint, $\theta = 0$ at $\hat{s} = 0$, and the tip of the blade is free, $d\theta/d\hat{s} = 0$ at $\hat{s} = 1$.

Crucially, B and Ca reflect the assumptions made in order to normalize Eq. 4.5. Specifically, the drag and buoyancy scales represent the maximum possible values for these forces, whereas the scale EI/l^2 can underestimate the stiffness restoring force, as discussed previously. The potential mismatch in scales is evident in Eq. 4.6. The term

reflecting the buoyancy force is proportional to the factor $(1 - \hat{s}) \sin\theta$ which cannot exceed 1. Similarly, the value of the integral on the right-hand side, representing the drag force, also cannot exceed 1. However, the curvature term is unbounded. For streamlined postures, where blade curvature is large close to the bed, $|d^2\theta/d\hat{s}^2| \gg 1$, the restoring force due to blade stiffness is larger than that suggested by the scale EI/l^2.

Reconfiguration reduces drag through two different mechanisms. First, reconfiguration reduces the frontal area of the vegetation, and second, the reconfigured shape tends to be more streamlined [13]. To quantify the reduction of drag due to reconfiguration we propose an effective blade length, l_e. This is defined as the length of a rigid, vertical blade that generates the same horizontal drag as the flexible blade of total length l. In dimensionless terms, the effective length is:

$$\frac{l_e}{l} = \frac{\int_0^l (1/2)\rho C_D b U^2 \cos^3\theta \, ds}{(1/2)\rho C_D b l U^2} = \int_0^1 \cos^3\theta \, d\hat{s} \tag{4.9}$$

Based on this definition, the total horizontal drag force is $F_x = (1/2)\rho C_D b l_e U^2$, where the drag coefficient, C_D, for the flexible blades is identical to that for rigid, vertical blades. The effective length is equal to the blade length, $l_e = l$, if the blades remain upright in flow ($\theta = 0$). As the blades are pushed over ($\theta > 0$), the effective length decreases so that $l_e < l$. Note that the effective length defined in Eq. 4.9 accounts for drag reduction both due to the reduced frontal area in the reconfigured state, and due to the more streamlined shapes of the bent blades. In contrast, the deflected vegetation height, often used to quantify drag reduction due to reconfiguration, accounts only for a reduction in frontal area. For the coordinate system used here, the dimensionless deflected height of the blades is:

$$\frac{h}{l} = \int_0^1 \cos\theta \, d\hat{s} \tag{4.10}$$

Comparing Eq. 4.9 and 4.10, it is clear that the effective length is always less than, or equal to, the deflected height, $l_e \leq h$.

4.1.1 Model predictions

Before describing the general case, where both blade buoyancy and stiffness play a role, we first consider the two limiting cases: zero stiffness and zero buoyancy. For the zero stiffness case, Eq. 4.6 simplifies to:

$$(1 - \hat{s}^*) \sin\theta^* = (B^{-1}Ca) \int_{\hat{s}^*}^{1} \cos^2\theta \cos(\theta - \theta^*)\, d\hat{s} \tag{4.11}$$

The parameter $B^{-1}Ca$ represents the ratio of the drag force and the buoyancy force. With zero stiffness, the blade cannot sustain any internal bending moments. Hence, the boundary condition at the base of the vegetation changes from a clamped joint to a pin joint, $d\theta/d\hat{s} = 0$ at $\hat{s} = 0$. Further, because there is no restoring force due to blade curvature, the angle θ reflects the local balance between drag and buoyancy. Since the model does not consider any spatial variations in blade density or flow speed, the angle θ is constant along the blade. This is evident by balancing the blade-normal components of the forces shown in Eq. 4.1 and 4.3. If b, d, $\Delta\rho$ and U are constant along $\hat{s}$, θ must also be. As a result, Eq. 4.11 simplifies further to:

$$\sin\theta = (B^{-1}Ca) \cos^2\theta \tag{4.12}$$

Eq. 4.12 can be solved easily to yield the blade angle, θ, as a function of $B^{-1}Ca$. For θ constant along the blade, the blade remains straight as it tilts over (see Fig. 4-2a, inset), and the effective blade length and deflected height are $l_e/l = \cos^3\theta$ and $h/l = cos\theta$, respectively (Eq. 4.9 and 4.10).

The predicted effective length for the zero-stiffness case is plotted as a function of the parameter $B^{-1}Ca$ in Fig. 4-2a. The inset in Fig. 4-2a shows predicted postures for $B^{-1}Ca = 0.1$ and $B^{-1}Ca = 3.2$. When the hydrodynamic forcing is much smaller than the buoyancy force, $B^{-1}Ca \ll 1$, the blade remains upright in flow. Specifically, the effective length is approximately equal to the blade length, $0.9 < (l_e/l) < 1$, for $B^{-1}Ca < 0.25$. As the hydrodynamic forcing increases relative to the buoyancy force, the blade is pushed over and the effective length is reduced. As an example,

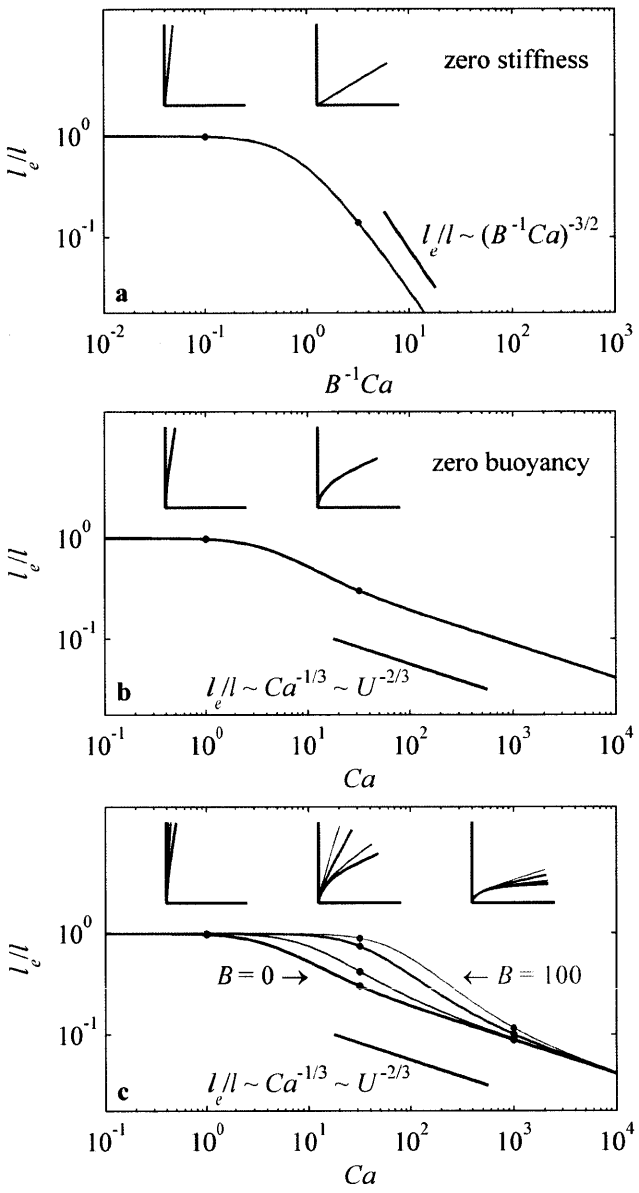

Figure 4-2: Model predictions for the effective blade length l_e/l and blade posture. (a) Effective blade length plotted against the ratio of hydrodynamic forcing and blade buoyancy, $B^{-1}Ca$, for zero-stiffness blades. Also shown are predicted blade postures for the cases marked with a dot: $B^{-1}Ca = 0.1$ and $B^{-1}Ca = 3.2$. (b) Effective blade length plotted against the Cauchy number, Ca, for blades that are neutrally buoyant. The blade postures shown in the left and right subplots correspond to the cases marked with a dot, $Ca = 1$ and $Ca = 32$, respectively. (c) Effective blade length plotted against the Cauchy number for four different values of the buoyancy parameter: $B = 0$ (bold black line), 10 (fine black line), 50 (bold gray line), and 100 (fine gray line). The predicted blade postures shown in the subplots correspond to the cases marked with a dot, $Ca = 1$, $Ca = 32$, and $Ca = 1000$, from left to right, respectively.

for $B^{-1}Ca = 3.2$, $\theta = 59^o$, the effective length is $l_e/l = 0.14$, and the deflected height is $h/l = 0.52$, as shown in Fig. 4-2a. For $B^{-1}Ca \gg 1$, the blade is pushed toward a near-horizontal posture, for which $\sin\theta \approx 1$, and Eq. 4.12 simplifies to $\cos\theta \sim (B^{-1}Ca)^{-1/2}$. In the limit of large $B^{-1}Ca$, therefore, the deflected height and effective length are $(h/l) \sim (B^{-1}Ca)^{-1/2}$ and $(l_e/l) \sim (B^{-1}Ca)^{-3/2}$, respectively (Fig. 4-2a). The Cauchy number (Eq. 4.8) is proportional to the square of the velocity, $Ca \propto U^2$, and so the above scaling implies that for $B^{-1}Ca \gg 1$, the effective length is inversely proportional to the velocity cubed, $l_e \propto U^{-3}$, and the horizontal drag decreases with increasing velocity, $F_x \propto U^2 l_e \propto U^{-1}$. More generally, for $B^{-1}Ca > 1$, the effective length decreases with increasing velocity as $(l_e/l) \sim (B^{-1}Ca)^{-\hat{A}}$, where the generic exponent $\hat{A}$ is greater than 0.5. Hence, the horizontal force, $F_x \propto U^2 l_e \propto U^{(2-2\hat{A})}$, increases sub-linearly with velocity. That is, $F_x \propto U^A$ with $A = (2 - 2\hat{A}) < 1$.

Next we consider the case where only blade stiffness is important the zero-buoyancy case. For this case, the boundary condition at the base is a clamped joint, with $\theta = 0$ at $\hat{s} = 0$. Because $B = 0$, the governing Eq. 4.6 simplifies to:

$$-\frac{d^2\theta}{d\hat{s}^2}\bigg|_{\hat{s}^*} = Ca \int_{\hat{s}^*}^{1} \cos^2\theta \cos(\theta - \theta^*)\, d\hat{s} \tag{4.13}$$

This equation for blade posture is solved to an accuracy of 10^{-3} in θ using an iterative shooting method (e.g., Stoer and Bulirsch [90], see Appendix B). The predicted effective length (Eq. 4.9) for the zero-buoyancy case is plotted against the Cauchy number in Fig. 4-2b, along with the predicted blade postures for $Ca = 1$ and $Ca = 32$. The model suggests that for $Ca < O(1)$, the hydrodynamic forcing is unable to overcome blade stiffness and the blade remains upright in flow. Specifically, the effective blade length is approximately equal to the blade length, $0.9 < (l_e/l) < 1$, for $Ca < 2$. For these conditions, the drag force increases with the square of velocity, $F_x \propto U^2$. However, as the Cauchy number increases (U increasing), the blade is pushed over by the flow, and both the deflected height and effective blade length decrease. As an example, for $Ca = 32$ (inset, Fig. 4-2b), the effective length is $(l_e/l) = 0.30$ and the deflected height is $(h/l) = 0.61$. Note that the decrease in

effective length with increasing velocity (i.e., increasing Ca) is more gradual for the zero-buoyancy case compared to the zero-stiffness case described above (Fig. 4-2a).

The model predicts that for $Ca \gg 1$, the effective length scales as $(l_e/l) \sim Ca^{-1/3}$ (Fig. 4-2b). This scaling suggests that $l_e \propto U^{-2/3}$ (c.f. $l_e \propto U^{-3}$ for the zero-stiffness case). Hence, the drag force increases with velocity as $F_x \propto U^2 l_e \propto U^{4/3}$, in agreement with the results obtained by Alben et al. [2] and Gosselin et al. [36] for non-buoyant bodies. The scaling $l_e/l \sim Ca^{-1/3}$ emerges directly from the balance of drag and the restoring force due to stiffness. For streamlined postures (e.g., Fig. 4-2b, inset, $Ca = 32$), the blades bend more severely near the base producing a smaller radius of curvature than that implied by the scale $|d^2\theta/ds^2| \sim 1/l^2$ used in Eq. 4.6, and so the restoring force due to blade stiffness is larger than that implied by the scale $EI(1/l)^2$. For bent postures, the effective length, l_e, captures the magnitude of the restoring force more accurately because it reflects the length over which the blade is actually bending, leading to $EI(|d^2\theta/ds^2|) \sim EI(1/l_e)^2$. Since the restoring force due to stiffness and the drag force must balance in the reconfigured state, we have $EI(1/l_e)^2 \sim (1/2)\rho C_D b l_e U^2$. Expressing this balance in dimensionless form (see Eq. 4.8), we see that the effective length scales as $(l_e/l) \sim Ca^{-1/3}$.

We now discuss the general case, where blade buoyancy and stiffness are both important. As before, we solve Eq. 4.6 numerically using an iterative shooting method. The four curves in Fig. 4-2c show effective lengths for the zero-buoyancy case described above, $B = 0$ (bold black line), along with the cases $B = 10$ (fine black line), 50 (bold gray line) and 100 (fine gray line). Comparing these four curves indicates that the addition of buoyancy delays the onset of blade reconfiguration relative to the zero-buoyancy case, i.e., the blades remain upright at higher velocities. For the zero-buoyancy case, the effective length is approximately equal to the blade length, $(l_e/l) \approx 1$, for $Ca < O(1)$. For $B > 1$, the effective length is approximately equal to the blade length as long as the drag force scale does not exceed the buoyancy force scale, $(B^{-1}Ca) < O(1)$, or $Ca < O(B)$. As an example, for $B = 100$, $l_e/l \approx 1$ for $Ca < O(100)$ (Fig. 4-2c). Above these thresholds, the blades are pushed over by the flow and the effective length decreases.

If the hydrodynamic forcing becomes significantly larger than blade buoyancy, $(B^{-1}Ca) \gg 1$, blade stiffness becomes the dominant restoring mechanism. Specifically, all the curves collapse onto the scaling law developed above, $(l_e/l) \sim Ca^{-1/3}$, and the effective length becomes independent of the buoyancy parameter, B. This is illustrated by the predicted blade postures for $Ca = 1000$ (Fig. 4-2c, right-most inset). Close to the base, blade posture is very similar for all four values of the buoyancy parameter, indicating that the curvature close to the bed is set purely by a balance between drag and the restoring force due to blade stiffness. The effect of buoyancy only becomes apparent closer to the top of the blades; the more buoyant blades are raised a bit higher in the water. However, given the near-horizontal orientations, the top of the blades do not generate significant drag. The majority of the drag is generated very close to the base, where the blades are clamped and remain vertical due to blade stiffness. As a result, blade buoyancy does not significantly affect the drag generated, and the effective length becomes independent of the buoyancy parameter.

4.2 Laboratory experiments

To validate the model developed above, we conducted laboratory experiments measuring drag and blade posture for model blades designed to be dynamically similar to seagrasses. Due to variations in material properties, morphology and flow conditions, the buoyancy parameter and Cauchy number vary considerably in natural systems. For example, the typical density of the seagrass *Zostera marina* varies in the range $700-900$ kg m^{-3} [1, 23, 30], so that $\Delta\rho \approx 125-325$ kg m^{-3} (the density of seawater is assumed to be 1025 kg m^{-3}), and the range of reported values for the elastic modulus is $E \approx 0.4 - 2.4$ GPa [8]. *Zostera marina* blades can also vary greatly in length with observations ranging from $l \approx 15 - 200$ cm [33]. Using a more typical blade length range of $l = 30 - 60$ cm, and assuming the blade width and thickness are $b = 0.8$ cm and $d = 0.35$ mm [56], we estimate that the buoyancy parameter (Eq. 4.7) ranges between $B \approx 1 - 170$. For a typical velocity range of $U = 5 - 50$ cm s^{-1}, we estimate the Cauchy number (Eq. 4.8) ranges from $Ca \approx 10 - 40,000$.

To span the estimated range for the buoyancy parameter, we constructed model blades from two different materials, silicon foam (E = 500 kPa; $\Delta\rho$ = 330 kg m^{-3}; d = 1.9 mm) and high-density polyethylene (HDPE, E = 0.93 GPa; $\Delta\rho$ = 50 kg m^{-3}; d = 0.4 mm). We tested model blades of five different lengths ranging from l = 5 cm to l = 25 cm in 5 cm-increments. The blade width was b = 1.0 cm in all cases. For the foam blades, the buoyancy parameter ranged from B = 2.7 for the 5 cm-long blades to B = 340 for the 25 cm-long blades (see Table 4.1). For the HDPE blades, the buoyancy parameter ranged from B = 0.005 for the 5 cm-long blades to B = 0.62 for the 25 cm-long blades (Table 4.1). In general, the foam blades represented buoyancy-dominated cases, while the HDPE blades represented stiffness-dominated cases. All the model blades were subjected to eight different flow speeds, ranging from U = 3.6 cm s^{-1} to U = 32 cm s^{-1}. The maximum value of the Cauchy number tested was Ca = 5500 for the foam blades, and Ca = 320 for the HDPE blades. Note that because the model blades resemble flat plates, these values for the Cauchy number have been calculated based on the drag coefficient for long, flat plates perpendicular to the flow, C_D = 1.95 [98]. Table 4.1 lists the buoyancy parameter and the Cauchy number for all eighty test cases.

For flow speeds smaller than U = 15 cm s^{-1}, the experiments were performed in a 24 m-long, 38 cm-wide and 60 cm-deep re-circulating flume. For flow speeds greater than U = 15 cm s^{-1}, the experiments were carried out in a 28 m-long, 76 cm-wide and 90 cm-deep re-circulating flume. Both flumes had glass sidewalls. A schematic of the experimental set-up is shown in Fig. 4-3. At every flow speed, the horizontal drag force, F_x, acting on a single model blade of each length tested was measured using a submersible s-beam load cell (Futek LSB210). The measurements were logged to a computer using a bridge completion and data acquisition module (National Instruments NI-USB 9237). Based on a calibration with known weights performed prior to the experiments, the resolution of the load cell was 0.001 N and the accuracy was 10%. Two separate calibrations showed that the load cell responded linearly over the range 0 - 0.015 N, and over the range 0 - 0.042 N.

To ensure that the flow did not interfere with the force measurement apparatus,

Table 4.1: List of test cases for the reconfiguration experiments with model blades

			U [cm s^{-1}]							
			3.6	7.1	11	14	16	22	27	32
	l [cm]	B	Ca							
HDPE	5	0.005	0.032	0.12	0.28	0.5	0.66	1.2	1.8	2.5
$E = 0.93 \pm 0.08$ GPa	10	0.04	0.25	0.99	2.2	4	5.3	9.3	15	20
$\Delta\rho = 50 \pm 10$ kg m^{-3}	15	0.13	0.86	3.3	7.5	14	18	32	50	68
$b = 1.0 \pm 0.05$ cm	20	0.32	2	7.9	18	32	42	75	120	160
$d = 0.4 \pm 0.04$ mm	25	0.62	3.9	15	35	63	83	150	230	320
Silicon foam	5	2.7	0.55	2.1	4.8	8.7	11	20	32	44
$E = 500 \pm 60$ kPa	10	22	4.4	17	38	70	92	160	260	350
$\Delta\rho = 330 \pm 50$ kg m^{-3}	15	73	15	58	130	240	310	550	860	1200
$b = 1.0 \pm 0.05$ cm	20	170	36	140	310	560	730	1300	2000	2800
$d = 1.9 \pm 0.10$ mm	25	340	69	270	600	1100	1400	2500	4000	5500

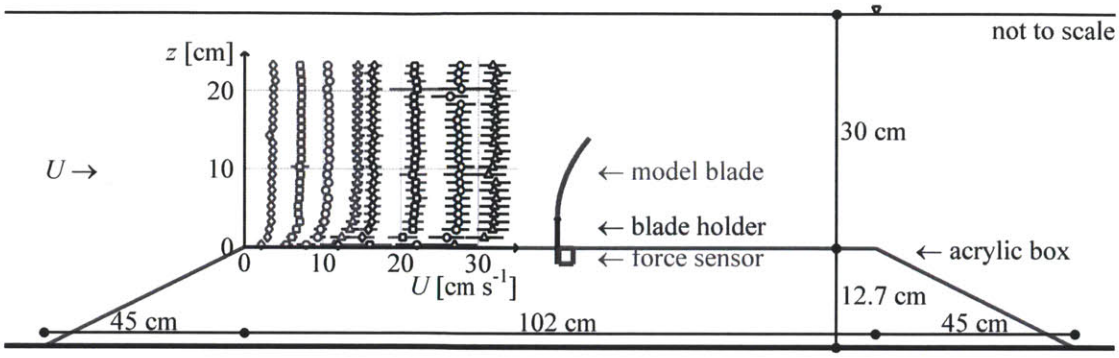

Figure 4-3: Schematic of the experimental set-up. Also shown are the measured profiles of velocity for the eight different flow speeds tested in this study (Table 4.1). Note the vertical exaggeration.

the load cell was housed inside a trapezoidal, acrylic box of length 192 cm and height 12.7 cm, as shown in Fig. 4-3. In all cases, the total water depth was $H = 42.7$ cm, so that the depth of the water above the acrylic box was 30 cm. The load cell was fixed to the top surface of the box, midway along the length of the box. A cylindrical, stainless steel blade holder, which protruded through a hole of diameter 1.25 cm, was used to attach the model blades to the load sensor (Fig. 4-3). The blade holder extended 4 cm above the top of the box. As a result, the model blades were positioned above the bottom boundary layer, ensuring a uniform flow speed over the length of the blade. Prior to the experiments, we measured vertical profiles of velocity above the acrylic box using an ADV (Nortek Vectrino) for all eight flow speeds. We measured the velocity profiles midway along the box at a vertical resolution of 1 cm. At each measurement location, 4-min records were obtained at 25 Hz. The vertical profiles, shown in Fig. 4-3, confirm that the horizontal flow speed varied by less than 5% above blade holder. Note that the velocity values, U , listed in this chapter denote the mean horizontal flow speed above the blade holder.

Force measurements were made for a period of 4 min at a sampling rate of 2 kHz (i.e., 480,000 samples). The drag force was calculated based on the arithmetic mean of all the samples. We also measured the force generated by the blade holder alone for each of the eight flow speeds tested. In order to estimate the drag force generated by the blades alone, the drag generated by the blade holder was subtracted from the

total drag (i.e., blade holder and blade). In addition to measuring the drag force, we also photographed the model blades for each flow speed using a digital still camera (Nikon D60). Multiple photographs were taken for each test case to account for any short-term fluctuations in blade posture.

4.3 Results

4.3.1 Model blades

Figure 4-4 shows force measurements (Fig. 4-4a,b) and observed blade postures (Fig. 4-4c-f) for the shortest (5 cm) and longest (25 cm) model blades tested. Vortex-induced vibrations of the HDPE blades were observed at velocities greater than 20 cm s^{-1}. However, the standard deviations from the mean measured forces were smaller than 10% in all cases. Hence, the errorbars in Fig. 4-4a,b reflect the 10% accuracy of the load cell. Model predictions for drag and blade posture are also shown in Fig. 4-4. The model force predictions agree with the observations for all but the shortest HDPE blade. For the 5 cm HDPE blade, the horizontal force, F_x, is over-predicted by the model (Fig. 4-4a, black squares and line). This over-prediction may be due to the fact that for flat plates with small length-to-width ratios, pressure recovery near the tip leads to a drag coefficient that is lower than the value assumed here, $C_D = 1.95$.

When the Cauchy number is small, the blades do not reconfigure significantly and the standard quadratic drag law applies. For example, the 5 cm HDPE blade ($Ca \leq 2.5$ for all flow speeds, Table 4.1) remained near-vertical even at the highest velocity tested (Fig. 4-4c), and the measured horizontal forces were approximately proportional to the square of velocity (Fig. 4-4a). Specifically, the horizontal force increased with velocity as $F_x \propto U^A$, with $A = 1.86 \pm 0.05$. As the Cauchy number increases so that $Ca \gg 1$, reconfiguration becomes significant and the quadratic law overestimates drag. As an example, the 25 cm HDPE blade exhibited some reconfiguration over the entire range of velocities tested here ($Ca = 3.9 - 320$, Table 4.1). The blade remained vertical near the clamped base, but blade curvature

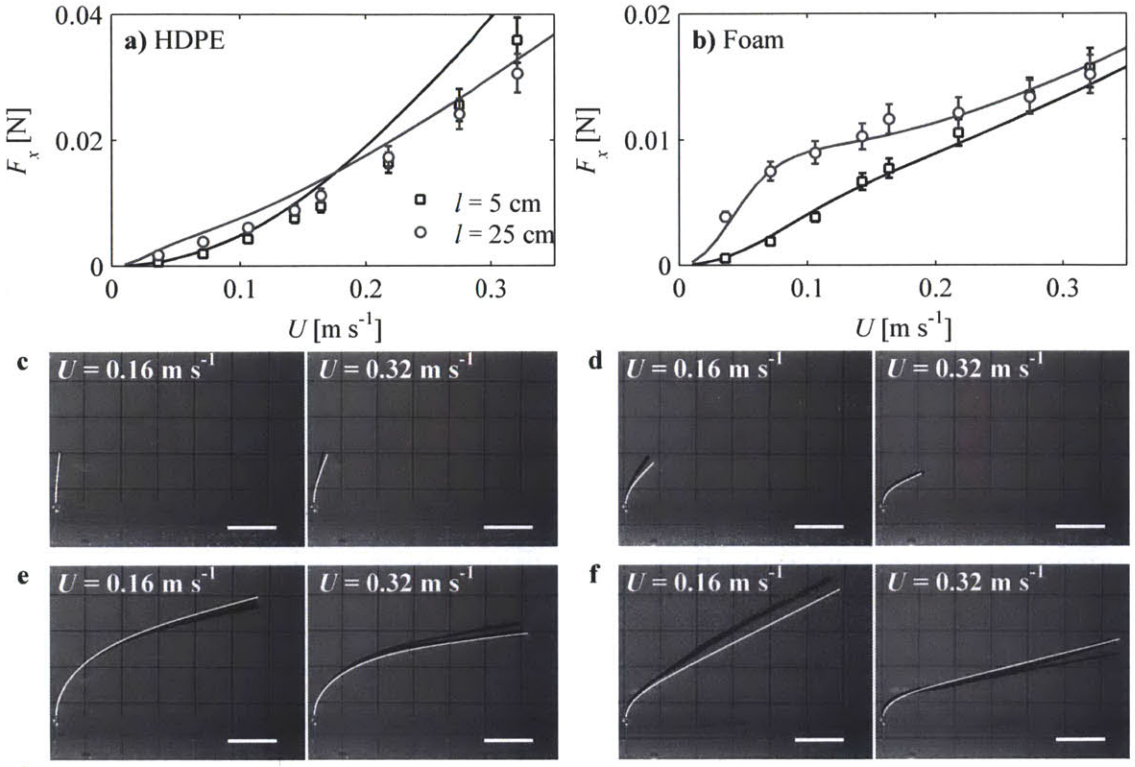

Figure 4-4: (a) Horizontal force (F_x), plotted against velocity (U), for the model blades made from high density polyethylene (HDPE). The black squares and black line correspond to the measured and predicted forces for the 5 cm-long blade. The gray circles and gray line correspond to the measured and predicted forces for the 25 cm-long blade. (b) Same as (a), but for the model blades made from silicone foam. (c-f) Observed blade postures for two different flow speeds. The overlaid white curves are model predictions, and the scale bar is 5 cm. (c, e) correspond to the 5 cm- and 25 cm-long HDPE blades, respectively. (d, f) correspond to the 5 cm- and 25 cm-long foam blades.

increased with increasing velocity (Fig. 4-4e). This flow-induced streamlining led to a near-linear relationship between the measured drag force and velocity (Fig. 4-4a). Specifically, $F_x \propto U^A$ with $A = 1.31 \pm 0.10$, in agreement with the predicted scaling law, $Fx \propto U^{4/3}$. Note that, because of reconfiguration, the drag generated by the 25 cm HDPE blade was comparable to the drag generated by the 5 cm blade for velocities greater than 25 cm s^{-1} (Fig. 4-4a). This is because reconfiguration reduces drag both by reducing frontal area and by producing more streamlined shapes. For $U = 32$ cm s^{-1}, the 25 cm HDPE blade had a larger frontal area than the 5 cm blade (see Fig. 4-4c,e). However, the drag generated by the longer blade was reduced because it was pushed over into a more streamlined posture compared to the upright shorter blade.

For the 25 cm foam blade ($B = 340$, Table 4.1), the reconfiguration response resembled the zero-stiffness limiting case, with a nearly constant θ along most of the blade length. However, curvature is observed at the bed because the blade is clamped, not pinned, as assumed by the model for the zero-stiffness case. Note that the curvature occurs over a much shorter length scale (i.e., smaller radius of curvature) than that observed for the stiffer HDPE blade (see Fig. 4-4e,f). This reinforces the idea that, even for buoyant blades with $B \gg 1$, stiffness plays a role in determining posture near the bed. The observed postures for the foam blades are slightly more upright compared to the model predictions for $U = 16$ cm s^{-1} (Fig. 4-4d, f). This discrepancy may be due to the uncertainty in B caused by variations in the foam density (Table 4.1).

For velocities between 5 cm s^{-1} and 20 cm s^{-1}, the drag generated by the 25 cm foam blades (Fig. 4-4b, gray circles) increased sub-linearly with velocity i.e., $F_x \propto U^A$ with $A = 0.69 \pm 0.22$. This sub-linear relationship between drag and velocity is characteristic of a buoyancy-dominated response, as discussed earlier. For velocities greater than $U \approx 20$ cm s^{-1}, however, the drag-velocity behavior of the 25 cm foam blade converged with that of the 5 cm foam blade, for which $A = 1.54 \pm 0.20$ (Fig. 4-4b, black squares). This exponent suggests a transition to the value 4/3 predicted for stiffness-dominated regimes, which is expected for $B^{-1}Ca > O(1)$. Indeed, for

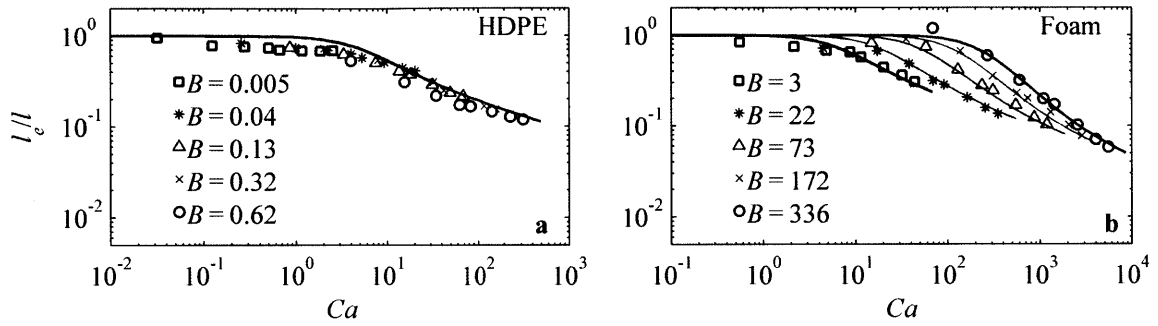

Figure 4-5: (a) Effective blade length (l_e/l), plotted as a function of the Cauchy number (Ca), for the model blades made from HDPE. The markers show experimental observations for the five different blade lengths tested, l = 5 cm (squares), 10 cm (asterisks), 15 cm (triangles), 20 cm (crosses), and 25 cm (circles), and the solid lines represent model predictions. The inset legend shows the value for the buoyancy parameter (B) for each of the five blade lengths. (b) Same as (a), but for the model blades made from foam.

$U > 20$ cm s^{-1}, $B^{-1}Ca > 6$ (Table 4.1). Hence, we see that a single blade can transition between the buoyancy-dominated and stiffness-dominated regimes with increasing velocity. When the drag force scale exceeds blade buoyancy, $B^{-1}Ca > O(1)$, blade stiffness becomes the dominant restoring mechanism, and the predicted scaling law $F_x \propto U^{4/3}$ applies, even if the value of B ($\gg 1$) implies that buoyancy should dominate.

Consistent with the data shown in Fig. 4-4, the model is able to accurately predict the effective blade length, l_e/l, for all eighty test cases (Fig. 4-5). The measured effective lengths were calculated from the measured forces, F_x, using the relation: $(l_e/l) = F_x/(1/2\rho C_D blU^2)$. The effective lengths for all the HDPE blades fall onto a single curve (Fig. 4-5a), which is similar to the zero-buoyancy case shown in Fig. 4-2b. This result suggests that for $B < 1$, blade stiffness is the dominant restoring mechanism and the effect of buoyancy on reconfiguration may be neglected. Further, in agreement with model predictions, the data suggest the following scaling relationships at the stiff and flexible limits: $(l_e/l) \sim Ca^A$, with $A = -0.07 \pm 0.03$ for $Ca < 2$, and $A = -0.41 \pm 0.06$ for $Ca > 10$.

In contrast, the effective lengths for the foam blades of different length follow distinct curves (Fig. 4-5b) that depend on the value of the buoyancy parameter,

confirming the model prediction (Fig. 4-5b, solid lines) that blade buoyancy delays the onset of reconfiguration. However, all five curves seem to collapse together for $B^{-1}Ca > O(1)$ (see Fig. 4-5b, $Ca > 1000$), again indicating that once the hydrodynamic forcing exceeds blade buoyancy, blade stiffness becomes the dominant restoring mechanism. So, blade stiffness may not be neglected even if $B \gg 1$. Recall that even at the highest B, curvature is observed near the bed (Fig. 4-4f), indicating that stiffness must influence posture.

Note that the model predictions described in this section were based on the known blade properties, flow speed and the drag coefficient for flat plates. No empirical fitting parameters were used. Agreement between the experimental observations and the predictions therefore confirms that the model effectively captures the physics underlying the flow-induced reconfiguration of buoyant, flexible blades. Of course, the experiments were designed to fit the simplifying assumptions made to develop the model. For example, the model blades had a constant, rectangular cross-section, and the blade material properties did not vary over the blade length. The flow speed was also constant over the length of the blade. Below, we show that the model developed here is also able to predict drag and posture for real aquatic vegetation in flow, where some of these simplifying assumptions break down.

4.3.2 Natural aquatic vegetation

Abdelrhman [1] photographed *Zostera marina* blades exposed to three different flow speeds, $U = 6$ cm s^{-1}, 12 cm s^{-1}, and 14 cm s^{-1}. The model described here accurately predicts the observed postures (Fig. 4-6). As mentioned above, the geometric and material properties for *Zostera marina* blades vary significantly in natural systems. To arrive at our estimates for blade posture, we assumed that the blade width and thickness were $b = 0.8$ cm and $d = 0.35$ mm, respectively [56]. As before, we assumed that the drag coefficient was identical to that for flat-plates, $C_D = 1.95$. Abdelrhman [1] reported that the blade density was 700 kg m^{-3}, so that $\Delta\rho = 325$ kg m^{-3}, and the blade length was $l \approx 40$ cm. We estimated blade postures for two different values of the elastic modulus, $E = 0.4$ GPa and $E = 2.4$ GPa, corresponding

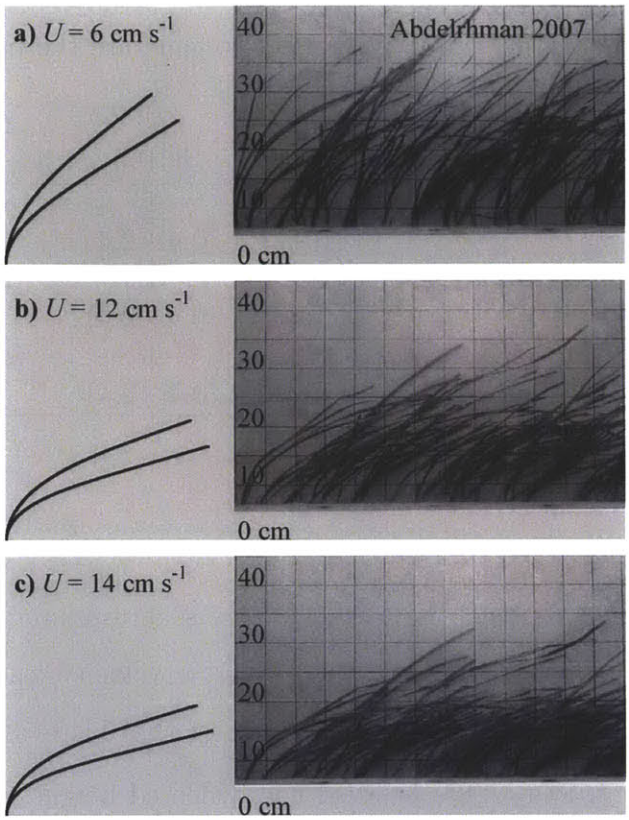

Figure 4-6: Comparison of model predictions for blade posture with the observations made by Abdelrhman [1] for the seagrass *Zostera marina* exposed to a flow of speed $U = 6$ cm s^{-1}. Predicted blade postures are shown as black curves on the left, while the observations are shown on the right (images from fig. 8 in Abdelrhman [1]). Note that the two predicted blade postures correspond to the highest and lowest assumed values for the blade elastic modulus, as described in the text. (b, c) Same as (a) but for flow speeds $U = 12$ cm s^{-1} and $U = 14$ cm s^{-1}, respectively.

to the minimum and maximum values reported by Bradley and Houser [8]. The more upright predicted posture corresponds to the higher elastic modulus, $E = 2.4$ GPa.

Abdelrhman [1] also developed a coupled flow-structure model to predict seagrass posture in flow, which was able to predict the deflected height of the seagrass reasonably well. However, this model assumed that blade stiffness was negligible, and that posture was set by a balance between hydrodynamic forces (drag, lift and skin friction) and buoyancy. Unsurprisingly, the blade posture predictions made by this model resemble the postures shown in Fig. 4-2a for the zero-stiffness case (i.e., pin-joint at the bed and a constant angle θ). Clearly, this is not consistent with the

Table 4.2: Assumed seagrass blade properties to generate the model predictions for comparison to data from Fonseca and Kenworthy [28]

Species	$b^\star$ [cm]	$d^\star$ [mm]	l [cm]	$E^\ddagger$ [GPa]	$\Delta\rho$ [kg m^{-3}]	B
Thalassia testudinum	1	0.45	20* (10-30)	1 (0.4 - 2.4)	85‡	0.4 (0.2 - 3.3)
Halodule wrightii	0.2	0.4	15* (10-20)	1 (0.4 - 2.4)	85‡	0.2 (0.03 - 1.3)
Zostera marina	0.8	0.35	40† (30-50)	1 (0.4 - 2.4)	325†	20 (3.5 - 98)

† From Abdelrhman [1]
‡ From Bradley and Houser [8]
* From Luhar et al. [56]

images shown in Fig. 4-6, which indicate that the seagrasses remain upright close to the bed. The images also show that an increase in velocity leads to an increase in curvature near the bed. These observations suggest that blade stiffness is important.

Fonseca and Kenworthy [28] observed the deflected height, h/l, for three different species of seagrass exposed to flow: *Thalassia testudinum*, *Halodule wrightii*, and *Zostera marina*. Figure 4-7 compares the observations (symbols) with model predictions (lines, Eq. 4.10). Table 4.2 lists the reported blade properties for each species of seagrass that were used here to predict deflected height. The natural variability in seagrass blade properties is reflected in the upper- and lower-bound predictions shown as dashed lines. The upper- and lower-bound predictions correspond to the stiffest (lowest B, Table 4.2) and most flexible (highest B, Table 4.2) cases, respectively.

In general, the observations lie within the limits predicted by the model. However, there are some discrepancies. Figure 4-7a shows that the observed deflected height for *Thalassia testudinum* lies closer to the upper-limit predicted by the model. Also, some outliers appear above the upper-limit. These results indicate that the assumed blade properties underestimate blade stiffness or blade buoyancy for the specific population of *Thalassia testudinum* studied by Fonseca and Kenworthy [28]. For instance, the elastic modulus may have been greater than the assumed value, $E = 2.4$ GPa. Note also that we do not consider any variations in seagrass buoyancy, or blade thickness. Seagrass blade buoyancy can change over time and in response to flow conditions,

and so the assumed density difference between the blades and the water ($\Delta\rho = 85$ kg m^{-3}), could be an underestimate. Similarly, the blade stiffness is proportional to the cube of blade thickness, $I \propto d^3$, and so even a relatively small increase in blade thickness could lead to significantly stiffer blades. Finally, previous studies (see e.g. [27]) suggest that the maximum bending for *Zostera marina* is achieved at a velocity of ~ 50 cm s^{-1}. The predictions shown in Fig. 4-7c are consistent with this observation.

Stewart [89] measured the forces acting on the marine macroalga *Turbinaria ornata* exposed to currents. This macroalga consists of a central stipe, or stem, that is covered with blades and pneumatocysts along part of its length. Stewart noted that populations of this macroalga in sheltered backreef habitats had buoyant pneumatocysts, while populations in wave-exposed forereef habitats lacked pneumatocysts, or that the pneumatocysts were very small and non-buoyant. Instead, algae from the forereef sites had shorter, thicker stipes. To test how these variations in morphology affected drag, Stewart measured the forces acting on algae samples obtained from an exposed forereef site, and a sheltered backreef site, for velocities ranging from $U = 32$ cm s^{-1} to $U = 75$ cm s^{-1}. The force measurements were used to estimate the drag coefficient in the reconfigured state, C_D^*, using the quadratic drag law, $C_D^* = F_x/(1/2\rho A_v U^2)$, where A_v is the planar surface area for the algae in an un-deflected state. Recall from Eq. 4.9 that the effective length is defined as $(l_e/l) = F_x/(1/2\rho C_D A_v U^2)$. We calculated the effective length from the reported values of C_D^* by combining the above relations, leading to $(l_e/l) = C_D^*/C_D$. The data shown in Stewart [89] suggest that the drag coefficient was $C_D \approx 2$ at the limit when the macroalgae remained upright in the water. Hence, we assumed $C_D = 1.95$, as before.

To arrive at model predictions for this morphologically complex macroalga, we calculated the buoyancy parameter as $B = F_B l^2/EI$ (c.f. Eq. 4.7), where F_B is the total buoyancy of each alga, l is the total stipe length, E is the elastic modulus and $I = \pi r^4/4$ is the second moment of area for the stipe of radius r. Similarly, we calculated the Cauchy number based on the relation $Ca = (1/2)\rho C_D A_v U^2 l^2/(EI)$

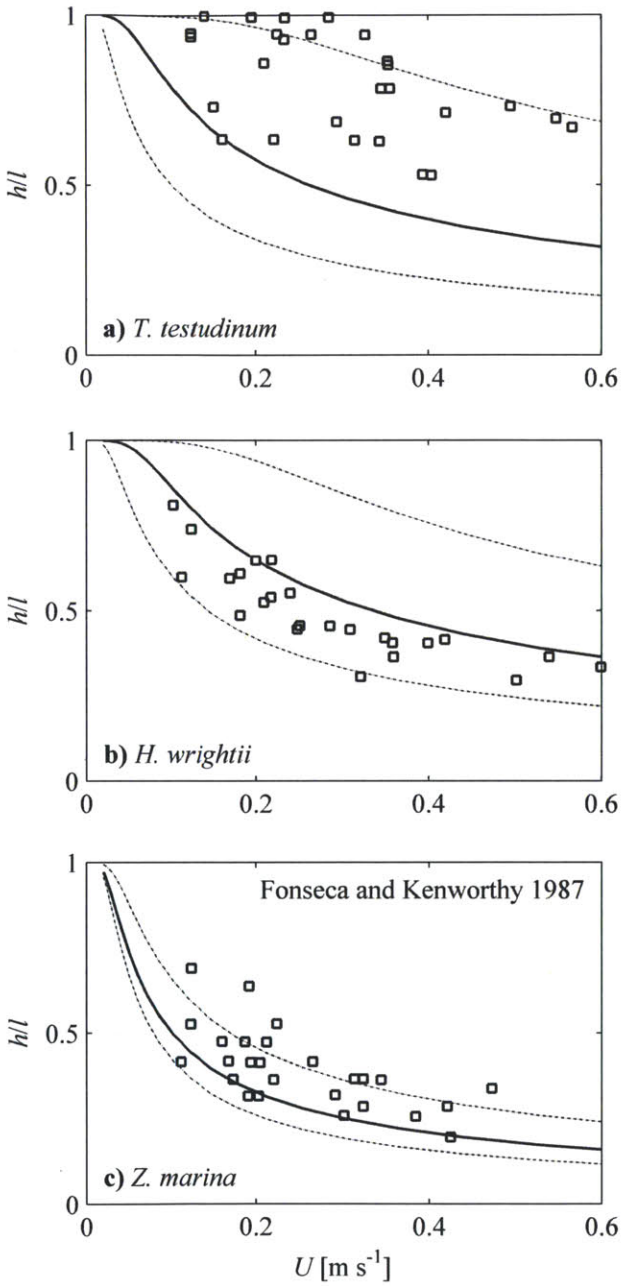

Figure 4-7: (a-c) Deflected blade height (h/l), plotted against velocity (U). Observations made by Fonseca and Kenworthy [28] are shown as squares, while the model predictions are shown as solid and dashed lines. The solid line corresponds to model predictions that use the elastic modulus and blade length that are in the middle of the range reported in previous literature. The dashed lines correspond to predictions made with the upper- and lower-limit of elastic modulus and blade length (Table 4.2). (a) shows the data for the seagrass species *Thalassia testudinum*, while (b, c) show the data for *Halodule wrightii* and *Zostera marina*, respectively.

Table 4.3: Material and geometric properties for the macroalga *Turbinaria ornata*, as reported by Stewart [89]. Also shown are the estimated buoyancy parameter and range of Cauchy number. A negative value of the buoyancy parameter corresponds to the case where the vegetation is denser than the water.

		Backreef	Forereef
E	[MPa]	29	34
l	[cm]	19	9.9
r	[mm]	1.3	1.6
A_v	[cm^2]*	12	7.0
F_B	[mN]	23	-10
B		15	-0.56
Ca	($U = 32 - 75$ cm s^{-1})	76-400	4.0-21

* Indirect estimate based on other reported properties

(c.f. Eq. 4.8). The vegetation parameters used to estimate B and Ca were either reported by Stewart [89], or estimated from values given in that paper. We repeat them in Table 4.3 for convenience. The buoyancy parameters were $B = 15$ and $B = -0.56$ for the backreef and forereef samples, respectively. The negative value for the buoyancy parameter indicates that the forereef algae were denser than water.

Despite the more complex vegetation morphology, agreement between the observed and predicted values for effective length is very good (Fig. 4-8). The shorter, stiffer forereef samples remained more upright over the range of velocities tested, and therefore had higher effective lengths. In contrast, the longer, more flexible backreef samples were pushed over by the flow, leading to lower effective lengths. The flow speeds tested by Stewart were higher than those recorded in the sheltered backreef location but lower than those for the exposed forereef site. The ranges of field conditions reported by Stewart [89] are marked by shaded regions in Fig. 4-8. For conditions characteristic of the backreef site, the hydrodynamic forcing and buoyancy are comparable, $B^{-1}Ca \sim O(1)$, and so the model predicts that the buoyant, backreef algae are likely to remain upright. However, for conditions characteristic of the forereef site, the Cauchy number is large, $Ca > O(10)$, and so the model predicts significant reconfiguration for the forereef algae. Below, we briefly discuss the possible ecological implications of these results.

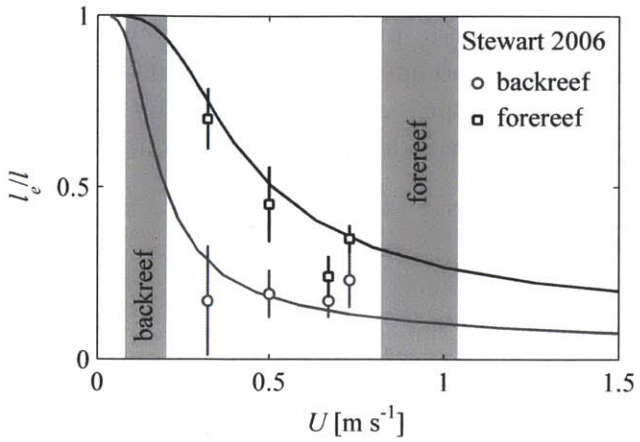

Figure 4-8: Effective blade length (l_e/l) plotted against velocity (U) for the marine macroalga *Turbinaria ornata*. The black squares correspond to the measurements made by Stewart [89] for samples collected from a wave-exposed forereef site, while the gray circles correspond to the measurements for samples collected from a sheltered backreef site. The black and gray lines show model predictions for the forereef and backreef samples, respectively. The shaded areas represent the velocities reported by Stewart for each site.

4.4 Discussion

4.4.1 Phenotypic plasticity in *Turbinaria ornata*

By considering the differences in the reconfiguration response for buoyancy- and stiffness-dominated cases, we can start to address how selective pressures may produce differences in vegetation morphology across different flow environments, such as those observed by Stewart [89]. As described above, Stewart observed that populations of the macroalga *Turbinaria ornata* in sheltered backreef habitats had buoyant pneumatocysts, while populations in exposed forereef habitats lacked pneumatocysts, or had pneumatocysts that were small and non-buoyant. This variation can perhaps be explained based on the limited nature of the restoring force due to buoyancy. Stewart [88] suggests that an upright posture can benefit benthic vegetation both by increasing light availability and by enhancing nutrient and oxygen transfer. If the primary purpose of the buoyant pneumatocysts is to help maintain an upright posture, investment in pneumatocysts would only be worthwhile if the additional buoyancy has a significant effect on posture. This is only possible if the drag force

scale is smaller than the buoyancy force, $B^{-1}Ca \leq O(1)$. The material and geometric properties listed in Table 4.3 suggest that this is unlikely to be the case for these macroalgae at velocities typical of the forereef site ($U \approx 100$ cm s^{-1}, Fig. 4-8). Even if the forereef samples were as buoyant as the backreef samples, so that $F_B = 23$ mN (instead of -10 mN, Table 4.3), the buoyancy parameter would be $B \approx 1.4$ (instead of $B = -0.6$), while the Cauchy number would be $Ca \approx 37$ for $U = 100$ cm s^{-1}, leading to $B^{-1}Ca \gg 1$. As a result, the additional buoyancy afforded by the pneumatocysts would have little effect on posture. In contrast, for velocities typical of the sheltered backreef site ($U \approx 15$ cm s^{-1}, Fig. 4-8), the Cauchy number is $Ca \approx 17$, which is comparable to the value of the buoyancy parameter for the backreef samples, $B = 15$. In this case, since $B^{-1}Ca \sim O(1)$, investment in the pneumatocysts may be worthwhile because buoyancy can help maintain an upright posture.

We must stress that the above discussion is presented primarily as a starting point for further study. A more complete analysis of the ecological trade-offs associated with allocating resources towards pneumatocysts rather than stem or leaf tissue needs to account for many other factors in addition to posture in the water column. A deeper understanding of the energetic costs involved is necessary. The effect of this allocation on photosynthetic performance and susceptibility to breakage must also be considered. Further, *Turbinaria ornata* grows in wave-dominated environments and so any discussion of hydrodynamic performance must take into account wave-induced forces (see e.g. [14, 15, 16]).

4.4.2 Accounting for canopy effects

A number of assumptions were made to yield the governing Eq. 4.6 for blade posture. The assumption of a rectangular beam cross-section is reasonable for seagrasses but the cross-section and material properties can vary along a real blade [8, 30]. In addition, the flow speed is likely to vary along the blade. We can account for spatial variations in vegetation properties (E, I, $\Delta\rho$, b, d, C_D) and velocity (U) by reverting Eq. 4.5 to a more general form:

$$\frac{d}{ds}\left(-EI\frac{d\theta}{ds}\right)\Big|_{s^*} + \int_{s^*}^{l} \Delta\rho g b d \sin\theta^* \, ds = \int_{s^*}^{l} \frac{1}{2}\rho C_D b U^2 \cos^2\theta \cos(\theta - \theta^*) \, ds \qquad (4.14)$$

Eq. 4.14 can then be made dimensionless as before. However, because the blade material properties and flow vary along the blade length, the buoyancy parameter (Eq. 4.7) and Cauchy number (Eq. 4.8) must be defined using characteristic values (e.g., an average) for these quantities.

Depth-uniform flow is a reasonable assumption for individual plants (or very sparse canopies) over smooth beds such that vegetation does not significantly affect the flow, and the height of the bottom boundary layer is small compared to the height of the vegetation. However, the presence of neighboring blades can change the flow structure, which can affect the reconfiguration response. To explore this point, we compare the reconfiguration response for a depth-uniform flow of velocity $U(0 \leq z \leq h) = U_v$ with that for the two representative velocity profiles shown in Fig. 4-9. For sparse vegetation canopies, the velocity profile approaches that of a rough, turbulent boundary layer (see Fig. 2-1a). As an abstraction of this case, we consider a profile where the velocity, $U(z)$, increases linearly from 0 to $2U_v$ over the canopy height, h (sparse canopy, Fig. 4-9). For dense canopies, the velocity profile resembles a shear layer with an inflection point near the top of the canopy (see Fig. 2-1b). As an abstraction of this case, we consider the velocity in the lower half of the canopy to be constant, $U(z < h/2) = 2U_v/3$, and in the upper half of the canopy $(h/2 \leq z \leq h)$ to be linearly increasing from $2U_v/3$ to $2U_v$ (dense canopy, Fig. 4-9). We solve the governing Eq. 4.14 for these velocity profiles using an iterative shooting method for two different values of the buoyancy parameter, $B = 0$ and $B = 100$. For all three velocity profiles, the average velocity over the canopy height is U_v. Hence, we calculate the Cauchy number (Ca) and effective length (l_e/l) using U_v as the velocity scale.

For both values of B, the predicted deflected canopy heights (h/l, Fig. 4-9b) for each of the three velocity profiles are nearly identical for $Ca = 1 - 1000$. The maximum absolute difference in h/l is 0.04 over this range, suggesting that the simple

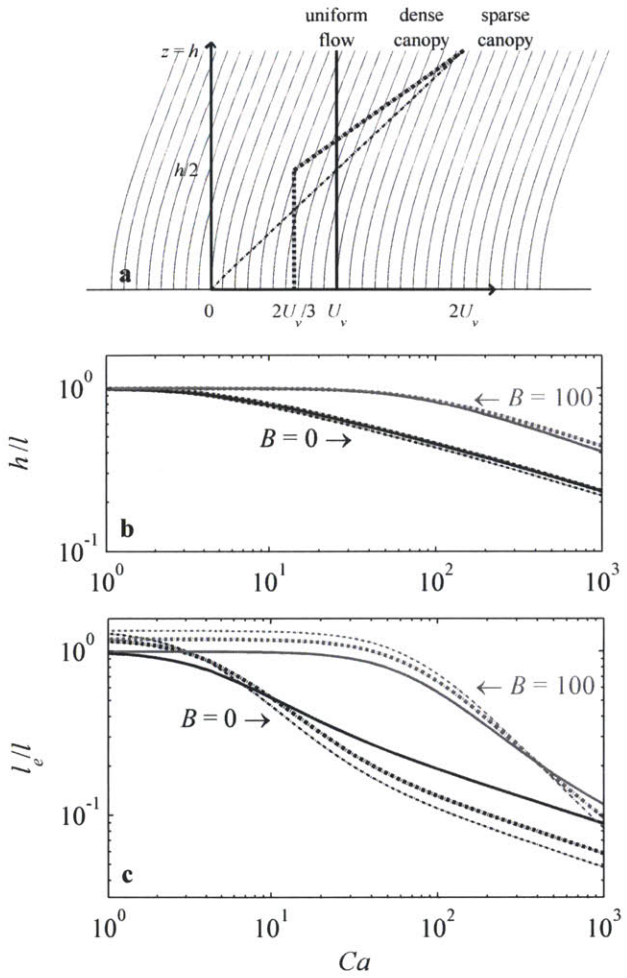

Figure 4-9: Reconfiguration response for three different velocity profiles. (a) Schematic of the three velocity profiles: the depth-uniform case (solid line), the dense canopy case (bold dashed line), and the sparse canopy case (fine dashed line). (b) Deflected canopy height (h/l) plotted against the Cauchy number (Ca) for two values of the buoyancy parameter, $B = 0$ (black lines) and $B = 100$ (gray lines). The solid lines denote the depth-uniform case while the bold and fine dashed lines correspond to the dense and sparse canopy cases. (c) Similar to (b) but showing the effective length (l_e/l) plotted against the Cauchy number (Ca).

depth-uniform model developed here may be used to reasonably predict h/l for field conditions as long as the canopy-averaged velocity is used to calculate Ca. The effective lengths (l_e/l, Fig. 4-9c) for the three velocity cases also show similar trends. However, there are some differences. For $Ca = 1$, the effective lengths are higher for the sparse and dense canopy cases compared to the depth-uniform case. At $Ca = 1$, the plants remain nearly upright and drag is generated along the entire canopy height. Since drag per unit length is proportional to $U(z)^2$ and the canopy-average of $U(z)^2$ is greater than U_v^2 for both the sparse and dense canopy velocity profiles, the effective length is larger. In contrast, for $Ca = 1000$, the depth uniform case has the largest effective length. At $Ca = 1000$, the vegetation is pushed over so far that the drag is generated primarily in the lower part of the canopy. Since $U(z) < U_v$ in the lower part of the canopy for the sparse and dense canopy velocity profiles (Fig. 4-9a), the drag generated for these cases is lower than that for the depth-uniform case.

Since the canopy-averaged velocity, U_v, provides a reasonable description of the reconfiguration response, we now apply the two-layer momentum balance model developed in §2.1.3 to canopies of flexible vegetation, by explicitly accounting for changes in drag and canopy height due to reconfiguration. For flexible vegetation, the momentum balance above the canopy remains as shown in Eq. 2.5, so that the velocity above the canopy is (c.f. Eq. 2.7):

$$U_o = \left(\frac{2gS(H-h)}{C_v} \right)^{1/2} \tag{4.15}$$

However, the vegetation drag term for the canopy momentum balance (Eq. 2.6) must be modified to $(1/2)\rho C_D a l_e U_v^2$ to account for the reduction in drag due to reconfiguration. With this modification, the in-canopy velocity is (c.f. Eq. 2.8):

$$U_v = \left(\frac{2gSH}{C_D a l_e} \right)^{1/2} \tag{4.16}$$

where we assume that the vegetation drag is much larger than the friction at the bed, as before, $C_f \ll C_D a l_e$. Recall that S is the slope, H is the water depth, h is the canopy height, C_v is the canopy friction coefficient and $a = nb$ is the canopy frontal

area per unit volume (n is the density of individual blades per unit bed area). The depth-averaged velocity is:

$$U_T = \frac{U_o(H-h) + U_v h}{H} \tag{4.17}$$

If the geometric (e.g., b,d,l, and $a = nb$) and material (e.g., ρ_v,E) properties of the vegetation are known, the reconfiguration model described in this section can be incorporated into the patch scale momentum balance from §2.1.3 using the following iterative procedure:

1. Assume that vegetation is rigid, i.e., $h = l_e = l$, and calculate the velocity above, U_o, and within, U_v, the patch using Eq. 4.15 and Eq. 4.16, respectively.

2. Use the estimated velocity within the patch, U_v, to calculate the Cauchy number Ca (Eq. 4.8) and the buoyancy parameter B (Eq. 4.7), based on the known vegetation properties.

3. Use the values of Ca and B estimated in step 2 to solve the governing equation for posture (Eq. 4.6) and calculate the effective length, l_e (Eq. 4.9), and the canopy height, h (Eq. 4.10).

4. Use the values of l_e and h estimated in step 3 to calculate new estimates for the overflow velocity, U_o (Eq. 4.15), and the velocity within the patch, U_v (Eq. 4.16).

5. Repeat steps 2-4 until the velocities calculated in step 4, agree with the velocities calculated in the previous iteration within a desired tolerance.

6. Calculate the depth-averaged velocity, U_T, using Eq. 4.17.

We used this iterative procedure to predict canopy heights and depth-averaged velocities for the laboratory experiments with flexible model vegetation performed by Ghisalberti and Nepf [35], who measured velocities for six different cases, denoted F1 F6 (from low to high velocity). Table 4.4 lists geometric and material properties for the model vegetation, along with the water depth, H, measured canopy height, h,

Table 4.4: Geometric and material properties for the model vegetation used by Ghisalberti and Nepf [35]. Hydrodynamic parameters for the six runs (denoted F1 F6) required for the iterative procedure described in 4.4.2 are also listed.

		F1	F2	F3	F4	F5	F6
E	[MPa]			200*			
ρ_v	[kg m^{-3}]			920			
b	[m]			3.8×10^{-3}			
d	[m]			0.2×10^{-3}			
l	[m]			0.215			
H	[m]			0.47			
a	[m^{-1}]			5.2			
$S \times 10^5$	[-]	0.44	1.2	1.9	3.1	3.8	5.5
h	[m]	0.215	0.213	0.2	0.186	0.17	0.155

* Lower than reported value, 300 MPa, but within the range reported by most manufacturers, 200-400 MPa.

and slope, S, for each case. Recall that the reconfiguration model assumes a value of C_D corresponding to rigid, upright vegetation of the same morphology. Ghisalberti and Nepf reported $C_D \approx 1.3$ for run F1, for which the model vegetation remained upright, and so we use this value for the drag coefficient. Finally, we assume that friction coefficient is $C_v = 0.04$, as in §2.1.3.

Fig. 4-10a compares the canopy height, h, predicted by the iterative procedure (circles) with the measurements (crosses). In general, the predicted and measured heights are in good agreement. Fig. 4-10 compares the predicted and measured depth-averaged velocities. For comparison, we also show the velocities predicted by the simple two-layer model assuming that the vegetation remains rigid and upright in flow (Fig. 4-10b, asterisks). The velocities predicted based on the rigid vegetation assumption are significantly lower than the measurements, indicating that the reduction in drag due to reconfiguration can be very important at the patch scale. The model that incorporates reconfiguration does much better (Fig. 4-10b, circles), confirming that the iterative procedure described above is a simple, yet physically reasonable, method to incorporate the effects of vegetation reconfiguration in patch scale models. However, note that the predicted velocities are still slightly lower than the measured velocities even when the iterative procedure is used to account for vegetation reconfiguration. As discussed in Ghisalberti and Nepf [35], this could be because

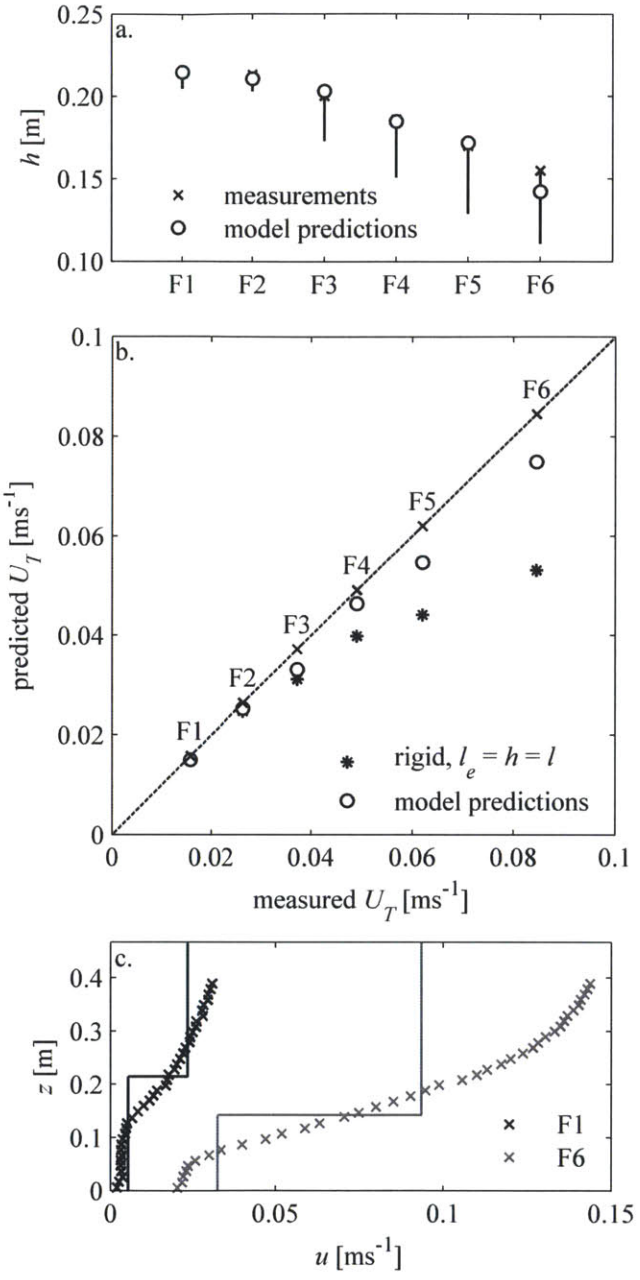

Figure 4-10: Predictions made by iterative two-layer model described in §4.4.2 compared to measurements from Ghisalberti and Nepf [35]. (a) Predicted (circles) and measured (crosses) canopy height, h, for the six runs denoted F1-F6 in [35]. Vertical lines denote measurement uncertainty for F1 and F2, and the vertical excursion due to the passage of a *monami* for F3-F6. (b) Model predictions for average velocity in channel (circles) plotted against measurements. Also shown are the predicted velocities assuming rigid, upright vegetation (asterisks). (c) Measured (crosses) and predicted (lines) velocity profiles.

the momentum exchange between the overflow and patch is less efficient (i.e., lower C_v) when the vegetation is irregular in height and moves in the flow. As a result, we would expect C_v for flexible vegetation to decrease with increasing velocity. Since our model assumes a constant C_v, the mean velocity in the overflow U_o predicted by the iterative scheme (Fig. 4-10c) is lower than the measurements made by Ghisalberti and Nepf.

4.4.3 Other considerations

While seagrass blades have relatively simple, strap-like morphologies, other marine and freshwater macrophytes can have more complex forms. For example, many marine (see e.g., Stewart [89]) and freshwater (e.g., Sand-Jensen [80]) macrophytes consist of a stem covered with leaf-like structures and buoyant, gas-filled pneumatocysts. The *Turbinaria ornata* case study described above shows that the model developed here remains applicable for such macrophytes as long as appropriate changes are made to the buoyancy parameter and Cauchy number. Specifically, the restoring force due to vegetation stiffness should be scaled on the properties of the central structural element - the stem, while the drag force should be scaled on the planar surface area of the vegetation to account for the contribution of the leaves. The buoyancy parameter should be scaled on the net buoyancy force generated by the gas-filled pneumatocysts. Other aquatic macrophytes such as kelp have drag- and buoyancy-generating structures concentrated near the top of the stem. For such cases, the spatial distribution of drag and buoyancy in the governing equation (Eq. 4.14) must be modified.

The model developed here only considers form drag. As the blades assume more streamlined postures, skin friction can become important. To assess when skin friction becomes significant, we consider the limit at which skin friction equals 10% of the horizontal form drag, $F_x = (1/2)\rho C_D b l_e U^2$. The skin friction force on a horizontal beam of length l and width b is $F_f = (1/2)\rho C_f b l U^2$ where C_f is the skin friction coefficient [51]. A comparison of F_f and F_x shows that skin friction becomes important when the effective length is

$$\frac{l_e}{l} \leq \frac{10C_f}{C_D} \tag{4.18}$$

This limit is conservative since it compares form drag in the reconfigured state with skin friction on the entire blade length. As before, the drag coefficient for flat plates normal to flow is $C_D = 1.95$. For horizontal plates with laminar boundary layers, the skin friction coefficient is $C_f = 1.33Re^{-1/2}$, where $Re = Ul/\nu$ is the Reynolds number based on plate length, l [51]. Substituting these expressions for C_D and C_f into Eq. 4.18, we see that skin friction becomes important as the effective blade length decreases below $(l_e/l) < 6.8Re^{-1/2}$. However, this relationship breaks down if the boundary layer on the blades becomes turbulent. The transition to a turbulent boundary layer depends both on flow properties and surface roughness. For smooth surfaces, this transition occurs as the Reynolds number increases above $Re \approx 10^5$ [51]. Using $l = 30$ cm as a typical blade length, the Reynolds number approaches this limit for a flow speed of $U \approx 30$ cm s^{-1}. For a range of flow speeds $U = 3 - 300$ cm s^{-1}, the Reynolds number is $Re = 10^4 - 10^6$, so that the skin friction coefficient for laminar boundary layers is $C_f \approx 0.001 - 0.01$. For turbulent boundary layers, C_f is also expected to be of $O(0.01)$. For $C_f \approx 0.01$, Eq. 4.18 suggests that skin friction is important for $(l_e/l) < 0.05$. However, note that smooth surfaces are rare in the field. Even relatively smooth seagrasses are often covered by epiphytes, which are likely to increase skin friction.

The model and results obtained in this chapter can also inform the debate about the how to best characterize reconfiguration and drag for flexible macrophytes (see [39, 92, 87]). Using the quadratic law, the drag force is usually expressed as $F_x = (1/2)\rho C_D A U^2$. As discussed in Statzner et al. [87], the effects of reconfiguration may be captured by changing either the drag coefficient, C_D, or the characteristic area, A, or by changing both. One option is to use the frontal area of the reconfigured vegetation as the characteristic area scale. However, as discussed above, reconfiguration reduces drag through two mechanisms: reduced frontal area and more streamlined shapes. As a result, using the frontal area would additionally require changing the

drag coefficient to account for the more streamlined shapes. With two changing parameters, comparing results across studies is difficult. Instead, we suggest the use of an effective length, l_e, so that the characteristic area is $A = bl_e$, where b is a characteristic width. This approach allows us to account for the two distinct physical phenomena that can affect drag: Reynolds number effects can be accounted for via the drag coefficient, C_D, and vegetation reconfiguration may be accounted for via the effective length, l_e, which is governed by the Cauchy number, Ca, and buoyancy parameter, B. The drag would then be estimated as $F_x = (1/2)\rho C_D b l_e U^2$, using the drag coefficient, C_D, for a rigid, upright blade.

As it is not practical in all cases to develop a model similar to that described here, as an approximation, we provide the following physically-motivated empirical relationship for effective length:

$$\frac{l_e}{l} = 1 - \frac{1 - 0.9Ca^{-1/3}}{1 + Ca^{-3/2}(8 + B^{3/2})} \tag{4.19}$$

The functional form of Eq. 4.19 was chosen to match model predictions for the zero-stiffness (Fig. 4-2a) and zero-buoyancy (Fig. 4-2b) cases. Eq. 4.19 reduces to $(l_e/l) \approx 1$ when the drag force scale is smaller than either the restoring force due to buoyancy ($B^{-1}Ca \ll 1$) or the restoring force due to stiffness ($Ca \ll 1$). For the zero-stiffness case, Eq. 4.19 yields $(le/l) \sim (B^{-1}Ca)^{-3/2}$ as $B^{-1}Ca \gg 1$. Similarly, for the zero-buoyancy case, Eq. 4.19 simplifies to the predicted scaling $(l_e/l) \sim Ca^{-1/3}$ for $Ca \gg 1$. Figure 4-11 shows that this empirical relationship (dashed lines) follows model predictions (solid lines) extremely well for the general case. The maximum absolute difference between the two predictions for effective length, l_e/l, is 0.03 over the range of parameters shown ($B = 0$ to 100, $Ca = 0.1$ to 10^4).

Finally, the predicted scaling law for effective length, $(l_e/l) \sim Ca^{-1/3}$, can also be interpreted in terms of the Vogel [98] exponent, often reported as a measure of reconfiguration. The Vogel exponent, γ, quantifies deviations from the quadratic drag law by assuming the following relationship between drag and velocity: $F_x \propto U^{2+\gamma}$. The quadratic drag law holds for rigid, upright bodies at high Reynolds number,

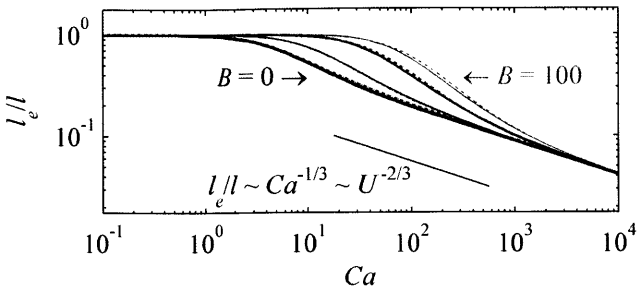

Figure 4-11: Effective blade length (l_e/l) plotted against the Cauchy number (Ca) for a range of values of the buoyancy parameter, $B = 0$ (bold black line), 10 (fine black line), 50 (bold gray line), and 100 (fine gray line). The solid lines denote predictions made by the numerical model, while the dashed lines correspond to the empirical relationship shown in Eq. 4.19.

for which $\gamma \approx 0$. However, because flexible bodies are pushed over by the flow, the drag is reduced, leading to $\gamma < 0$. Using the predicted relationship, $(l_e/l) \sim Ca^{-1/3}$, the drag force is proportional to $U^{4/3}$, which leads to a Vogel exponent of $\gamma = -2/3$. Consistent with this prediction, the observations made by Boller and Carrington [6] indicate that $\gamma \approx -0.6$ for the intertidal macroalga *Chondrus crispus*. For the terrestrial giant reed *Arundo donax*, Harder et al. [41] observed that the Vogel exponent transitions from a value of $\gamma = -0.12$ for velocities smaller than $U = 1.5$ m s^{-1}, to $\gamma = -0.71$ for velocities greater than $U = 1.5$ m s^{-1}. The low-velocity condition is consistent with a quadratic drag law ($\gamma = 0$), implying that these flows do not induce reconfiguration. However, for $U > 1.5$ m s^{-1}, the observed coefficient is consistent with the stiffness dominated reconfiguration ($\gamma = -2/3$). The observations described above suggest that the predicted scaling law for stiffness-dominated reconfiguration, $F_x \propto U^{4/3}$, holds for many systems. Note that for buoyancy-dominated systems ($B \gg 1$), the drag force can increase sub-linearly with velocity (Fig. 4-2b), so that $\gamma < -1$. However, once the drag scale exceeds blade buoyancy, $B^{-1}Ca > O(1)$, the predicted scaling law for effective length, $(l_e/l) \sim Ca^{-1/3}$, applies again and the Vogel exponent reverts to $\gamma = -2/3$.

THIS PAGE INTENTIONALLY LEFT BLANK

Chapter 5

Wave-induced dynamics of flexible model vegetation

This chapter describes the dynamics of flexible blades forced by wave-induced oscillatory flows. In §5.1, we extend the blade reconfiguration model developed in §4.1 to account for time-varying flow and hydrodynamic force. In general, this model adequately reproduces the observed blade motion and measured hydrodynamic forces for laboratory experiments with model blades (§5.2). Interestingly, the experiments show that in some cases, the force generated by flexible blades can be greater than that expected for rigid blades (§5.4.1).

5.1 Dynamic blade model

Similar to §4.1, we develop the dynamic model for elastic, inextensible blades of width b, thickness d, length l, elastic modulus E, and density ρ_v. We assume that the flow field is described by horizontal and vertical time varying velocities, $u_w(t)$ and $w_w(t)$, respectively. The coordinate system used is shown in Fig. 5-1, where s is the distance along the blade from the base, and θ is the local bending angle of the blade relative to the vertical. To describe the force balance for the blade in both the horizontal and vertical directions, we use complex notation, such that the complex velocity is $\tilde{u} = u_w + iw_w$, and $\tilde{x} = x_v(s) + iz_v(s)$ describes the position of a point

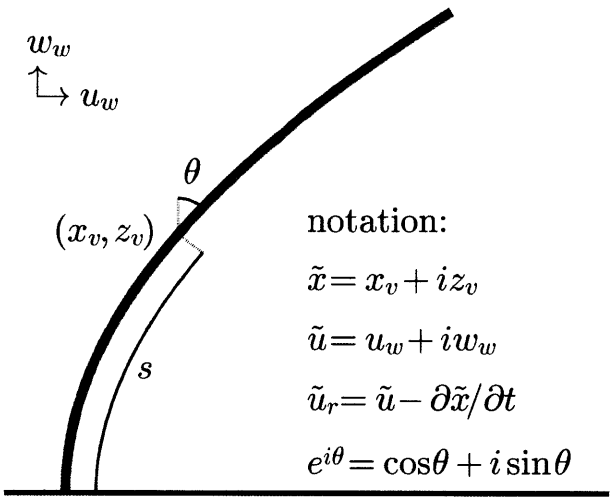

Figure 5-1: Schematic showing the coordinate system, and notation used to for dynamic blade model.

along the blade in the $x-z$ (horizontal-vertical) plane. Using the standard definition $e^{i\theta} = \cos\theta + i\sin\theta$, the inextensibility condition can be expressed as:

$$\tilde{x} = \int_0^s i\exp(-i\theta)\, ds' \tag{5.1}$$

where s' is a dummy variable. As shown in Fig. 5-1, $\tilde{u}_r = \tilde{u} - \partial\tilde{x}/\partial t$, is the *relative* velocity between the blade and the water; t is time.

The dynamics of the flexible beam are controlled by a number of internal and external forces. The internal forces include tension, T, which acts in the blade-parallel direction, and shear, $V = -EI(\partial^2\theta/\partial s^2)$, which acts in the blade-normal direction. As before, I is the second moment of area for the blade cross-section ($I = bd^3/12$ for rectangular cross-sections). We assume that the external forces acting on the blade can be described by the well-known Morison formulation (see e.g. [15]). The external forces per unit blade length include (i) the net buoyancy force,

$$f_B = (\rho - \rho_v)gbd \tag{5.2}$$

which acts in the vertical direction, (ii) the virtual buoyancy force,

$$f_{VB} = \rho b d \frac{\partial \tilde{u}}{\partial t} \tag{5.3}$$

which acts in the direction of flow acceleration, (iii) the drag force,

$$f_D = \frac{1}{2}\rho C_D b \left|\Re\left(\tilde{u}_r e^{i\theta}\right)\right| \Re\left(\tilde{u}_r e^{i\theta}\right) \tag{5.4}$$

which depends on the relative velocity normal to the blade, $\Re(\tilde{u}_r e^{i\theta})$, and acts in the blade-normal direction, and finally (iv) the added mass force,

$$f_{AM} = \frac{\pi}{4}\rho C_M b^2 \Re\left(\frac{\partial \tilde{u}_r}{\partial t} e^{i\theta}\right) \tag{5.5}$$

which depends on the relative acceleration between the flow and the blade, and also acts in the blade-normal direction. As before, ρ is the density of water, C_D is the drag coefficient, and C_M is the added mass coefficient. The notation $\Re$ is used to denote the real component. Following Keulegan and Carpenter [47], we use the cylinder-equivalent blade cross-sectional area, $\pi b^2/4$, to represent the added mass force in this chapter. Recall that in §3, we used the actual blade cross-sectional area, bd. With the cylinder-equivalent cross-sectional area, the added mass coefficient is expected to be $C_M = O(1)$. For the actual cross-sectional area, $C_M = O(b/d)$. We make this notational change primarily for convenience. As discussed below, we hypothesize that flat-plate C_D and C_M may be used to model the behavior of flexible blades in oscillatory flows, as long as the *relative* velocity between the blade and the water is used. Most previous studies that report values of C_D and C_M for rigid, flat plates (e.g. Keulegan and Carpenter [47]) employ the cylinder-equivalent cross-sectional area, $\pi b^2/4$, to model the added mass force; so, we follow the same notation.

A balance of the internal and external forces described above yields the following physically intuitive equation governing blade dynamics:

$$\frac{\partial}{\partial s}\left((V + iT)e^{-i\theta}\right) + i f_B + (f_D + f_{AM})e^{-i\theta} + f_{VB} = \rho_v b d \frac{\partial^2 \tilde{x}}{\partial t^2} \tag{5.6}$$

The term on the right-hand side of Eq. 5.6 represents blade inertia. The real part of

Eq. 5.6 represents the horizontal force balance, and the imaginary part represents the vertical force balance. Note that the blade-normal (V, f_D, f_{AM}) and blade-parallel (T) forces have been multiplied by the factor $e^{-i\theta}$ to rotate them into the $x-z$ directions. Evaluating the first term on the left-hand side of Eq. 5.6, introducing the expression for f_{VB} shown in Eq. 5.3, and multiplying by $e^{i\theta}$, we have:

$$\frac{\partial}{\partial s}(V+iT) - i\frac{\partial \theta}{\partial s}(V+iT) + if_B e^{i\theta} + f_D + f_{AM} + \rho bd\left(\frac{\partial \tilde{u}}{\partial t} - \frac{\rho_v}{\rho}\frac{\partial^2 \tilde{x}}{\partial t^2}\right)e^{i\theta} = 0 \quad (5.7)$$

Multiplication by $e^{i\theta}$ rotates the force balance in Eq. 5.6 such that the real part of Eq. 5.7 represents the blade-normal force balance, and the imaginary part represents the blade-parallel force balance. Similar to §4, the boundary conditions for this dynamic model are: clamped at the base of the blade, $\theta = 0$ at $s = 0$, and free at the tip, $\partial\theta/\partial s = \partial^2\theta/\partial s^2 = T = 0$ at $s = l$.

To make the governing Eq. 5.7 dimensionless, we use the following normalized variables (denoted by over-hats):

$$s = l\hat{s} \;\; ; \;\; t = \hat{t}/\omega \;\; ; \;\; \tilde{u} = U_w\hat{u} \;\; ; \;\; T = (EI/l^2)\hat{T} \;\; ; \;\; \tilde{x} = l\hat{x} \quad (5.8)$$

The blade coordinates s and $\tilde{x}$ have been normalized by the blade length, l. Time has been normalized based on the wave radian frequency, $\omega = 2\pi/T_w$, where T_w is the wave period. Velocity has been normalized using the horizontal oscillatory velocity scale, $U_w = A_w\omega$, where A_w is the horizontal wave excursion. Tension is normalized with the assumed scaling for the internal shear force, EI/l^2 (see also §4.1). Substituting these normalized variables, along with the expressions for V and the external forces (Eq. 5.2-5.5), in Eq. 5.7, and dividing through by EI/l^3, we have the following dimensionless equation describing blade dynamics:

$$\frac{\partial}{\partial \hat{s}}\left(-\frac{\partial^2\theta}{\partial \hat{s}^2} + i\hat{T}\right) - i\frac{\partial\theta}{\partial\hat{s}}\left(-\frac{\partial^2\theta}{\partial\hat{s}^2} + i\hat{T}\right)$$

$$+iBe^{i\theta} + \frac{1}{2}C_D Ca|\Re(\hat{u}_r e^{i\theta})|\Re(\hat{u}_r e^{i\theta})$$

$$+\frac{2\pi^2}{4}C_M\frac{Ca}{KC}\Re\left(\frac{\partial\hat{u}_r}{\partial\hat{t}}e^{i\theta}\right) + 2\pi\frac{CaS}{KC}\left(\frac{\partial\hat{u}}{\partial\hat{t}} - \rho' L\frac{\partial^2\hat{x}}{\partial\hat{t}^2}\right)e^{i\theta} = 0 \qquad (5.9)$$

where

$$\hat{u}_r = \hat{u} - L\left(\partial\hat{x}/\partial\hat{t}\right) \qquad (5.10)$$

is the dimensionless relative velocity between the blade and the water, and

$$L = \frac{l\omega}{U_w} = \frac{l}{A_w} \qquad (5.11)$$

is the ratio of the blade length, l, to the wave excursion, A_w. Similar to the steady-flow reconfiguration model developed in §4, the dimensionless parameters governing blade motion include the Cauchy number, Ca, which is the ratio of hydrodynamic drag and the restoring force due to blade stiffness, and the buoyancy parameter, B, which is the ratio of blade buoyancy to the stiffness restoring force:

$$Ca = \frac{\rho b U_w^2 l^3}{EI} \qquad (5.12)$$

$$B = \frac{(\rho - \rho_v)gbdl^3}{EI} \qquad (5.13)$$

Note that, in contrast to §4, we do not include C_D in the definition of Ca in this chapter. This is because C_D varies with the Keulegan-Carpenter number, $KC = U_w T_w/b$, for wave-induced oscillatory flows (see discussion below). Finally, Eq. 5.9 also includes the ratio of densities, $\rho' = \rho_v/\rho$, and the blade slenderness, $S = d/b$. In dimensionless form, the boundary conditions are: $\theta = 0$ at $\hat{s} = 0$, and $(\partial\theta/\partial\hat{s}) = (\partial^2\theta/\partial\hat{s}^2) = \hat{T} = 0$ at $\hat{s} = 1$. The inextensibility condition (Eq. 5.1) becomes:

$$\hat{x} = \int_0^{\hat{s}} i\exp(-i\theta)\, d\hat{s}' \qquad (5.14)$$

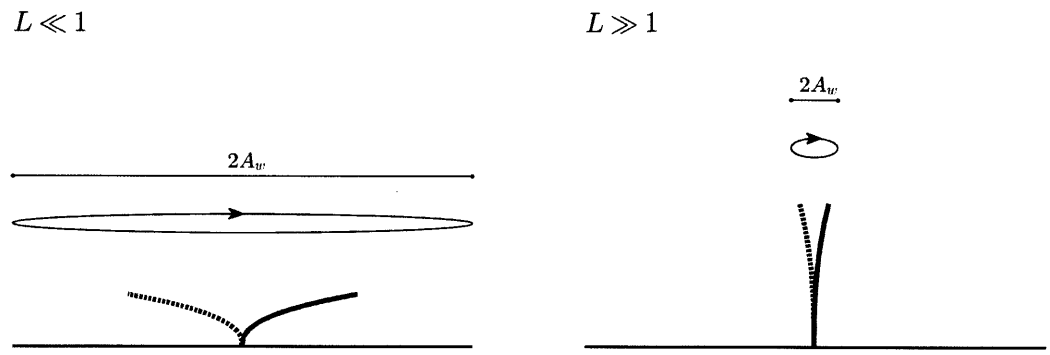

Figure 5-2: Schematic illustrating the difference in blade behavior at the limit of large and small wave excursions, $L \ll 1$ and $L \gg 1$, respectively.

where $\hat{s}'$ is a dummy variable.

Importantly, Eq. 5.10 shows that as the wave excursion becomes much greater than the blade length, $A_w \gg l$ ($L \ll 1$), the relative velocity between the blade and the water is approximately equal to the water velocity, $\hat{u}_r \approx \hat{u}$. Further, for the cases considered here, the blade width is smaller than the blade length, $b/l < 1$. So, at this large excursion limit, the Keulegan-Carpenter number is $KC = U_w T_w/b = 2\pi A_w/b \gg 1$. For $KC \gg 1$, the inertial terms (added mass, virtual buoyancy, blade inertia) in the last row of Eq. 5.9 are negligible. For $\hat{u}_r \approx \hat{u}$ and negligible inertia, Eq. 5.9 resembles the steady-flow reconfiguration model developed in §4. Indeed, for $L = 0$ and $KC \to \infty$, an integration of the real component of Eq. 5.9 yields the governing equation for posture from §4 (Eq. 4.6). Physically, at this large excursion limit, we have a quasi-steady situation where the blade is pushed over by the flow in the early stages of a wave-half cycle (see Fig. 5-2). The blade remains bent until the oscillatory flow reverses direction at the end of the wave half-cycle, with the bent posture reflecting a balance between hydrodynamic drag and the restoring forces due to buoyancy and stiffness.

At the other limit, when the horizontal wave excursion is much smaller than the blade length, $A_w \ll l$ ($L \gg 1$), we anticipate that the blade remains nearly vertical throughout the wave cycle (see Fig. 5-2), and that the horizontal blade excursion scales with the wave excursion, i.e., $|x_v| \sim O(A_w)$. More formally, we expect that

$\theta \sim O(L^{-1}) \ll 1$ and so the inextensibility condition (Eq. 5.14) becomes:

$$\hat{x} = \int_0^{\hat{s}} i \exp(-i\theta)\, d\hat{s}' \approx \int_0^{\hat{s}} i(1 - i\theta)\, d\hat{s}' = i\hat{s} + \int_0^{\hat{s}} \theta\, d\hat{s}' \tag{5.15}$$

In dimensional terms, this leads to $z_v(s) \approx s$ (i.e., nearly-vertical blade) and $(\partial x_v/\partial s) \approx \theta$ (i.e., $|x_v| \sim \theta l \sim A_w$). The implications of this scaling for the hydrodynamic forces generated by flexible blades are discussed in §5.4.

Note that this dynamic blade model requires an accurate description of C_D and C_M. In §4, we showed that the flat plate drag coefficient for steady flows, $C_D = 1.95$, can be used to accurately capture the drag generated by flexible blades, as long as the blade-normal velocity is used in the quadratic law. So, we hypothesize that the flat plate C_D and C_M may also be used for flexible blades in oscillatory flows, as long as the blade-normal *relative* velocity and acceleration are used to characterize the drag and added mass forces. Flat-plate C_D and C_M from [47, 82] are plotted in Fig. 5-3. Both data sets show that C_D and C_M depend on the Keulegan-Carpenter number, KC. Following Graham [37], we model the relationship between the drag coefficient and Keulegan-Carpenter number as $C_D = 10KC^{-1/3}$ (solid line in Fig. 5-3a). However, as $KC \to \infty$ (i.e., $T_w \to \infty$), the drag coefficient must approach the steady flow value, $C_D = 1.95$. Therefore, a more complete definition is $C_D = \max(10KC^{-1/3}, 1.95)$. Unlike the monotonically decreasing relationship between C_D and KC, the variation of C_M with KC is more complex. In general, C_M increases gradually with KC, but there is a pronounced dip in C_M at $KC \approx 18$. This dip corresponds to the case where a single eddy is shed from the plate during each wave half-cycle [47]. We use the spline shown as a solid-line in Fig. 5-3b to describe the variation in C_M with K_C.

To predict blade motion and drag, we solve the governing Eq. 5.9 numerically using finite differences. The blade-normal force balance (real component of Eq. 5.9) is solved explicitly to yield $\theta(\hat{s})$; although, the third-order spatial derivative is treated implicitly for stability. The blade-parallel force balance (imaginary component of Eq. 5.9) is solved implicitly to yield the tension, $\hat{T}(\hat{s})$. To force the dynamic blade model, we use wave-induced velocity fields measured in the laboratory (see §5.2). A

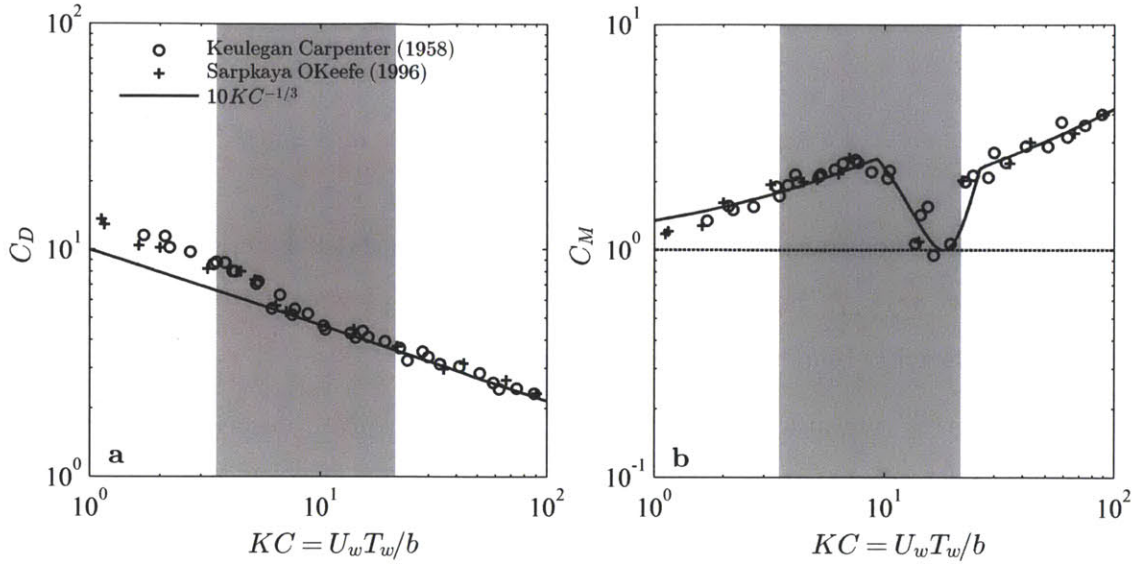

Figure 5-3: Drag and added mass coefficients, C_D (a) and C_M (b), for rigid flat plates in oscillatory flows plotted against the Keulegan-Carpenter number, KC. The data shown are from [47, 82]. The shaded regions represent the range of KC for the laboratory experiments described in §5.2.

description of the numerical scheme, and a code listing, can be found in Appendix C.

5.2 Laboratory experiments

We pursued laboratory experiments that simultaneously (i) measured the hydrodynamic force generated by flexible blades over a wave-cycle, (ii) imaged blade motion, and (iii) measured the local velocity field using particle image velocimetry (PIV). The experiments were carried out in a 24 m-long, 38 cm-wide, 60 cm-deep wave flume fitted with a paddle wavemaker. The paddle was actuated using a programmable signal generator (see §3.2 and Appendix A for details). As before, we tested model blades made of two different materials: silicon foam (E = 500 kPa; ρ_v = 670 kg m^{-3}; d = 1.9 mm) and high-density polyethylene (HDPE, E = 0.93 GPa; ρ_v = 950 kg m^{-3}; d = 0.4 mm). We tested model blades of four different lengths ranging from l = 5 cm to l = 20 cm in 5 cm increments. The blade width was b = 2.0 cm in all cases. The model blades made of HDPE exhibited a small degree of curvature in the cross section. Because of this curvature, the HDPE blades had a second moment

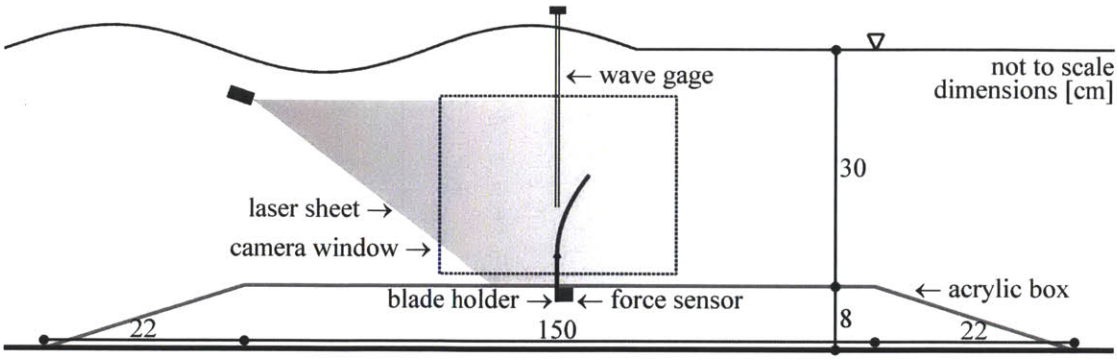

Figure 5-4: Schematic showing the experimental setup. The laser light sheet was placed 0.5 mm behind the model blades. The wave gage was placed 15 cm behind the blades. The direction of wave propagation was from left to right. Not to scale.

of area, $I \approx bd^3/6$. So, the HDPE blades were twice as stiff as they would have been if the cross-section had been perfectly flat and rectangular ($I = bd^3/12$). The estimated buoyancy parameter ranged from $B = 0.002$ to $B = 0.15$ for the HDPE blades, and from $B = 2.7$ to $B = 170$ for the silicon foam blades (Table 5.1). Each model blade was tested in eight different wave conditions: waves of frequency $f = 0.5$ Hz ($T_w = 2.0$ s) with amplitudes $a_w \approx 1, 2, 3, 4$ cm; waves of frequency $f = 0.7$ Hz ($T_w = 1.4$ s) with amplitudes $a_w \approx 2, 4$ cm; waves of frequency $f = 0.9$ Hz ($T_w = 1.1$ s) with amplitudes $a_w \approx 2, 4$ cm. A list of all the test cases is shown in Table 5.1.

To measure the total horizontal force generated by the blade, F_x, we used a submersible s-beam load sensor (Futek LSB210). The measurements were logged to a computer using a bridge completion and data acquisition module (National Instruments NI-USB9237). To study how F_x varies over a wave cycle, the local wave elevation, η, was measured synchronously with F_x using a wave gage of 0.2 mm accuracy. The analog output from the wave gage was amplified and logged to a computer using an analog-digital converter (National Instruments NI-USB6210). We measured F_x and η for a period of 3 min at a sampling rate of 2000 Hz. Thus, we captured between 90 and 162 waves, depending on wave frequency. The measurements were then phase-averaged (see §3.2), to yield representative descriptions of F_x and η over a single wave cycle. As shown in Fig. 5-4, the load cell was mounted inside a trapezoidal box of height 8 cm and total length 192 cm. The model blade was attached to the

Table 5.1: List of test cases for the dynamic blade experiments.

	a_w [cm]*		1	2	3	4	2	4	2	4
		($\pm$0.1 cm)	(0.9)	(1.9)	(2.9)	(3.9)	(1.7)	(3.5)	(1.7)	(3.6)
	T_w [s]	($\pm$0.1 s)	2	2	2	2	1.4	1.4	1.1	1.1
	U_w [cm s^{-1}]	($\pm$0.9 cm s^{-1})	5.0	10.1	15.4	20.6	8.9	16.7	6.6	12.8
	KC		5.0	10.1	15.4	20.6	6.4	11.9	3.7	7.1
	l [cm]	B	Ca							
HDPE										
$E = 0.93 \pm 0.08$ GPa	5	0.002	0.02	0.12	0.28	0.50	0.09	0.36	0.06	0.20
$\Delta\rho = 50 \pm 10$ kg m^{-3}	10	0.02	0.24	1.0	2.5	4.0	0.76	2.8	0.41	1.5
$b = 2.0 \pm 0.05$ cm	15	0.06	0.81	3.2	7.2	13	2.7	9.7	1.5	5.7
$d = 0.4 \pm 0.04$ mm	20	0.15	2.2	7.5	19	36	6.2	21	3.5	13
Silicon foam										
$E = 500 \pm 60$ kPa	5	2.7	1.0	4.4	9.9	17	3.5	12	1.7	6.8
$\Delta\rho = 330 \pm 50$	10	22	8.9	36	90	160	27	95	15	52
$b = 2.0 \pm 0.05$ cm	15	73	33	120	280	530	100	310	53	210
$d = 1.9 \pm 0.10$ mm	20	170	71	300	680	1200	240	800	110	470

* In the text, we refer to each wave condition using these values for the amplitude a_w. Measured a_w are shown in parentheses below.

load cell via a stainless steel blade holder that protruded through a 1.25 cm-diameter hole in the trapezoidal box. The blade holder placed the base of the blade 4 cm above the box surface. The total water depth was 38 cm. Note that the model blade was mounted in the middle of the flume, while the wave gage was mounted approximately 15 cm behind the blade at the same x-location (i.e., the wave gage was 4 cm from the flume sidewall).

For the blade motion and PIV measurements, illumination was provided by a laser light sheet. The light sheet was placed in the $x - z$ plane, 0.5 mm behind the model blade (see Fig. 5-4). Images were captured at 60 frames per second (fps) using a monochrome CCD camera (Dalsa Falcon 1.4M100HG) of resolution 1400 pixels $\times$ 1024 pixels. The field of view was approximately 42 cm $\times$ 31 cm, leading to a spatial resolution of 0.03 cm pixel^{-1}. For each case tested, we captured images over 3 wave cycles, e.g., for waves of period $T_w = 2$ s, we captured 6 s worth of images. For the PIV measurements, the water was seeded with Pliolite particles (density 1020 kg m^{-3}). PIVlab, a MATLAB software package, was used to calculate the horizontal, u_w, and vertical, w_w, velocity fields from the images. The PIV software calculated velocities for blocks of 16 pixels $\times$ 16 pixels (i.e., 0.5 cm $\times$ 0.5 cm). Assuming that the PIV algorithm calculates velocities accurate to 1 pixel per frame, we anticipate a velocity resolution of ± 0.9 cm s^{-1}.

To characterize the wave-induced flow field, we used the velocities measured approximately 15 cm upstream of the model blade. These upstream measurements were used because the measured velocities were relatively smooth sinusoids. Velocities measured closer to the blade were less smooth because of the turbulence generated by the blade itself. Further, the presence of the blade, blade holder, and wave gage in the field of view led to noisier PIV estimates because, unlike the Pliolite seeding particles, these elements do not track the local flow field. To estimate the local magnitudes, U_w and W_w, of the wave-induced oscillatory velocities, $u_w(t)$ and $w_w(t)$, we fitted sinusoids to the velocity measurements (Fig. 5-5). The dimensionless parameters, Ca, KC, and L, were estimated using the maximum fitted horizontal velocity, U_w (Table 5.1), for a vertical location corresponding to the base of the blade (i.e., at

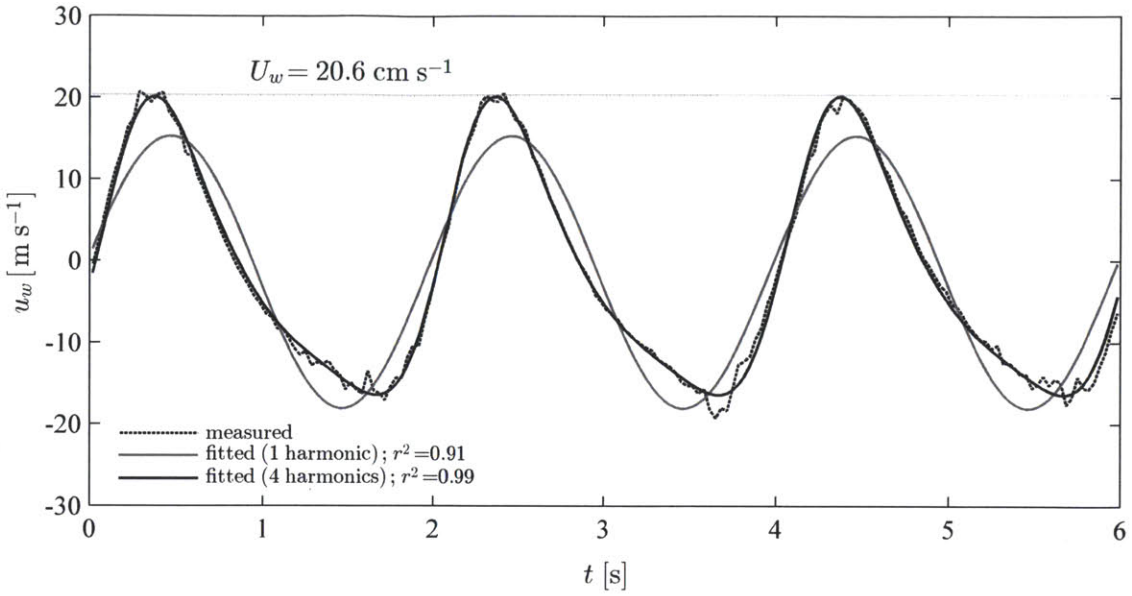

Figure 5-5: PIV-measured horizontal wave velocity, u_w (dashed black line), for waves of period $T_w = 2.0$ s and amplitude $a_w \approx 4$ cm. Also shown is the fitted sinusoidal velocity employing only one harmonic (solid gray line), as well as the fitted velocity employing the first four harmonics (solid black line).

$z_v \approx 0$). For the wave conditions tested here, the Keulegan-Carpenter number was $KC = 3.7 - 20.6$. The Cauchy number was $Ca = 0.02 - 36$ for the HDPE blades, and $Ca = 1.0 - 1200$ for the foam blades (see Table 5.1). The ratio of blade length to wave excursion, $L = l/A_w$, was smallest for the 5 cm-long blades in waves of period $T_w = 2.0$ s and amplitude $a_w \approx 4$ cm, with $L = 0.8$. L was largest for the 20 cm-long blades in waves of period $T_w = 1.1$ s and amplitude $a_w \approx 2$ cm, with $L = 17$. To force the numerical model described in §5.1, we used sinusoidal fits to velocities measured 15 cm upstream of the model blade. For all the wave conditions, we found that the first four harmonics adequately captured the temporal variation in velocity. The use of higher harmonics did not significantly improve the fits as any further differences between the measured and fitted velocities stemmed from high-frequency turbulent fluctuations or noise (Fig. 5-5).

We carried out numerical simulations (Eq. 5.9) corresponding to each of the sixty four cases tested in the laboratory (Table 5.1). For the simulations, we used the known blade material and geometric properties, the PIV-measured velocity fields,

and C_D and C_M as described in Fig. 5-3. The numerical simulations were run until a quasi-steady state was achieved i.e., once blade motion did not vary from one wave cycle to the next. Typically, this quasi-steady state was achieved within 7 or 8 wave cycles. Below, we compare numerical predictions with laboratory experiments. The experiments measured the total horizontal force generated by the model blades, F_x. A force balance for the entire blade shows that F_x is equal to the blade-normal internal shear force, $V = -EI(\partial^2\theta/\partial s^2)$, at the base of the blade ($s = 0$). So, we use $-EI(\partial^2\theta/\partial s^2)|_{s=0}$ to calculate the numerically-predicted, time varying F_x.

5.3 Results

Figure 5-6 (panels a-l) shows that even for the highest velocity (U_w) waves tested here ($T_w = 2.0$ s and $a_w \approx 4$ cm, Table 5.1) the 5 cm-long HDPE blades did not move significantly in flow. These observations are reproduced by the numerical model. The Cauchy number was $Ca \leq 0.5$ for the 5 cm-long HDPE blades. At this limit where $Ca < 1$, the hydrodynamic forcing is not strong enough to overcome blade stiffness; in effect, the blade is rigid. Importantly, the predicted and measured horizontal force, F_x, also show good agreement throughout the wave cycle (Fig. 5-6m). This confirms that the Morison force formulation, with values of C_D and C_M based on previous literature, provides a good description of the forces generated by the model blades in oscillatory flows. There is an ≈ 0.03 N, discrepancy between the measurements and predictions near $t \approx 0.5$ s. However, such discrepancies are not unexpected given that the Morison force formulation is simply a physically intuitive approximation representing the true time-varying hydrodynamic forces generated by the model blade. Even for rigid flat plates, the best-fit values of C_D and C_M shown in Fig. 5-3 lead to some differences between measured and predicted forces [47].

For the same wave condition, the 20 cm-long HDPE blade moved much more with the wave-induced flow (Fig. 5-8, panels a-l) compared to the 5 cm-long blade. For example, the total horizontal excursion at the blade tip was $[\max(x_v) - \min(x_v)] \approx$ 17.5 cm for the 20 cm-long blade, while the tip of the 5 cm-long blade moved back

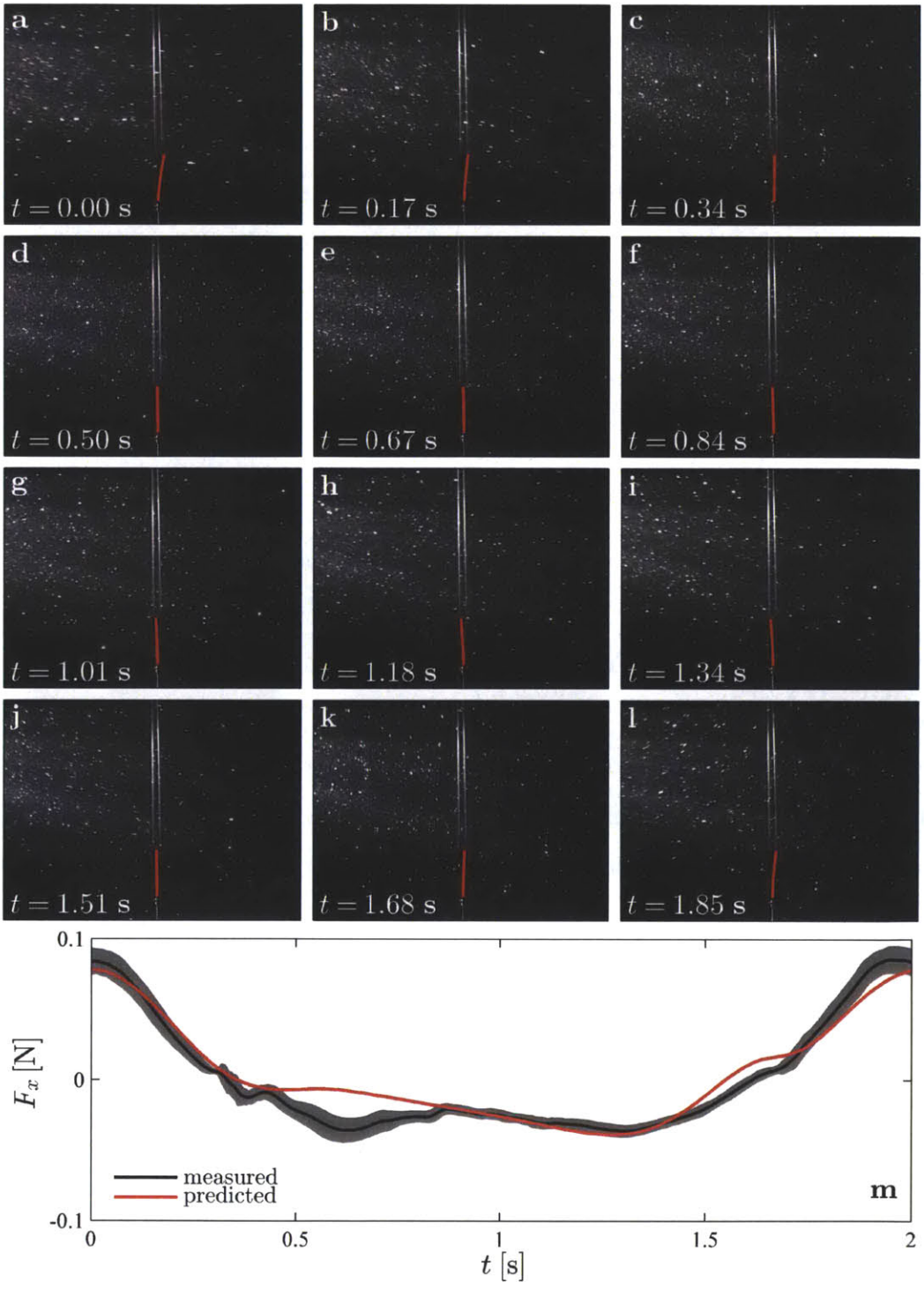

Figure 5-6: 5 cm-long HDPE blade in waves of period $T_w = 2.0$ s and amplitude $a_w \approx 4$ cm. (a-l) Observed and predicted (red) blade posture over the wave-cycle. Note that the real blade (black) is hidden by the model overlay (red) for most of the wave cycle. (m) Measured (black) and predicted (red) horizontal force, F_x, generated by blade. The shaded region represents estimated uncertainty.

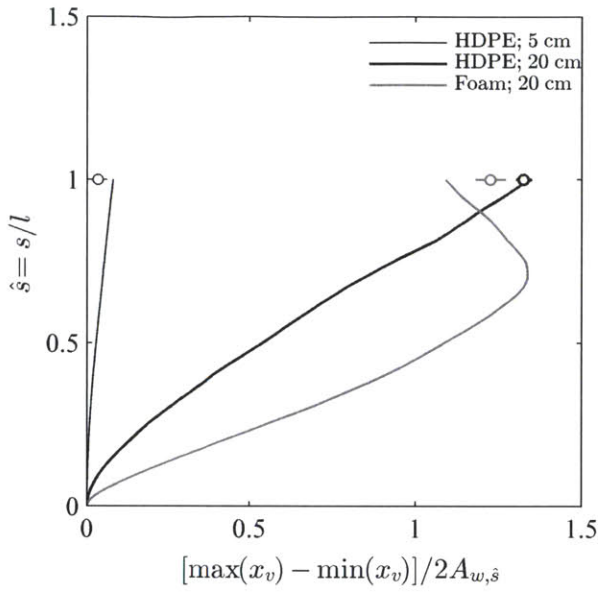

Figure 5-7: Profiles of the total horizontal blade excursion over a wave cycle, $[\max(x_v) - \min(x_v)]$, normalized by the *local* wave excursion, $2A_{w,\hat{s}}$, along the blade length, $\hat{s} = s/l$. Note that $A_{w,\hat{s}}$ was calculated using the measured velocity at the mean vertical position of blade location $\hat{s}$ (i.e., $z_v(\hat{s})$) over a wave cycle. Solid lines denote outputs from numerical simulations. Symbols denote blade tip excursions extracted from the laboratory experiments. All data correspond to waves of amplitude $a_w \approx 4$ cm and period $T_w = 2.0$ s.

and forth by ≈ 0.5 cm. The total wave excursion for these cases ($a_w \approx 4$ cm and $T_w = 2.0$ s) was $2A_w \approx 13$ cm. So, the tip of the 20 cm-long HDPE blade moved through a distance roughly 1.3 times the wave excursion, while the tip excursion for the 5 cm-long HDPE blade was less than 10% of the wave excursion (i.e., the blade remained almost still). These observations are supported by Fig. 5-7, which shows the variation in the horizontal blade excursion (normalized by the local wave excursion) along the length of the blade, as predicted by the numerical model, for both of these cases. The predicted excursion for the 5 cm-long HDPE blade was less than 10% of the wave excursion along the entire blade length (fine black line in Fig. 5-7), while the excursion for the 20 cm-long HDPE blade was comparable to the wave excursion for the upper part of the blade. Specifically, the blade excursion was within 35% of the wave excursion for $\hat{s} > 0.58$ (i.e., for the upper $\approx 40\%$ of the blade).

Passive motion for the upper part of the 20 cm-long HDPE blade is also reflected

in the measured force. The maximum measured force for the 20 cm-long blade was 0.12 N (Fig. 5-8m), while the maximum measured force for the 5 cm-long blade was 0.09 N (Fig. 5-6m). If the 20 cm-long blade had remained still and upright in the water like the 5 cm-long blade, we would have expected the maximum horizontal force generated to be $4 \times 0.09N \approx 0.36$ N. The Cauchy number was $Ca = 36$ for this case. At this limit where $Ca \gg 1$, the hydrodynamic forcing is large enough to overcome blade stiffness, and so the upper portion of the blade moves passively with the flow. Hydrodynamic forces are generated primarily near the base of the blade which remains still relative to the flow. As explained in §4, this reduction in force can be characterized by the use of an effective rigid blade length, l_e, which decreases with increasing Ca. We define l_e for wave-conditions in §5.4 below; we also discuss in greater detail the variation in l_e with the dimensionless parameters governing blade motion: Ca, B, and L.

The blade postures and forces predicted by the numerical model show good agreement with the observations for the 20 cm-long HDPE blade, especially under the wave crest (see e.g., $t < 0.5$ in Fig. 5-8). For example, the predicted blade tip excursion is 17.8 cm (c.f. the observed 17.5 cm, see bold black line and circle in Fig. 5-7), and the maximum predicted force is 0.10 N (c.f. the measured 0.12 N). However, there are some discrepancies between the measurements and the predictions under the wave trough, $t \approx 1.5$ s in Fig. 5-8. The predicted blade posture is more upright compared to the measurements, and the magnitude of the predicted force is lower (a difference of $\approx$0.04 N). Possible reasons for this discrepancy are discussed in §5.4.

In waves of period $T_w = 2.0$ s and amplitude $a_w \approx 4$ cm, the Cauchy number for the 20 cm-long foam blade was $Ca = 1200$. As a result, a larger portion of the foam blade (Fig. 5-9, panels a-l) moved passively with the flow compared to the HDPE blade (see also Fig. 5-7, bold gray line). Recall that, for the 20 cm-long HDPE blade, the numerically-predicted blade excursion was within 35% of the wave excursion along the upper $\approx$ 40% of the blade. For the 20 cm-long foam blade, the excursion was within 35% of the wave excursion for $\hat{s} > 0.29$ (i.e., along the upper $\approx$ 70% of the blade, bold gray line in Fig. 5-7). Force measurements (Fig. 5-9m) confirm that a

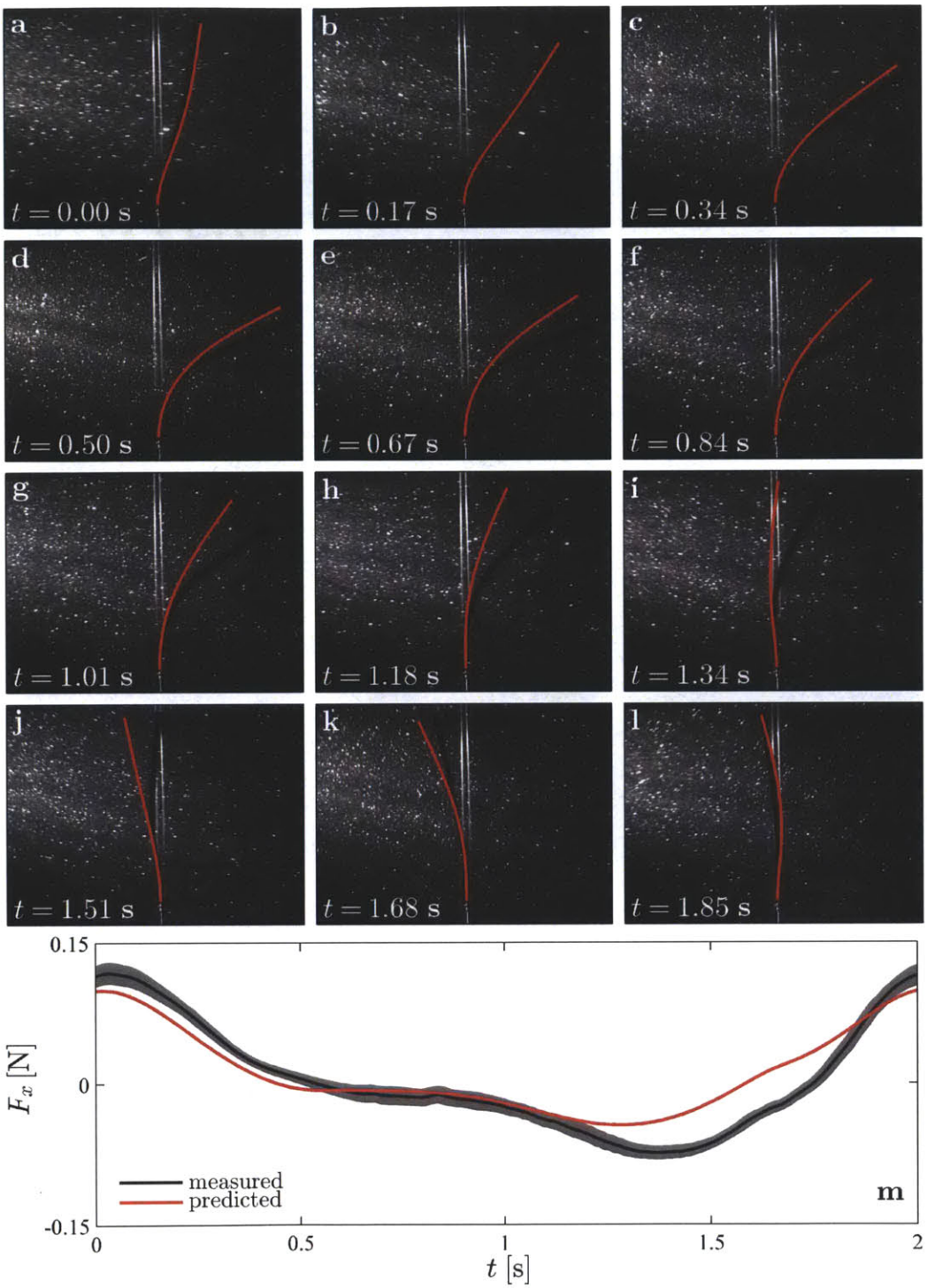

Figure 5-8: 20 cm-long HDPE blade in waves of period $T_w = 2.0$ s and amplitude $a_w \approx 4$ cm. (a-l) Observed and predicted (red) blade posture over the wave-cycle. (m) Measured (black) and predicted (red) horizontal force, F_x, generated by blade. The shaded region represents estimated uncertainty.

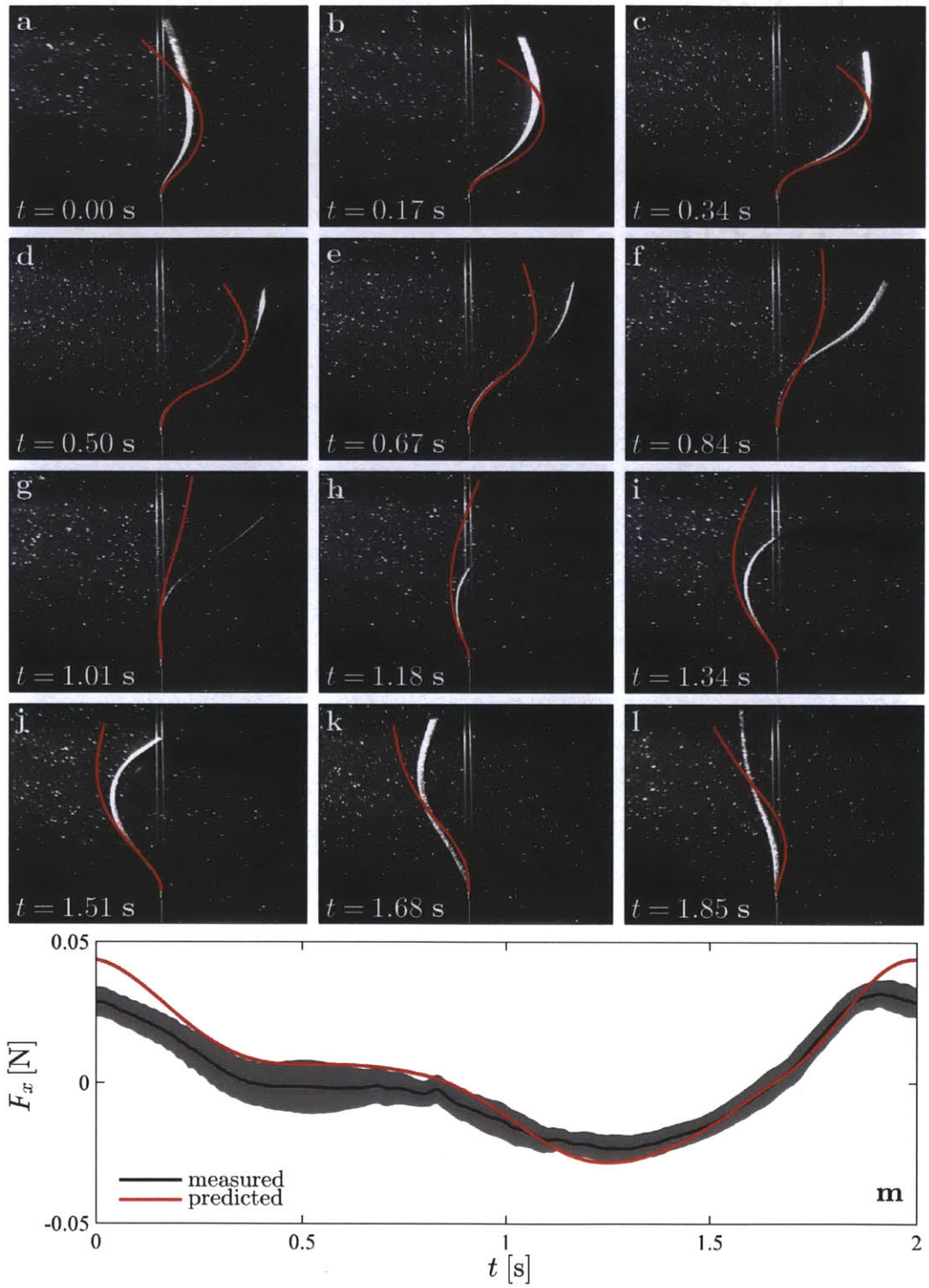

Figure 5-9: 20 cm-long foam blade in waves of period $T_w = 2.0$ s and amplitude $a_w \approx 4$ cm. (a-l) Observed and predicted (red) blade posture over the wave-cycle. (m) Measured (black) and predicted (red) horizontal force, F_x, generated by blade. The shaded region represents estimated uncertainty.

larger portion of the foam blade moves passively in the flow. The maximum measured force was much lower for the foam blade, 0.03N, compared to the HDPE blade, 0.12N.

Note that, for the foam blade, the model predicts blade motion that is more symmetric than the observations. The simulated blade moved back and forth roughly symmetrically about the vertical, while the real blade leaned to the right near the tip (Fig. 5-9d,j). However, the predicted and observed blade excursions are similar over most of the blade. Because the simulated and real blade move through the same distance over a wave cycle, they experience the same relative velocity. Since the hydrodynamic force generated by the blade depends on this relative velocity, the predicted (red) and measured (black) forces agree, within uncertainty, through most of the wave cycle (Fig. 5-9m). Fig. 5-7 shows that the measured blade excursion at the tip (gray circle, $[\max(x_v)-\min(x_v)]/2A_{w,\hat{s}} = 1.23\pm0.06$) was slightly greater than that predicted by the numerical model (bold gray line, $[\max(x_v)-\min(x_v)]/2A_{w,\hat{s}} = 1.09$). We believe this discrepancy arises because we do not account for any pressure recovery at the blade tip in the numerical model, and so the simulated blade experiences greater drag at the tip compared to the real blade.

The three cases described above suggest that the numerical model developed in §5.1, although not perfect, adequately describes the dynamics of flexible blades over the range of conditions tested in the laboratory. This is further confirmed by Fig. 5-10, which compares the measured and predicted root-mean-square (RMS) force over a wave cycle, $F_{x,R}$, for all the laboratory experiments. In general, the model under-predicts the forces acting on the HDPE blades, and over-predicts forces for the foam blades. Specifically, for the foam blades, the ratio of predicted to measured $F_{x,R}$ was 1.27 ± 0.30 (mean $\pm$ s.d.). For the HDPE blades, the ratio was 0.78 ± 0.19. Given the 10% accuracy of the load cell, the measurements agree with the predictions within uncertainty. Uncertainty in material properties offers another possible explanation for these discrepancies. This is especially true for the foam blades, where the uncertainty in both the density difference, $\Delta\rho$, and the elastic modulus, E, was greater than 10% (Table 5.1).

Upon closer inspection, Fig. 5-10a suggests that while the measured and predicted

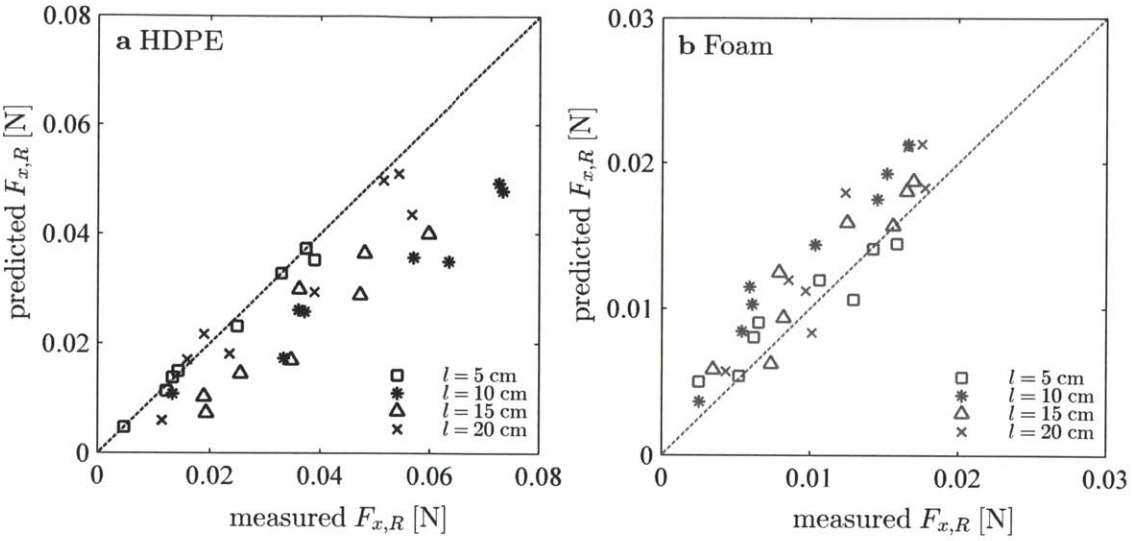

Figure 5-10: (a) Predicted RMS horizontal forces, $F_{x,R}$, plotted against the measurements for the HDPE blades for all test cases. (b) Same as (a) but for foam blades. Blade lengths as indicated on plot.

forces agree very well for the 5 cm-long (squares) and 20 cm-long (crosses) HDPE blades, the measurements are consistently larger than the predictions for the 10 cm-long and 15 cm-long blades. For example, over all eight wave conditions, the ratio of predicted to measured RMS force was 0.66 ± 0.09 (mean $\pm$ s.d.) for the 10 cm-long blades. In contrast, this ratio of predicted to measured force was 0.98 ± 0.05 for the 5 cm-long blades and 0.88 ± 0.20 for the 20 cm-long blades. We discuss why the measured forces were larger than predictions for the 10 cm-long HDPE blades in §5.4.1 below.

5.4 Discussion

Without the use of any tuned parameters (recall that C_D and C_M were based on previous literature for flat plates), the numerical model developed in §5.1 predicts the forces generated by the model blades in laboratory tests reasonably well across a range of blade properties and flow conditions. This confirms that our model captures the salient physics governing the wave-induced dynamics of flexible blades. Specifically, our results suggest that rigid-body C_D and C_M may be used for flexible bodies as

long as the relative, body-normal velocity and acceleration are used to calculate the drag and added mass forces. However, it is important to keep in mind that, although it has been used with relative success in previous studies (and in this chapter), the Morison force formulation is merely a physically intuitive, simplified representation of the true unsteady forces acting on the blade. There are often large differences between the true force generated by the body, and that represented by a sum of the drag and added-mass terms [47] with constant C_D and C_M (see e.g., Fig. 5-6m).

There are differences between the predicted and observed blade postures, especially near the top of the blade (see e.g., Fig. 5-9). We suggest that these discrepancies may arise because we assume that C_D and C_M are constant over the length of the blade. In reality, pressure recovery near the blade tip must lead to a reduction in forces, and therefore a reduction in the effective C_D and C_M. Another possible explanation for these differences could be the fact we do not account for the hydrodynamic force generated due to blade curvature i.e., as the component of flow parallel to the blade accelerates to follow the blade shape. This force is sometimes termed the *reactive* force [9]. In the future, we hope to extend the numerical model to account for these two effects.

5.4.1 Flexibility can enhance forces

Recall that the measured forces were significantly larger than the predictions for the 10 cm-long HDPE blades (Fig. 5-10a). Table 5.1 shows that the Cauchy number ranged from $Ca = 0.24$ to $Ca = 4.0$ for these blades. For $Ca \sim O(1)$, the hydrodynamic forcing and the restoring force due to blade stiffness are comparable. So, over a wave cycle, there can be a transition between forcing-dominated and stiffness-dominated conditions. As illustrated by Fig. 5-11, this transition leads to unsteady blade behavior and an enhancement of forces that cannot be reproduced by the numerical model. Specifically, we observe that a vortex is shed from the blade between time $t = 0.10 - 0.20$ s (Fig. 5-11a-d), which leads to a reduction in the hydrodynamic force acting on the blade at that point in time. Because of this force reduction, the blade springs backwards between $t = 0.3 - 0.6$ s (Fig. 5-11e-g). As the blade springs

backwards, there is significant relative motion between the blade and the water, and this leads to the generation of additional drag (Fig. 5-11h). In contrast to the real blade, the simulated blade moves back gradually in the flow (red lines in Fig. 5-11e-g). Hence, the relative motion between the blade and the water is lower for the simulations, and so is the predicted force (red line in Fig. 5-11h). We suggest that the numerical model cannot reproduce the observed behavior because it employs constant C_D and C_M. In effect, the shedding event leads to a local (in time) reduction in the added mass, C_M.

Note that similar shedding events were also observed for the 5 cm-long and 20 cm-long HDPE blades. However, because $Ca < 1$ for the 5 cm-long blade, it remained motionless throughout the wave cycle, i.e., it was essentially rigid. For the 20 cm-long blade, the Cauchy number was $Ca \gg 1$, and so we suggest that this blade was not stiff enough to spring backwards following the local (in time) reduction in the hydrodynamic forcing. Recall that for the same wave condition, the numerical model was able to predict the measured forces reasonably well for both the 5 cm-long (Fig. 5-6) and 20 cm-long (Fig. 5-8) HDPE blades.

Interestingly, because of this unsteady blade behavior, the RMS force generated by the flexible 10 cm-long HDPE blade was greater than that predicted for a rigid 10 cm-long blade (blue line in Fig. 5-11h) for the same wave condition. Specifically, $F_{x,R} = 0.074$ N for the flexible blade, while we expect $F_{x,R} = 0.070$ N for a rigid blade. Indeed, for most of the laboratory tests with the 10 cm-long HDPE blades, the measured $F_{x,R}$ was greater than that predicted for a rigid blade (see Fig. 5-12 below). Observations of blade motion suggest that a mechanism similar to the one described here (i.e., blade springing back) may be responsible for this enhancement. Note that the rigid-blade force was calculated using the PIV-measured velocity field, $u_w(z,t)$, as:

$$F_x(t) = \int_0^l \frac{1}{2}\rho C_D b |u_w| u_w + \rho\left(\frac{\pi}{4}b^2 C_M + bd\right)\frac{\partial u_w}{\partial t}\, dz \tag{5.16}$$

The first term inside the integral is the drag force (see Eq. 5.4), and the second term

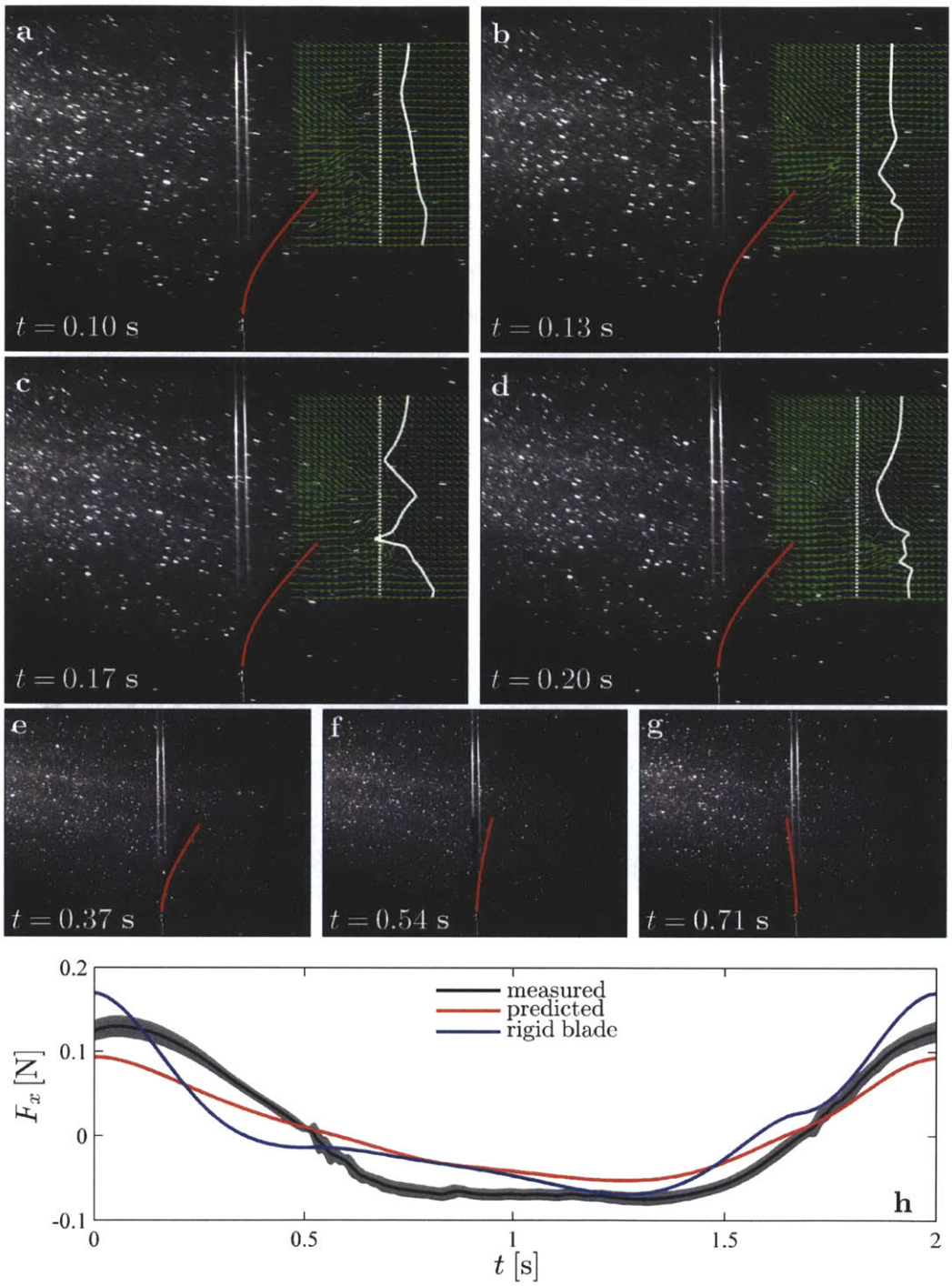

Figure 5-11: (a-d) Blade postures and PIV velocity field (green arrows) for 10 cm-long HDPE blade between $t = 0.1 - 0.2$ s in waves of period $T_w = 2.0$s and amplitude $a_w \approx 4$ cm. The solid white line shows the variation in horizontal velocity along the dotted white line. (e-f) Vortex shedding leads to the HDPE blade springing backwards between $t \approx 0.3 - 0.6$ s. (g) A comparison of measured (black), predicted (red), and rigid-blade (blue) forces.

represents the added mass and virtual buoyancy forces (see Eqs. 5.5 and 5.3).

5.4.2 Effective blade length

Most of the discussion in §4 was presented in terms of an effective blade length. This effective length, l_e, was defined as the length of a rigid, upright blade that generates the same horizontal drag as the flexible blade of length l. Because of the time-varying nature of the hydrodynamic forces generated, the effective length can be defined in multiple different ways for oscillatory flows. We define the effective length based on the RMS force:

$$\frac{l_{e,R}}{l} = \frac{measured\ F_{x,R}}{rigid\ F_{x,R}} \tag{5.17}$$

However, one may also use, for example, the maximum force over a wave cycle.

Recall that, for flexible blades in unidirectional flow, once the hydrodynamic forcing becomes much larger than blade buoyancy and the restoring force due to blade stiffness, $Ca \gg B$ and $Ca \gg 1$, the following scaling law for effective length applies: $l_e/l \sim Ca^{-1/3}$. This scaling law represents a balance between the restoring force due to stiffness and drag in the reconfigured state, $EI/l_e^2 \sim \rho b l_e U^2$. In other words, both the blade curvature, $(\partial^2\theta/\partial s^2)$, and the pressure drag force, F_x, scale on the effective length, l_e, in this reconfigured state. For wave-induced oscillatory flows, we anticipate that a similar scaling law for $l_{e,R}/l$ would emerge if the ratio of blade length to wave excursion was small, $L \ll 1$. As discussed earlier, at the quasi-steady limit of $L \ll 1$, the flexible blade is pushed over into a bent posture in the early stages of a wave half-cycle, where it remains until the wave velocity reverses. This bent posture must reflect a balance between the hydrodynamic forcing, which is dominated by pressure drag for $L \ll 1$, and the restoring forces.

However, as discussed in §5.1, when the blade length is much larger than the wave excursion, $L \gg 1$, the blade remains nearly upright as it moves back and forth (Fig. 5-2). At this limit, we anticipate small blade angles, $\theta \sim L^{-1} \ll 1$, such that the blade curvature term may be linearized as: $EI(\partial^2\theta/\partial s^2) \approx EI(\partial^3 x_v/\partial z_v^3)$ (see

Eq. 5.15). Here, the horizontal blade excursion would scale on the wave excursion, $x_v \sim A_w$. Therefore, balancing drag and blade stiffness for this limit of $L \gg 1$, we have:

$$EI\frac{\partial^3 x_v}{\partial z_v^3} \sim F_x \;\rightarrow\; EI\frac{A_w}{l_e^3} \sim \rho b l_e U_w^2 \tag{5.18}$$

Using the definition of the Cauchy number Ca (Eq. 5.12) and the ratio L (Eq. 5.11), the above equation can be re-arranged to yield:

$$(l_e/l) \sim (CaL)^{-1/4} \tag{5.19}$$

Essentially, with this scaling, the effective length represents the blade length over which there is significant relative motion between the blade and the water. The upper part of the blade, $z_v > l_e$, moves nearly passively with the flow and therefore, forces are only generated in the lower part, $z_v < l_e$.

To summarize, once the hydrodynamic forcing exceeds the restoring force due to blade stiffness, we expect that $l_{e,R}/l \sim Ca^{-1/3}$ for $L \ll 1$, and that $l_{e,R}/l \sim (CaL)^{-1/4}$ for $L \gg 1$. For the laboratory experiments described in §5.2, the ratio of blade length to wave excursion ranged from $L = 0.8$ to $L = 17$. The measured effective lengths (Eq. 5.17) for all sixty-four laboratory tests, shown in Fig. 5-12, indicate that for this range of L (≥ 0.8), the small-excursion scaling, $l_{e,R}/l \sim (CaL)^{-1/4}$, is more appropriate. For example, all the measured effective lengths for the foam blades (gray symbols in Fig. 5-12b) collapse together, with a best fit power-law suggesting the following relationship: $l_{e,R}/l = 0.70 \pm 0.05(CaL)^{-0.21\pm0.02}$. For $CaL < 1$, the blades are essentially rigid in the flow. This is illustrated by the fact that the effective lengths for the 5 cm-long HDPE blades (black squares in Fig. 5-12) are approximately constant and equal to 1. A best-fit power law suggests $l_{e,R}/l = 1.08 \pm 0.06(CaL)^{0.02\pm0.04}$ (dashed line in Fig. 5-12), confirming that there is no dependence between $l_{e,R}/l$ and CaL, and that $l_{e,R}/l \approx 1$ at this limit, i.e. the blade is behaving like a rigid flat plate. The measurements for the 10 cm-long HDPE blades (black stars in Fig. 5-12) do not conform to the predicted scaling law for effective length. As discussed above, the hydrodynamic forces

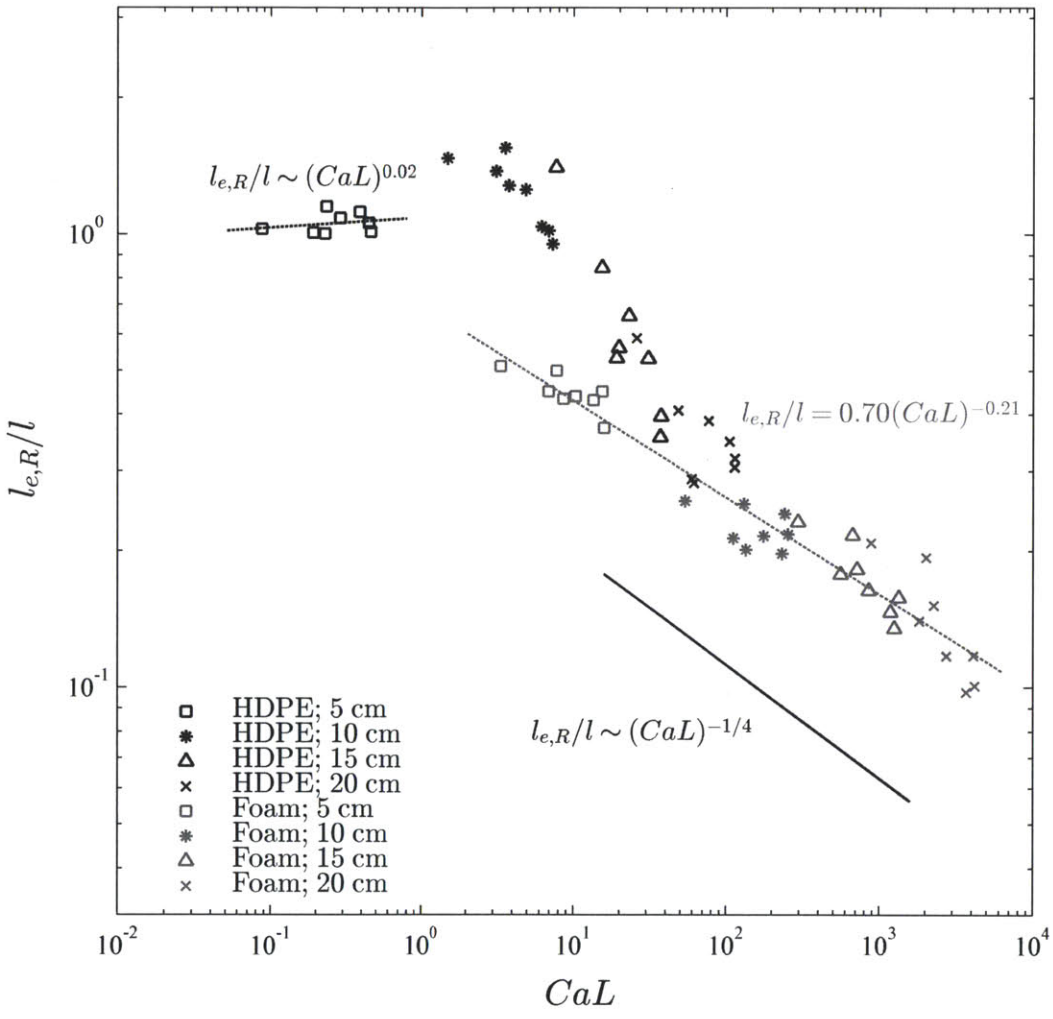

Figure 5-12: $l_{e,R}/l$ plotted against CaL. The solid black line shows the expected scaling for small wave ($L \gg 1$) excursions, $l_{e,R}/l \sim (CaL^{-1/4})$. The dotted gray line shows the best fit to all the foam data. The dotted black line shows the best fit to the 5 cm-long HDPE blade data. Symbols and color scheme as indicated on plot.

generated by these blades were enhanced as they sprung backwards in flow following a vortex shedding event. However, the measured effective lengths for the longer HDPE blades (black crosses in Fig. 5-12b) seem to agree with those measured for the foam blades, suggesting that the scaling $l_{e,R}/l \sim (CaL)^{-1/4}$ may apply again once $Ca \gg 1$. Finally, the effective lengths shown in Fig. 5-12 represent the ratio of the measured RMS force to the RMS force predicted for a rigid blade. The observed trends do not change significantly if, instead of the RMS forces, we use the ratio of the maximum forces, $l_{e,M}/l$. Specifically, best-fits suggest $l_{e,M} = 1.05 \pm 0.12(CaL)^{-0.03\pm0.08}$ for the 5 cm-long HDPE blades, and $l_{e,M}/l = 0.65 \pm 0.07(CaL)^{-0.22\pm0.02}$ for all the foam blades.

In §4, we saw that blade buoyancy delayed the onset of reconfiguration in steady flows until the Cauchy number exceeded the value of the buoyancy parameter, $Ca > B$. Specifically, when plotted against Ca (see Fig. 4-5b), the measured effective lengths for the foam blades formed distinct curves that depended on the value of B. However, buoyancy does not play as important a role for the foam blades moving in wave-induced oscillatory flows. Despite the fact that the buoyancy parameter ranged from $B = 2.7 - 170$, with $Ca < B$ in some cases (Table 5.1), the measured effective lengths all collapse onto a single line. These observations can again be explained by the fact that, for wave-induced oscillatory flows with $L > 1$, the blades remain relatively upright in the flow. For upright blades the contribution of buoyancy to the blade-normal force balance, which dictates blade motion, is negligible. In the governing equation, Eq. 5.9, the buoyancy term is: $iBe^{i\theta}$. The blade-normal (i.e., real) component of this term is $-B\sin\theta$. As discussed above, for $L > 1$ we expect that the angle $\theta \sim L^{-1} \ll 1$, and so $B\sin\theta \sim B\theta \sim (B/L)$. At this limit therefore, buoyancy is only important as long as $(B/L) > Ca$, or $(CaL) < B$. While $Ca < B$ for some of the cases tested in the laboratory, $CaL > B$ for all the cases. Therefore, buoyancy did not play a significant role.

Importantly, the scaling law for effective length shown in Eq. 5.19 assumes that drag is the dominant hydrodynamic forcing. This is reasonable for the range of conditions tested in the laboratory, where the Keulegan-Carpenter number, $KC \geq 3.7$. At the limit of $KC \ll 1$, Eq. 5.9 suggests that the added mass force, which

scales as Ca/KC, would become the dominant hydrodynamic forcing instead of drag, which scales with the Cauchy number, Ca. For this limit, a force balance similar to the one shown in Eq. 5.18, but with added mass instead of drag, leads to $l_e/l \sim (CaL/KC)^{-1/4}$.

The effective length framework developed in this chapter may also be useful for studies of wave attenuation over canopies of flexible vegetation. Wave attenuation by submerged vegetation has been studied in the laboratory [25, 48], in the field [8], and using analytical methods or numerical models [48, 68, 67]. Most of these studies recognize that it is the relative motion between water and vegetation that determines energy dissipation. Yet, there is no consistently adopted methodology to account for vegetation motion. In an analytical study, Mendez et al. [68], account for plant motion by imposing a blade excursion that increases linearly with height, and use the resulting relative velocity to calculate drag. In a field study, Bradley and Houser [8], account for blade motion by recording the movement of seagrass blade tips from above, and assuming a cantilever model to translate tip excursion into blade motion over the entire blade height. Most other studies (e.g., Mendez and Losada [67]) use bulk drag coefficients that are calibrated to account for vegetation motion.

Without a consistent framework, it is difficult to make comparisons across species and systems. For example, the drag coefficient calibrations typically employ the Reynolds number, Re, or Keulegan-Carpenter number, KC, as the independent governing parameters [8, 48, 67]. Re and KC can be used to account for the variation in drag with hydrodynamic conditions (see e.g., Fig 5-3). However, they cannot account for any drag reduction due to plant flexibility because they do not reflect the underlying physics. Given the likely variation in vegetation stiffness and buoyancy, the calibrated drag coefficient for one species will not hold for another species. Instead, we suggest the use of an effective length, l_e, to account for vegetation motion. The effective length approximates the length of blade over which relative motion between the blades and the water is significant. So wave energy dissipation within the meadow can be calculated by assuming that the vegetation is rigid, but of length l_e, rather than l. Further, a characterization of l_e/l as a function of the dimensionless

parameters that govern blade motion Ca, B, and L, is likely to hold across systems.

Note that, for field studies, Ca, B, and L, may be calculated based on measured vegetation properties, and the significant wave height, H_S, and peak period, T_P (see §3.3). However, because of the broadband nature of waves in the field, defining an effective length is more difficult. As observed by Bradley and Houser [8], the blades may move in response to secondary frequencies rather than the peak frequency. For such cases, the motion of the blades is not in phase with the water, resulting in some relative motion over the entire blade length even if $l_e < l$.

THIS PAGE INTENTIONALLY LEFT BLANK

Chapter 6

Conclusions and remaining questions

This thesis has explored many aspects of the interaction between flow and aquatic vegetation. We have studied physical processes at the scale of individual blades as well as entire canopies; in steady and unsteady flows. Here, we summarize our key findings, explore possible environmental and engineering implications, and highlight problems that merit further study.

In §2.1.2, we showed that for submerged vegetation in steady flow, the penetration of turbulence and momentum from the overflow has a significant influence on canopy function. Specifically, for dense canopies where the vegetation frontal area per unit bed area is $ah \geq 0.1$, turbulent stress cannot penetrate to the bed. Above this density a meadow can promote sediment retention, stabilizing the bed and improving light conditions, two positive feedbacks that promote meadow persistence. Conversely, a reduction in canopy density below this threshold will lead to increased flow and stress near the bed, increased sediment resuspension, a loss of bed stability, and a reduction in light climate, all of which can lead to further canopy deterioration.

In §2.2, we considered how the distribution of vegetation in a channel affects the hydraulic resistance and velocity. Using a simplified momentum balance, we showed that the Manning roughness, n_M, due to vegetation depends primarily on the blockage factor, B_X, which is the fraction of the channel cross-section blocked

by vegetation. Specifically, for $B_X < 0.8$, we anticipate that $n_M \propto (1 - B_X)^{-3/2}$. Although, approaching the limit where the entire channel is blocked by vegetation ($B_X = 1$), the roughness depends on the canopy frontal area parameter, a. Our model also suggests that, for the same channel blockage $B_X(< 0.8)$, the velocity decreases if vegetation is distributed as small patches rather than large contiguous blocks, because the interfacial area between the flow and the vegetation increases with an increasing number of patches. There is limited experimental support for this hypothesis in existing literature (e.g. [3]). However, further laboratory experiments testing varying plant distributions are required to quantify the effect of vegetation patchiness on velocity and channel resistance.

For natural channels, the effect of vegetation patchiness is likely to be small; we estimate reductions of velocity $< 20\%$. This is comparable to the uncertainty with which vegetation distributions can be measured at the reach scale using remote sensing techniques (e.g. [99, 83]). So for now, incorporating the effect of specific vegetation distributions at the reach scale may be impractical. One exception, for which the specific distribution of vegetation may be of current practical interest, is managed channels where vegetation is mowed periodically to reduce hydraulic resistance; mowing patterns that produce less interfacial area per channel length (e.g. a single continuous cut on one side of the channel) are likely to be the most effective in reducing hydraulic resistance.

In §3, we showed that a mean current is generated within seagrass meadows under wave forcing. Similar to boundary layer streaming, this mean current is forced by a nonzero wave stress. This induced mean current could play an important role in the net transport of suspended sediment and organic matter. By continuously renewing the water within the meadow, the induced current may also mediate the ecologically and economically important nutrient cycling services provided by seagrass meadows. A simple model, developed in §3.1.2, is able to predict the magnitude of the measured mean currents in the laboratory reasonably well. However, this model under-predicts the velocities measured in the field by a factor of ~ 4. We believe that this difference arises primarily because the model developed in §3.1.2 does not

account for plant flexibility. To the best of our knowledge, no previous studies have studied the drag generated by flexible plants in combined wave-current flows, and so a range of important questions remain unanswered. For example, is the two-term drag formulation used in §3.1.2 appropriate for flexible plants? If so, how do the wave (C_{Dw}) and current (C_{Dc}) drag coefficients vary with hydrodynamic conditions and plant properties?

The laboratory and field measurements described in §3 also showed that wave-induced oscillatory flows are damped less within seagrass canopies compared to unidirectional flows. The higher in-canopy velocities associated with wave-dominated conditions have been observed to enhance nutrient and oxygen transfer between the seagrasses and the water [97]. Further, the limited reduction of in-canopy oscillatory velocities suggests that in wave-dominated regions, the bed stress is not sufficiently distinct in any cuts or channels compared to areas of healthy meadow. Hence, seagrasses may be able to recolonize areas of lost meadow, leading to more uniform meadow structure. This is in contrast to tidal- or current-dominated regions where any cuts or channels tend to be stable because of the local increase in flow and hence, bed stress [96].

In §4, we showed that a simple model balancing the effects of hydrodynamic drag with the restoring forces due to vegetation stiffness and buoyancy can successfully predict posture and drag for a range of model and natural aquatic vegetation in steady flows. We also showed that the scaling law, $F_x \propto U^{4/3}$, consistently describes the relationship between drag and velocity as flexible plants reconfigure in flow. This scaling represents a balance between hydrodynamic drag and the restoring force due to plant stiffness in the reconfigured state. Further, by incorporating blade-scale reconfiguration into a canopy-scale momentum balance (§4.4.2), we demonstrated that the reduction in drag and channel blockage, B_X, due to plant flexibility can reduce the Manning roughness and increase velocities significantly. The canopy-scale momentum balance presented in §4.4.2 was based on a two-box formulation where a constant friction factor C_v was used to model the shear stress at the interface between the vegetation canopy and the overflow. However, measurements made by

Ghisalberti and Nepf [35] suggest that, for flexible plants, C_v decreases with increasing velocity because the interface between the vegetation canopy and the overflow becomes smoother as the plants reconfigure in flow. Since a similar momentum balance model successfully predicts the roughness produced by channel vegetation at the reach-scale (§2.2), further experiments quantifying the reduction in C_v with velocity could be useful for field application.

In §5, we showed that the wave-induced dynamics of flexible plants can be characterized by extending the force balance developed in §4 to account for oscillatory flows. For flexible blades ($Ca \gg 1$), we defined two different limits of blade behavior based on the ratio of the blade length to the wave excursion, L. When the blade length is much longer than the wave excursion, $L \gg 1$, the blade remains upright as it moves back and forth with the wave-induced flow. In contrast, when the wave excursion is much longer than the blade length, $L \ll 1$, the blade bends over during the early stages of a wave half-cycle and remains in a bent posture until the flow reverses (i.e., similar behavior to that in a unidirectional current). We developed scaling laws that described the relationship between drag and velocity for both these limits. However, the laboratory experiments described in §5.2 only spanned the range $L \geq O(1)$. For this range, the scaling law developed for the small excursion limit, $L \gg 1$, applied. So, the transition between the large- and small-excursion limits is yet to be described experimentally.

The canopy- and reach-scale studies described in §2 and §3 showed that the drag generated by flexible plants has important ecological and engineering implications. However, there is no universally accepted framework to describe drag reduction for flexible plants. Given the success of the models developed in §4 and §5, we suggest that future work should be framed in terms of the dimensionless parameters that dictate the reconfiguration of flexible plants in steady flows, and govern plant motion in oscillatory flows: Ca, B, and L. The use of this convention will make a quantitative comparison possible across vegetation species and hydrodynamic conditions. Such an approach would be especially useful in the wave decay literature, where most existing studies fit drag coefficients to measurements. A reanalysis that translates the fitted

drag coefficients into effective lengths (defined in §5), and considers the variation of these effective lengths with Ca, B, and L, would be a useful first step towards bringing together existing data, as well as providing a consistent methodology for future work.

THIS PAGE INTENTIONALLY LEFT BLANK

Appendix A

Programmable wavemaker

The wave experiments described in §3.2 and §5.2 were carried out in a 24 m-long, 38 cm-wide, 60 cm-deep flume fitted with a piston-type wavemaker (Fig. A-1). The piston displacement as a function of time, $\xi(t)$, was controlled by a voltage signal, $V(t)$, from a programmable signal generator (Syscomp WGM-101). Through a graphic user interface (GUI), the WGM-101 allows users to generate voltage signals of any shape (e.g. sinusoidal, square-wave, saw-tooth, or user-defined) at a desired amplitude, V_0, and frequency, f. Tests with sinusoidal voltage signals, $V(t) = V_0 \sin(2\pi ft)$, showed that the piston displacement was proportional to the voltage signal; however, the constant of proportionality, C_w, decreased with the frequency of the sinusoidal signal, f, i.e. $\xi(t) = C_w(f)V_0 \sin(2\pi ft)$. The variation of C_w with frequency is given in Table A.1.

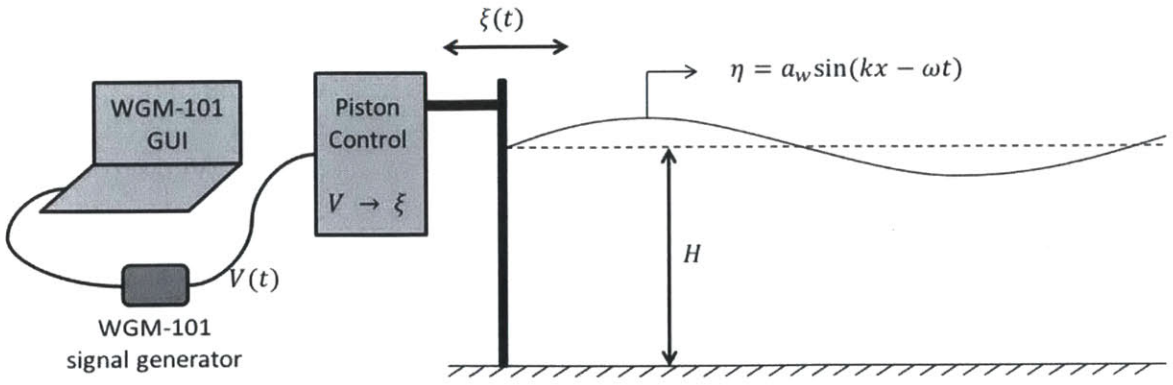

Figure A-1: Schematic showing the programmable piston-type wavemaker.

Table A.1: Variation in piston response coefficient with frequency

f	[Hz]	0.0	0.1	0.3	0.5	0.7	0.9
C_w	[cm V^{-1}]	3.2	3.2	3.1	3.0	2.9	2.8

To generate water waves of a desired frequency, f, and amplitude, a_w, in water depth H, we employed the closed form solution for piston motion given in Madsen [60]. Specifically, Madsen [60] showed that to generate sinusoidal waves, $\eta = a_w \sin(2\pi f t)$, without the *bound* and *free* secondary harmonics (see Madsen [60] for details), the piston motion must be prescribed as:

$$\xi(t) = \xi_0 \left(\cos(\omega t) + \frac{a_w}{2 n_1 H} \left(\frac{3}{4 \sinh^2(kH)} - \frac{n_1}{2} \right) \sin(2\omega t) \right) \tag{A.1}$$

Recall that $\omega = 2\pi f$ is the radian frequency, and k is the wavenumber, with $\omega^2 = kg \tanh(kH)$. The variables ξ_0 and n_1 are:

$$\xi_0 = \frac{a_w n_1}{\tanh(kH)} \tag{A.2}$$

$$n_1 = \frac{1}{2} \left(1 + \frac{2kH}{\sinh(2kH)} \right) \tag{A.3}$$

A MATLAB (Mathworks,Inc.) script to generate a wave form of the shape described by Eq. A.1 is given below (`syscomp_final.m`). This script outputs text files that can be loaded onto the WGM-101 signal generator. As an example, to generate waves of amplitude $a_w = 2.0$ cm, frequency $f = 0.5$ Hz, in water depth $H = 39$ cm:

1. The user types in `syscomp_final(2,0.5,39)` in the MATLAB command window. This generates a text file with the name: `final_aw2f0.5H39V2.txt`.

2. The user loads this file onto the signal generator using the WGM-101 GUI button `Load user waveform`.

3. The desired waves can be produced by setting the `Frequency` slider to 0.5 Hz and the `Voltage` slider on the WGM-101 GUI to the value indicated on the file name: 2.0V (`...V2.txt`).

```
function[]=syscomp_final(aw,f,H)
% Function to generate a waveform file to cancel the free second harmonic that can
    be read by the function generator. For a theoretical derivation, see Madsen
    (1971)
% aw is the desired wave amplitude (cm)
% f  is the wave frequency (Hz)
% H  is the water depth (cm)
% Vmax is the voltage set on the syscomp WGM-101 GUI (V)

%Input Conditioning
if(H>45)
    disp('The small wave flume should not have H > 45 cm');
    return
elseif (aw>0.3*H)
    disp('Wave amplitude is high. Expect non-linearity');
elseif (mod(f,0.1)~=0)
    disp('Please enter frequency in 0.1 Hz increments');
    return
end

%Gravity
g = 981;     %[cm/s/s]
%Piston displacement coefficients [cm/V]
freq = [0,0.1:0.2:0.9]; %[Hz]
C = [3.2,3.2,3.1,3.0,2.9,2.8];
%Interpolate
Cw = spline(freq,C,f); %[cm/V]

%Radian frequency [rad/s]
w = 2*pi*f;
%Find the wavenumber using the linear dispersion relation
k_trial = 0.001:0.001:1;
error_k = w*w-g*k_trial.*tanh(H*k_trial);
[~,k_index] = min(abs(error_k));
k = k_trial(k_index);                %Wavenumber [/cm]

%Calculate all the variables needed
n1 = 0.5*(1+(2*k*H/sinh(2*k*H)));  %Cg/Cp
X0 = aw*n1/(tanh(k*H));              %Piston motion amplitude[cm]
V0 = X0/Cw;                          %Maximum voltage required
Vmax = ceil(V0);                     %TO BE SET ON THE WGM-101 GUI

if(Vmax<9)
    disp(strcat('Please set the voltage amplitude on the WGM-101 GUI to: ',num2str(
        Vmax,'%0.1f'),'V'));
```

```
    disp('See also the name for the output text file.');
elseif (V0>9)
    disp('Error: You should not need voltages this high. Check input parameters.')
    return
end

%Calculate the waveform
i = 0:255;
V = V0*(cos(2*pi*i/256)+0.5*Cw*V0*tanh(k*H)*((0.75/(sinh(k*H)^2))-(0.5*n1))*sin(4*
    pi*i/256)/(H*n1*n1));
S = V0*cos(2*pi*i/256);
%Plot to compare with basic sine wave
plot(i,V,'k')
hold on
plot(i,S,'k:')

%Convert to a format accessible by the function generator and write to file
%Make the numbers palatable for the function generator
V = 0.5*V/Vmax;      %Normalise to Vmax
V = 255*V;           %Scale to 255
V = round(V);        %Round to integers
V = V + 128;         %Shift everything up to zero
V = 255-V;           %Invert for the hardware

%Save to a text file
fileId = fopen(strcat('final_aw',num2str(aw),'f',num2str(f),'H',num2str(H),'V',
    num2str(Vmax),'.txt'),'w');
for i = 0:255
    fprintf(fileId,'%d\n',V(i+1));
end
fclose(fileId);

end
```

Appendix B

Shooting method to calculate blade posture

To solve the equation governing blade posture shown in §4.1 (Eq. 4.6, repeated below for convenience), we employed a standard shooting method [90]. Recall that the governing equation was:

$$-\left.\frac{d^2\theta}{d\hat{s}^2}\right|_{\hat{s}^*} + B(1-\hat{s}^*)\sin\theta^* = Ca\int_{\hat{s}^*}^{1}\cos^2\theta\cos(\theta-\theta^*)\,d\hat{s} \tag{B.1}$$

and the boundary conditions were $\theta = 0$ at $\hat{s} = 0$, and $d\theta/d\hat{s} = 0$ at $\hat{s} = 1$. Using the alternative coordinate, $r = 1 - \hat{s}$, Eq. B.1 can be rewritten as:

$$-\left.\frac{d^2\theta}{dr^2}\right|_{r^*} + B(r^*)\sin\theta^* = Ca\left(\cos\theta^*\int_0^{r^*}\cos^3\theta\,dr + \sin\theta^*\int_0^{r^*}\cos^2\theta\sin\theta\,dr\right) \tag{B.2}$$

and the boundary conditions become $\theta = 0$ at $r = 1$, and $d\theta/dr = 0$ at $r = 0$. Eq. B.2 can be discretized in space as:

$$-\left(\frac{\theta_{i+1} - 2\theta_i + \theta_{i-1}}{\Delta^2}\right) + Br_i\sin\theta_i \approx Ca\left(\cos\theta_i I_i^1 + \sin\theta_i I_i^2\right) \tag{B.3}$$

Here, θ_i is the blade angle at grid-point r_i. There are N grid-points and so, the spatial step size is $\Delta = r_{i+1} - r_i = 1/(N-1)$. With this discretization, $r_1 = 0$, $r_i = (i-1)\Delta$, and $r_N = 1$. To first order, the discrete integrals I_i^1 and I_i^2 can be approximated as:

$$I_i^1 = \sum_2^i (\cos^3 \theta_{i-1/2})\Delta \tag{B.4}$$

$$I_i^2 = \sum_2^i (\cos^2 \theta_{i-1/2} \sin \theta_{i-1/2})\Delta \tag{B.5}$$

where $\theta_{i-1/2} = (1/2)(\theta_i + \theta_{i-1})$. Note that $I_1^1 = I_1^2 = 0$. Finally, Eq. B.3 can be re-arranged to yield:

$$\theta_{i+1} \approx 2\theta_i - \theta_{i-1} + \Delta^2 \left(Br_i \sin \theta_i - Ca \left(\cos \theta_i I_i^1 + \sin \theta_i I_i^2 \right) \right) \tag{B.6}$$

The shooting method works as follows. We start with three initial guesses for $\theta_1 = [0, \pi/4, \pi/2]$. The free boundary condition ($d\theta/dr = 0$ at $r = 0$) leads to $\theta_2 = \theta_1$. Using the discretization shown in Eq. B.6, the governing equation for blade posture (Eq. B.2) is integrated numerically from the blade tip ($r = 0$ or r_1) to the base ($r = 1$ or r_N) for these three initial guesses to yield θ_i for $i = 1$ to N. Next, the three numerical solutions are used to evaluate which of the two intervals spanned by the initial guesses (e.g. $\theta_1 = [0 - \pi/4]$ or $[\pi/4 - \pi/2]$) contains the true solution that satisfies the clamped boundary condition at the base ($\theta = 0$ at $r = 1$, or $\theta_N = 0$). The governing equation is then integrated for three guesses for the blade tip angle, θ_1, that span the smaller interval containing the true solution (e.g. $\theta_1 = [0, \pi/8, \pi/4]$ or $\theta_1 = [\pi/4, 3\pi/8, \pi/2]$). This interval-bisection procedure is repeated until the interval is smaller than the desired accuracy for θ. The MATLAB code listing provided below (`shooting_final`) performs this procedure for given values of N (grid-points), Ca (Cauchy number, Eq. 4.8), and B (Buoyancy parameter, Eq. 4.7).

```
function [s,thetafinal] = shooting_final(N,Ca,B)
%Function to calculate blade posture based on the shooting method
%N is the number of gridpoints
%Ca: Cauchy Number = Drag/Rigidity
%B : Buoyancy Parameter = Buoyancy/Rigidity

%Starts from the free boundary condition at the tip
%The blade coordinate is s. s = 0 at the bed and s = 1 at the tip.
%This code uses r = 1-s

%Domain and difference
r = linspace(0,1,N);
dr = r(2)-r(1);
s = 1-r;
%Tolerance for theta
eps = 0.01/N;
%Initial guesses for tip angle
tip = linspace(0,pi/2,3);
%Initial guess for theta
theta = ones(N,1)*tip;

while(abs(theta(end,end)-theta(end,1))>eps)
    %Initial guess for theta
    theta = ones(N,1)*tip;
    %Loop to step forward in space
    for i = 2:(N-1)
        %averaging for discrete integrals
        tavg = 0.5*(theta(1:(i-1),:) + theta(2:i,:));
        %discrete integrals
        I1 = Ca*sum(dr*(cos(tavg).^3));
        I2 = Ca*sum(dr*(sin(tavg).*(cos(tavg).^2)));
        %step forward along r (=1-s)
        dthta = min(zeros(1,3),(B*r(i)*sin(theta(i,:))-I1.*cos(theta(i,:))-I2.*sin
            (theta(i,:))));
        theta(i+1,:) = 2*theta(i,:) - theta(i-1,:) + dr*dr*dthta;
    end
    %Logic to calculate next theta interval
    if (theta(end,1)*theta(end,2)<0)
        %Opposite signs for theta, so the real solution must lie in between
        tip = linspace(theta(1,1),theta(1,2),3);
    elseif (theta(end,2)*theta(end,3)<0)
        tip = linspace(theta(1,2),theta(1,3),3);
    elseif (theta(end,2)==0)
        thetafinal = fliplr(theta(:,2)');
        s = fliplr(s);
```

```
        return
    else
        disp('error: system will not converge')
        return
    end
end
thetafinal = fliplr(theta(:,2)');
s = fliplr(s);
end
```

Appendix C

Dynamic blade model

The real part of the equation governing the wave-induced dynamics of flexible blades Eq. 5.9, which describes the blade-normal force balance, is:

$$-\frac{\partial^3\theta}{\partial\hat{s}^3}+\hat{T}\frac{\partial\theta}{\partial\hat{s}}-B\sin\theta+\frac{1}{2}C_DCa\,|\Re(\hat{u}_re^{i\theta})|\Re(\hat{u}_re^{i\theta})$$

$$+\frac{2\pi^2}{4}C_M\frac{Ca}{KC}\Re\left[\left(\frac{\partial\hat{u}}{\partial\hat{t}}-L\frac{\partial^2\hat{x}}{\partial\hat{t}^2}\right)e^{i\theta}\right]$$

$$+2\pi\frac{Ca\,S}{KC}\Re\left[\left(\frac{\partial\hat{u}}{\partial\hat{t}}-\rho' L\frac{\partial^2\hat{x}}{\partial\hat{t}^2}\right)e^{i\theta}\right]=0 \tag{C.1}$$

Employing the inextensibility condition, we can rewrite the time-derivatives in $\hat{x}$ as:

$$\hat{x}=\int_0^{\hat{s}} ie^{-i\theta}\,d\hat{s}' \tag{C.2}$$

$$\frac{\partial\hat{x}}{\partial\hat{t}}=\int_0^{\hat{s}}\frac{\partial\theta}{\partial\hat{t}}e^{-i\theta}\,d\hat{s}' \tag{C.3}$$

$$\frac{\partial^2\hat{x}}{\partial\hat{t}^2}=\int_0^{\hat{s}}\left[\frac{\partial^2\theta}{\partial\hat{t}^2}-i\left(\frac{\partial\theta}{\partial\hat{t}}\right)^2\right]e^{-i\theta}\,d\hat{s}' \tag{C.4}$$

Substituting the above time derivatives into Eq. C.1, and collecting terms, we have:

$$
\begin{aligned}
&-\frac{\partial^3\theta}{\partial\hat{s}^3}+\hat{T}\frac{\partial\theta}{\partial\hat{s}}-B\sin\theta \\
&+\frac{1}{2}C_DCa\,\hat{u}_{rn}\Re\left[e^{i\theta}\left(\hat{u}-L\int_0^{\hat{s}}e^{-i\theta}\frac{\partial\theta}{\partial\hat{t}}\,d\hat{s}'\right)\right] \\
&+\frac{2\pi Ca}{KC}\left(\frac{\pi}{4}C_M+S\right)\Re\left[e^{i\theta}\frac{\partial\hat{u}}{\partial\hat{t}}\right] \\
&=\frac{2\pi Ca\,L}{KC}\left(\frac{\pi}{4}C_M+\rho' S\right)\Re\left[e^{i\theta}\int_0^{\hat{s}}e^{-i\theta}\left[\frac{\partial^2\theta}{\partial\hat{t}^2}-i\left(\frac{\partial\theta}{\partial\hat{t}}\right)^2\right]d\hat{s}'\right] \qquad \text{(C.5)}
\end{aligned}
$$

Here, we linearize the drag term by assuming that the magnitude of the blade-normal relative velocity $\hat{u}_{rn}=|\Re(\hat{u}_r e^{i\theta})|$ is known. Treatment of this term in the numerical scheme is discussed shortly. We discretize Eq. C.5 in time as follows:

$$
\begin{aligned}
&\hat{T}^N\frac{\partial\theta}{\partial\hat{s}}^N-B\sin\theta^N+\frac{1}{2}C_DCa\,\hat{u}_{rn}^N\Re\left(e^{i\theta^N}\hat{u}^N\right) \\
&+\frac{2\pi Ca}{KC}\left(\frac{\pi}{4}C_M+S\right)\Re\left[e^{i\theta^N}\left(\frac{\partial\hat{u}}{\partial\hat{t}}\right)^N\right] \\
&+\frac{2\pi Ca\,L}{KC}\left(\frac{\pi}{4}C_M+\rho' S\right)\Re\left[e^{i\theta^N}\int_0^{\hat{s}}e^{-i\theta^N}i\left(\frac{3\theta^N-4\theta^{N-1}+\theta^{N-2}}{2\Delta}\right)^2 d\hat{s}'\right] \\
&=\frac{\partial^3\theta}{\partial\hat{s}^3}^{N+1}+\frac{1}{2}C_DCa\,L\hat{u}_{rn}^N\Re\left[e^{i\theta^N}\left(\int_0^{\hat{s}}e^{-i\theta^N}\frac{\theta^{N+1}-\theta^{N-1}}{2\Delta}\,d\hat{s}'\right)\right] \\
&+\frac{2\pi Ca\,L}{KC}\left(\frac{\pi}{4}C_M+\rho' S\right)\Re\left[e^{i\theta^N}\int_0^{\hat{s}}e^{-i\theta^N}\frac{\theta^{N+1}-2\theta^N+\theta^{N-1}}{\Delta^2}\,d\hat{s}'\right] \qquad \text{(C.6)}
\end{aligned}
$$

In the above equation, a superscript N refers to values for that variable at time step $\hat{t}^N$. The difference between subsequent time steps is $\Delta=\hat{t}^{N+1}-\hat{t}^N$. Note that

the third-order spatial derivative in θ is treated implicitly. The nonlinear acceleration term $\sim (\partial\theta/\partial\hat{t})^2$ (see the last line in Eq. C.5) is evaluated using a backward difference. Similarly, we also evaluate the magnitude of the blade-normal relative velocity with a backward difference:

$$\hat{u}_{rn}^N = \left| \Re \left[e^i \theta^N \left(\hat{u}^N - \frac{3\hat{x}^N - 4\hat{x}^{N-1} + \hat{x}^{N-2}}{2\Delta} \right) \right] \right| \tag{C.7}$$

To discretize Eq. C.6 in space, we use a finite difference method with M evenly spaced grid points, $s_1, s_2, ...s_M$; s_1 corresponds to $\hat{s} = 0$ and s_M corresponds to $\hat{s} = 1$. The spacing is $\delta s = s_{j+1} - s_j = 1/(M-1)$. The spatial derivatives were evaluated using standard second-order-accurate difference matrices. The integrals shown on the last two lines of Eq. C.6 were evaluated as follows:

$$\begin{aligned} I_C(A^N) &= \Re \left[e^{i\theta^N} \int_0^{\hat{s}} e^{-i\theta^N} A^N \, d\hat{s}' \right] \\ &= \int_0^{\hat{s}} \cos[\theta^N(\hat{s}) - \theta^N(\hat{s}')] A^N \, d\hat{s}' \\ &\rightarrow \delta s \begin{bmatrix} 0 & \cdots & & 0 \\ \cos(\theta_1^N - \theta_1^N) & 0 & & \vdots \\ \vdots & \ddots & 0 & \\ cos(\theta_M^N - \theta_1^N) & \cdots & \cos(\theta_M^N - \theta_M^N) & 0 \end{bmatrix} \begin{bmatrix} A_1^N \\ A_2^N \\ \vdots \\ A_M^N \end{bmatrix} \end{aligned} \tag{C.8}$$

The integral on the third line of Eq. C.6 was also evaluated in a similar fashion. Note that, because the integrand is imaginary, $\cos[\theta^N(\hat{s}) - \theta^N(\hat{s}')]$ in Eq. C.8 is replaced by $\sin[\theta^N(\hat{s}) - \theta^N(\hat{s}')]$. Using the notation $I_C^N(\cdot)$ and $I_S^N(\cdot)$ to represent these discrete integrals, and the notation D_1 and D_3 to represent discrete first- and third-order spatial derivatives, the governing Eq. C.6 can be written as:

$$\hat{T}^N D_1 \theta^N - B \sin\theta^N + \frac{1}{2} C_D Ca \, \hat{u}_{rn}^N \, A_U^N + \frac{2\pi Ca}{KC} \left(\frac{\pi}{4} C_M + S \right) A_{UT}^N$$

$$-\frac{2\pi Ca\,L}{KC}\left(\frac{\pi}{4}C_M+\rho' S\right)I_S^N\left(\frac{3\theta^N-4\theta^{N-1}+\theta^{N-2}}{2\Delta}\right)^2$$

$$=D_3\theta^{N+1}+\frac{1}{2}C_D Ca\,L\,\hat{u}_{rn}^N\,I_C^N\left(\frac{\theta^{N+1}-\theta^{N-1}}{2\Delta}\right)$$

$$+\frac{2\pi Ca\,L}{KC}\left(\frac{\pi}{4}C_M+\rho' S\right)I_C^N\left(\frac{\theta^{N+1}-2\theta^N+\theta^{N-1}}{\Delta^2}\right) \tag{C.9}$$

Where $A_U^N = \Re(e^{i\theta^N}\hat{u}^N)$, and $A_{UT}^N = \Re[e^{i\theta^N}(\partial\hat{u}/\partial\hat{t})^N]$. Equation C.9 represents a system of linear equations for blade posture at the next time step, θ^{N+1}, that depend on the internal blade tension and posture at the current and previous time steps ($\hat{T}^N$, θ^N, θ^{N-1} etc.), as well as the known velocity and acceleration fields, $\hat{u}^N$ and $(\partial\hat{u}/\partial\hat{t})^N$. We solve this system of equations using the built-in solvers in MATLAB. A code listing (`dynamicblade_FINAL`) is provided below.

The internal blade tension, $\hat{T}^N$, was calculated implicitly by solving the imaginary component of the governing Eq. 5.9:

$$D_1\hat{T}^N+D_1\theta^N\,D_2\theta^N+B\cos\theta^N$$

$$+\frac{2\pi Ca}{KC}\Im\left[e^{i\theta^N}\left(\frac{\partial\hat{u}}{\partial\hat{t}}^N-\rho' L\frac{\partial^2\hat{x}}{\partial\hat{t}^2}^N\right)\right]$$

$$+\frac{1}{2}C_f Ca\left|\Im\left[e^{i\theta^N}\left(\hat{u}^N-L\frac{\partial\hat{x}}{\partial\hat{t}}^N\right)\right]\right|\Im\left[e^{i\theta^N}\left(\hat{u}^N-L\frac{\partial\hat{x}}{\partial\hat{t}}^N\right)\right]=0 \tag{C.10}$$

Where we use backward differences to calculate the blade velocity and acceleration (see last two lines in Eq. C.10). Note that, for generality, we also include a skin-friction term here (last line in Eq. C.10), which acts in the blade-parallel direction. Finally, the program below uses the PIV-measured velocities and accelerations as forcing. However, it can be modified easily to use known functions for velocity and acceleration (e.g. from linear wave theory).

```
function [] = dynamicblade_FINAL(material,lv,f,a)
%Numerical model to simulate dynamic behavior of flexible blades under
%wave forcing. Refer to model derivation from 11/30/2011
%material is either Foam or HDPE
%lv is the length (cm), a is the wave amplitude (cm) and f is the frequency
%(Hz)
%% Blade and other paramters [cm/g/s]
if (strcmp(material,'HDPE'))
  tv = 0.04;        %thickness
  rhov = 0.95;      %density
  Ev = 2.07*9.3e9;  %Young's modulus
  basedir = 'C:\Users\Mitul\Documents\Heidi Nepf\Experiments\Flow-Structure Waves
      \2012 03 28 HDPE';
elseif (strcmp(material,'Foam'))
  tv = 0.19;        %thickness
  rhov = 0.67;      %density
  Ev = 5.0e6;       %Young's modulus
  basedir = 'C:\Users\Mitul\Documents\Heidi Nepf\Experiments\Flow-Structure Waves
      \2012 03 29 Foam';
else
  disp('Error: Unknown material')
  return
end
directory = strcat(basedir,'\lv',num2str(lv,'%0.2d'),'\f',num2str(10*f,'%0.2d'),'a
    ',num2str(10*a,'%0.2d'));
bv = 2.0;         %width
Iv = bv*(tv^3)/12;  %Second moment of area
rho = 1;          %density
g = 981;          %gravity
om = 2*pi*f;      %radian frequency

%% Load measured wave velocities based on the PIV measurements
%Load PIV measured velocities
cmtopix = 4/130;
dt = 1/60;
load(strcat(directory,'\',material,'lv',num2str(lv,'%0.2d'),'f',num2str(10*f,'%0.2
    d'),'a',num2str(10*a,'%0.2d'),'PIV.mat'));
for i = 1:length(u)
  u_temp = u{i,1}; %u is the PIV-measured horizontal velocity at step i
  v_temp = v{i,1}; %v is the vertical velocity
  UU(:,i) = u_temp(:,3)*cmtopix/dt; %from [pix/imag pair] to [cm/s]
  VV(:,i) =-v_temp(:,3)*cmtopix/dt;
end
UU = inpaint_nans(UU);
VV = inpaint_nans(VV);
```

```
%smooth
for i = 1:max(size(y_conv))
  UU(i,:) = smooth(UU(i,:));
  VV(i,:) = smooth(VV(i,:));
end
clear u_temp v_temp u v

%Velocity scale (in cm/s)
[~,z0i] = min(abs(y_conv(:,1)));
U = max(abs(UU(z0i,:)));
clear z0i

%Normalize velocities
UU = UU/U; UUmeas = UU;
VV = VV/U; VVmeas = VV;
%Fit harmonic sinusoidals
t = t_norm';
X = [ones(size(t)) cos(t) sin(t) cos(2*t) sin(2*t) cos(3*t) sin(3*t) cos(4*t)
    sin(4*t)];
for i = 1:max(size(y_conv))
  u_coeffs(:,i) = X\UU(i,:)';
  v_coeffs(:,i) = X\VV(i,:)';
end

%% Now create a searchable grid of velocities from t = 0 to 2pi
t = linspace(0,2*pi,round(60/f)+1)';
clear X
X = [zeros(size(t)) cos(t) sin(t) cos(2*t) sin(2*t) cos(3*t) sin(3*t) cos(4*t)
    sin(4*t)];
%Fitted Velocities
UU = (X*u_coeffs)';
VV = (X*v_coeffs)';
%Calculate accelerations
Xt = [zeros(size(t)) -sin(t) cos(t) -2*sin(2*t) 2*cos(2*t) -3*sin(3*t) 3*cos(3*t
    ) -4*sin(4*t) 4*cos(4*t)];
%Fitted accelerations
UUT = (Xt*u_coeffs)';
VVT = (Xt*v_coeffs)';
clear X Xt

%Vertical coordinate for interpolation
z = y_conv(:,3)+0.5;
%Make dimensionless
z = z/lv;
%Searchable grid for interpolation
```

```
[TT,ZZ]=meshgrid(t,z);
clear t z;

%% Set up model
%Model parameters
ns = 512;          %Number of grid points
s  = linspace(0,1,ns)';%Grid
ds = s(2)-s(1);     %spacing
ndt = 1;
dt = (2*pi*f/60)/ndt;          %Time
nt = ceil(10*2*pi/dt); %Number of time steps
i = sqrt(-1);

%2nd order accurate difference matrices.
D1 = fdmatrix(s,1,2);
D2 = fdmatrix(s,2,2);
D3 = fdmatrix(s,3,2);

%Make matrices for finite differences
%Make matrix for implicit Tension calculation
D1T = D1;
%Fixed BC
D1T(end,:) = 0; D1T(end,end) = 1;
%Make matrix for conversion between theta and X
D1X = D1;
%Fixed BC
D1X(1,:) = 0; D1X(1,1) = 1;

%% Dimensionless Parameters
KC = U*(1/f)/bv;              %Keulegan Carpenter Number
CD = max(1.95,10*KC^(-1/3));%Drag coefficient
CD = CD*ones(ns,1);
CF = 0.1;                     %Friction
 if(KC<20)
   CM1 = 1+(0.35*KC^(2/3));
 else
   CM1 = 1+(0.15*KC^(2/3));
 end
CM2 = 1+((KC-18)^2)/49;
CM = min(CM1,CM2);             %Added mass coefficient
% CM = 1;
rhop = rhov/rho;              %Density ratio
B = (rho-rhov)*g*bv*tv*(lv^3)/(Ev*Iv);  %Buoyancy Parameter -- Buoyancy/Rigidity
Ca = rho*bv*U*U*(lv^3)/(Ev*Iv);      %Cauchy Number -- Drag/Rigidity
L = lv*om/U;                  %Length ratio
```

```
S = tv/bv;                    %Slenderness ratio

%% Estimate force on Rigid body
ZZ_log = logical((ZZ(:,1)>0)&(ZZ(:,1)<1));
for ti = 1:size(TT,2)
  Frigid(1,ti) = sum((0.5*CD(1)*Ca*(abs(UU(ZZ_log,ti)).*UU(ZZ_log,ti))+(2*pi*pi/4)*
      CM*(Ca/KC)*UUT(ZZ_log,ti))*abs((ZZ(2,1)-ZZ(1,1))));
end

%% Initial conditions
%velocity and acceleration
u = zeros(ns,1);
ut = zeros(ns,1);

%theta
theta = zeros(ns,1);
thOld = theta;
thetat = zeros(ns,1);

%Calculate X from theta
RHSX = i*exp(-i*theta); RHSX(1)=0;
X = D1X\RHSX;
XOld = X;       %Previous time step
XOld2= X;       %Two time steps ago
Xt = zeros(ns,1);

%Tension
T = linspace(B,0,ns)';

%% Integrate in time.
for tc = 1:nt
  %Relative velocity normal to blade
  UN = abs(real(exp(i*theta).*(u-L*Xt)));

  %Make lower triangular matrices for integration
  IS = ds*tril(sin(theta*ones(1,ns)-(theta*ones(1,ns))'),-1);
  IC = ds*tril(cos(theta*ones(1,ns)-(theta*ones(1,ns))'),-1);

  %Calculate all the terms treated explicitly
  %Tension, Buoyancy
  A1 = T.*(D1*theta) - B*sin(theta);
  %Drag Forcing
  A2 = (1/2)*Ca*CD.*UN.*real(exp(i*theta).*u);
  %Added mass and virtual buoyancy forcing
  A3 = Ca*real(exp(i*theta).*((2*pi/KC)*(pi*CM/4+S).*ut));
```

```
%Terms due to time discretization
A4 = -Ca*L*(2*pi/KC)*(pi*CM/4+rhop*S).*(IS*(thetat.^2));
A5 = (1/2)*Ca*L*CD.*UN.*(IC*(thOld/2/dt));
A6 = Ca*L*(IC*((2*pi/KC)*(pi*CM/4+rhop*S).*(2*theta-thOld)/dt/dt));

%Total Forcing
RHS = (A1+A2+A3+A4+A5+A6);
%Account for BCs
RHS(1) = 0;
RHS(end) = 0;
RHS(end-1) = 0;

%Calculate the matrix for the LHS
LHS = (D3 + Ca*L*diag((1/2)*CD.*UN/2/dt + (2*pi/KC)*(pi*CM/4+rhop*S)/dt/dt)*IC);
%Fixed boundary condition
LHS(1,:) = 0;
LHS(1,1) = 1;
%No bending moment
LHS(end,:) = D1(end,:);
%No shear force
LHS(end-1,:) = D2(end,:);

%Evaluate!
thNew = LHS\RHS;
RHSX = i*exp(-i*thNew);
RHSX(1)=0;
XNew = D1X\RHSX;

%Update variables
%Rates of change
Xt = (1.5*XNew-2*X+0.5*XOld)/dt;
Xtt = (2.0*XNew - 5*X + 4*XOld - XOld2)/dt/dt;
thetat = (1.5*thNew-2*theta+0.5*thOld)/dt;
%Theta
thOld = theta;
theta = thNew;
%X
XOld2= XOld;
XOld = X;
X = XNew;

%Water velocities and accelerations (from PIV measurements)
%Interpolation time
itime = mod(tc*dt+3*pi/2,2*pi);
%Horizontal
```

```
    ux = interp2(TT,ZZ,UU,itime,imag(X),'linear',interp1(TT(1,:),UU(1,:),itime));
    uxt = interp2(TT,ZZ,UUT,itime,imag(X),'linear',interp1(TT(1,:),UUT(1,:),itime));
    %Vertical
    uz = interp2(TT,ZZ,VV,itime,imag(X),'linear',interp1(TT(1,:),VV(1,:),itime));
    uzt = interp2(TT,ZZ,VVT,itime,imag(X),'linear',interp1(TT(1,:),VVT(1,:),itime));
    %Complex notation
    u = (1-exp(-tc*dt))*(ux+i*uz);
    ut = (1-exp(-tc*dt))*(uxt + i*uzt);

    %Relative velocity along blade
    UT = abs(imag(exp(i*theta).*(u-L*Xt)));

    %Now calculate tension implicitly;
    B1 = -(D2*thNew).*(D1*thNew);
    B2 = -B*cos(thNew);
    B3 = -Ca*(2*pi/KC)*S*imag(exp(i*thNew).*(ut-rhop*L*Xtt));
    B4 = -(1/2)*CF*Ca*UT.*imag(exp(i*thNew).*(u-L*Xt));
    RHST = B1+B2+B3+B4;
    RHST(end) = 0;
    T = D1T\RHST;

    %Parameters to be saved
    saved.theta(:,tc) = theta;
    saved.X(:,tc) = X;
    saved.U(:,tc) = u;
    D2th = D2*theta;
    saved.F(tc) = D2th(1);
end

clearvars -except saved Frigid UU VV UUmeas VVmeas f a Ev Iv bv tv U lv Ca B KC rhop
    L CM CD CF material directory
savestr = 'dynamicblade.mat';
save(savestr)
end
```

Bibliography

[1] Mohamed A. Abdelrhman. Modeling coupling between eelgrass zostera marina and water flow. *Marine Ecology Progress Series*, 338:81–96, 2007.

[2] S. Alben, M. Shelley, and J. Zhang. Drag reduction through self-similar bending of a flexible body. *Nature*, 420(6915):479–481, 2002.

[3] Kris Bal, Eric Struyf, Hans Vereecken, Peter Viaene, Liesbet De Doncker, Eric de Deckere, Frank Mostaert, and Patrick Meire. How do macrophyte distribution patterns affect hydraulic resistances? *Ecological Engineering*, 37(3):529–533, 2011.

[4] J. W. Barko and W. F. James. Effects of submerged aquatic macrophytes on nutrient dynamics, sedimentation, and resuspension. *Structuring Role of Subbmerged Macrophytes in Lakes*, 131:197–214, 1998.

[5] R. D. Blevins. *Applied Fluid Dynamics Handbook.* 1984.

[6] M. L. Boller and E. Carrington. The hydrodynamic effects of shape and size change during reconfiguration of a flexible macroalga. *Journal of Experimental Biology*, 209(10):1894–1903, 2006.

[7] T. J. Bouma, M. B. De Vries, E. Low, G. Peralta, C. Tanczos, J. Van de Koppel, and P. M. J. Herman. Trade-offs related to ecosystem engineering: A case study on stiffness of emerging macrophytes. *Ecology*, 86(8):2187–2199, 2005.

[8] Kevin Bradley and Chris Houser. Relative velocity of seagrass blades: Implications for wave attenuation in low-energy environments. *Journal of Geophysical Research F: Earth Surface*, 114:F01004, 2009.

[9] P. Buchak, C. Eloy, and P. M. Reis. The clapping book: Wind-driven oscillations in a stack of elastic sheets. *Physical Review Letters*, 105:194301, 2010.

[10] Nian-Sheng Cheng. Representative roughness height of submerged vegetation. *Water Resources Research*, 47:W08517, 2011.

[11] R. Costanza, R. dArge, R. deGroot, S. Farber, M. Grasso, B. Hannon, K. Limburg, S. Naeem, R. V. ONeill, J. Paruelo, R. G. Raskin, P. Sutton, and M. vandenBelt. The value of the world's ecosystem services and natural capital. *Nature*, 387(6630):253–260, 1997.

[12] A. G. Davies and C. Villaret. Eulerian drift induced by progressive waves above rippled and very rough beds. *Journal of Geophysical Research C: Oceans*, 104(C1):1465–1488, 1999.

[13] E. de Langre. Effects of wind on plants. *Annual Review of Fluid Mechanics*, 40:141–168, 2008.

[14] M. Denny and B. Gaylord. The mechanics of wave-swept algae. *Journal of Experimental Biology*, 205(10):1355–1362, 2002.

[15] M. Denny, B. Gaylord, B. Helmuth, and T. Daniel. The menace of momentum: Dynamic forces on flexible organisms. *Limnology and Oceanography*, 43(5):955–968, 1998.

[16] M. W. Denny, B. P. Gaylord, and E. A. Cowen. Flow and flexibility - ii. the roles of size and shape in determining wave forces on the bull kelp nereocystis luetkeana. *Journal of Experimental Biology*, 200(24):3165–3183, 1997.

[17] L. De Doncker, P. Troch, R. Verhoeven, K. Bal, P. Meire, and J. Quintelier. Determination of the manning roughness coefficient influenced by vegetation in the river aa and biebrza river. *Environmental Fluid Mechanics*, 9(5):549–567, 2009.

[18] L. De Doncker, P. Troch, R. Verhoeven, and K. Buis. Deriving the relationship among discharge, biomass and manning's coefficient through a calibration approach. *Hydrological Processes*, 25(12):1979–1995, 2011.

[19] J. G. Duan, R. H. French, and J. Miller. The lodging velocity for emergent aquatic plants in open channels. *Journal of the American Water Resources Association*, 38(1):255–263, 2002.

[20] C. Dunn, F. Lopez, and M. Garcia. Mean flow and turbulence in a laboratory channel with simulated vegetation. Technical Report 51, University of Illinois,, 1996.

[21] S. Enriquez, S. Agusti, and C. M. Duarte. Light absorption by seagrass posidonia oceanica leaves. *Marine Ecology Progress Series*, 86:201–204, 1992.

[22] J. Finnigan. Turbulence in plant canopies. *Annual Review of Fluid Mechanics*, 32:519–571, 2000.

[23] M. S. Fonseca. *Exploring the basis of pattern expression in seagrass landscapes*, 1998.

[24] M. S. Fonseca and S. S. Bell. Influence of physical setting on seagrass landscapes near beaufort, north carolina, usa. *Marine Ecology Progress Series*, 171:109–121, 1998.

[25] M. S. Fonseca and J. A. Cahalan. A preliminary evaluation of wave attenuation by four species of seagrass. *Estuarine, Coastal and Shelf Science*, 35(6):565–576, 1992.

[26] M. S. Fonseca and J. S. Fisher. A comparison of canopy friction and sediment movement between four species of seagrass with reference to their ecology and restoration. *Marine Ecology Progress Series*, 29:15–22, 1986.

[27] M. S. Fonseca, J. S. Fisher, J. C. Zieman, and G. W. Thayer. Influence of the seagrass, zostera-marina l, on current flow. *Estuarine Coastal and Shelf Science*, 15(4):351–364, 1982.

[28] M. S. Fonseca and W. J. Kenworthy. Effects of current on photosynthesis and distribution of seagrasses. *Aquatic Botany*, 27(1):59–78, 1987.

[29] M. S. Fonseca, J. C. Zieman, G. W. Thayer, and J. S. Fisher. The role of current velocity in structuring eelgrass (zostera marina l.) meadows. *Estuarine, Coastal and Shelf Science*, 17(4):367–380, 1983.

[30] Mark S. Fonseca, M. A. R. Koehl, and Blaine S. Kopp. Biomechanical factors contributing to self-organization in seagrass landscapes. *Journal of experimental marine biology and ecology*, 340(2):227–246, 2007.

[31] J. Fredsoe and R. Deigaard. 1992.

[32] M. Ghisalberti and H. Nepf. Mass transport in vegetated shear flows. *Environmental Fluid Mechanics*, 5(6):527–551, 2005.

[33] M. Ghisalberti and H. M. Nepf. Mixing layers and coherent structures in vegetated aquatic flows. *Journal of Geophysical Research C: Oceans*, 107(C2), 2002.

[34] M. Ghisalberti and H. M. Nepf. The limited growth of vegetated shear layers. *Water Resources Research*, 40(7):W07502, 2004.

[35] Marco Ghisalberti and Heidi Nepf. The structure of the shear layer in flows over rigid and flexible canopies. *Environmental Fluid Mechanics*, 6(3):277–301, 2006.

[36] Frederick Gosselin, Emmanuel de Langre, and Bruno A. Machado-Almeida. Drag reduction of flexible plates by reconfiguration. *Journal of Fluid Mechanics*, 650:319–341, 2010.

[37] J. M. R. Graham. The forces on sharp-edged cylinders in oscillatory flow at low keulegan-carpenter numbers. *Journal of Fluid mechanics*, 97(3):331–346, 1980.

[38] J. C. Green. Comparison of blockage factors in modelling the resistance of channels containing submerged macrophytes. *River Research and Applications*, 21(6):671–686, 2005.

[39] J. C. Green. Further comment on drag and reconfiguration of macrophytes. *Freshwater Biology*, 50(12):2162–2166, 2005.

[40] J. C. Green. Effect of macrophyte spatial variability on channel resistance. *Advances in Water Resources*, 29(3):426–438, 2006.

[41] D. L. Harder, O. Speck, C. L. Hurd, and T. Speck. Reconfiguration as a prerequisite for survival in highly unstable flow-dominated habitats. *Journal of plant growth regulation*, 23(2):98–107, 2004.

[42] C. L. Hurd. Water motion, marine macroalgal physiology, and production. *Journal of Phycology*, 36(3):453–472, 2000.

[43] Fredrik Huthoff, Denie C. M. Augustijn, and Suzanne J. M. H. Hulscher. Analytical solution of the depth-averaged flow velocity in case of submerged rigid cylindrical vegetation. *Water Resources Research*, 43(6):W06413, 2007.

[44] Eduardo Infantes, Alejandro Orfila, Jorge Terrados, Gonzalo Simarro, Mitul Luhar, and Heidi M. Nepf. Effect of a seagrass (posidonia oceanica) meadow on wave propagation. *Marine Ecology Progress Series*, 456:63–72, 2012.

[45] Eduardo Infantes, Jorge Terrados, Alejandro Orfila, Bartomeu Canellas, and Amaya Alvarez-Ellacuria. Wave energy and the upper depth limit distribution of posidonia oceanica. *Botanica Marina*, 52(5):419–427, 2009.

[46] J. L. Kemp, D. M. Harper, and G. A. Crosa. The habitat-scale ecohydraulics of rivers. *Ecological Engineering*, 16(1):17–29, 2000.

[47] G. H. Keulegan and L. H. Carpenter. Measurement of the velocity-profile in and above a forest of laminaria hyperborea. *Journal of Research of the National Bureau of Standards*, 60(5):423–440, 1958.

[48] N. Kobayashi, A. W. Raichle, and T. Asano. Wave attenuation by vegetation. *Journal of Waterway, Port, Coastal, and Ocean Engineering - ASCE*, 119(1):30–48, 1993.

[49] E. W. Koch and G. Gust. Water flow in tide- and wave-dominated beds of the seagrass thalassia testudinum. *Marine Ecology Progress Series*, 184:63–72, 1999.

[50] Nicholas Kouwen, Tharakkal E. Unny, and H. M. Hill. Flow retardance in vegetated channels. *Journal of the Irrigation and Drainage Division*, 95(2):329–342, 1969.

[51] P. K. Kundu and I. M. Cohen. *Fluid Mechanics*, 2004.

[52] A. F. Lightbody and H. M. Nepf. Prediction of velocity profiles and longitudinal dispersion in emergent salt marsh vegetation. *Limnology and Oceanography*, 51(1):218–228, 2006.

[53] D. Liu, P. Diplas, J. D. Fairbanks, and C. C. Hodges. An experimental study of flow through rigid vegetation. *Journal of Geophysical Research F: Earth Surface*, 113(F4):F04015, 2008.

[54] M. S. Longuet-Higgins. Mass transport in water waves. *Philosophical Transaction of the Royal Society of London. A*, 245(903):535–581, 1953.

[55] R. J. Lowe, J. R. Koseff, and S. G. Monismith. Oscillatory flow through submerged canopies: 1. velocity structure. *Journal of Geophysical Research C: Oceans*, 110(C10016), 2005.

[56] M. Luhar, S. Coutu, E. Infantes, S. Fox, and H. Nepf. Wave-induced velocities inside a model seagrass bed. *Journal of Geophysical Research C: Oceans*, 115(C12005), 2010.

[57] M. Luhar and H. M. Nepf. From the blade scale to the reach scale: A characterization of aquatic vegetative drag. *Advances in Water Resources*, 2012.

[58] Mitul Luhar and Heidi M. Nepf. Flow-induced reconfiguration of buoyant and flexible aquatic vegetation. *Limnology and Oceanography*, 56(6):2003–2017, 2011.

[59] Mitul Luhar, Jeffrey Rominger, and Heidi Nepf. Interaction between flow, transport and vegetation spatial structure. *Environmental Fluid Mechanics*, 8(5-6):423–439, 2008.

[60] O. S. Madsen. On the generation of long waves. *Journal Geophysical Research*, 76(36):8672–8683, 1971.

[61] N. Marb, C. M. Duarte, J. Cebrian, M. E. Gallegos, B. Olesen, and K. Sand-Jensen. Growth and population dynamics of posidonia oceanica on the spanish mediterranean coast: Elucidating seagrass decline. *Marine Ecology Progress Series*, 137(1-3):203–213, 1996.

[62] F. Marin. Eddy viscosity and eulerian drift over rippled beds in waves. *Coastal Engineering*, 50(3):139–159, 2004.

[63] Tali Mass, Amatzia Genin, Uri Shavit, Mor Grinstein, and Dan Tchernov. Flow enhances photosynthesis in marine benthic autotrophs by increasing the efflux of oxygen from the organism to the water. *Proceedings of the National Academy of Sciences of the United States of America*, 107(6):2527–2531, 2010.

[64] C. C. Mei, M. Stiassnie, and D. K. P Yue. *Theory and Applications of Ocean Surface Waves*, 2005.

[65] D. G. Meijer. Modelproeven overstroomde vegetatie. Technical Report PR121, HKV Consultants, 1998.

[66] D. G. Meijer and E. H. van Velzen. Prototype-scale flume experiments on hydraulic roughness of submerged vegetation. Technical report, HKV Consultants, 1998.

[67] F. J. Mendez and I. J. Losada. An empirical model to estimate the propagation of random breaking and nonbreaking waves over vegetation fields. *Coastal Engineering*, 51(2):103–118, 2004.

[68] F. J. Mendez, I. J. Losada, and M. A. Losada. Hydrodynamics induced by wind waves in a vegetation field. *Journal of Geophysical Research C: Oceans*, 104(C8):18383–18396, 1999.

[69] K. A. Moore. Influence of seagrasses on water quality in shallow regions of the lower chesapeake bay. *Journal of Coastal Research*, 20(Special Issue 45):162–178, 2004.

[70] E. Murphy, M. Ghisalberti, and H. Nepf. Model and laboratory study of dispersion in flows with submerged vegetation. *Water Resources Research*, 43(5):W05438, 2007.

[71] H. Nepf, M. Ghisalberti, B. White, and E. Murphy. Retention time and dispersion associated with submerged aquatic canopies. *Water Resources Research*, 43(4), 2007.

[72] H. M. Nepf. Flow and transport in regions with aquatic vegetation. *Annual Review of Fluid Mechanics*, 44:123–142, 2012.

[73] Iehisa Nezu and Michio Sanjou. Turburence structure and coherent motion in vegetated canopy open-channel flows. *Journal of Hydro-Environment Research*, 2(2):62–90, 2008.

[74] V. Nikora. Hydrodynamics of aquatic ecosystems: an interface between ecology, biomechanics and environmental fluid mechanics. *River Research and Applications*, 26(4):367–384, 2010.

[75] Vladimir Nikora, Scott Lamed, Nina Nikora, Koustuv Debnath, Glenn Cooper, and Michael Reid. Hydraulic resistance due to aquatic vegetation in small streams: Field study. *Journal of Hydraulic Engineering-ASCE*, 134(9):1326–1332, 2008.

[76] D. Poggi, A. Porporato, L. Ridolfi, J. D. Albertson, and G. G. Katul. The effect of vegetation density on canopy sub-layer turbulence. *Boundary-Layer Meteorology*, 111(3):565–587, 2004.

[77] M. Raupach, J. Finnigan, and Y. Brunet. Coherent eddies and turbulence in vegetation canopies: The mixing-layer analogy. *Boundary-Layer Meteorology*, 60:375–395, 1996.

[78] W. O. Ree. Hydraulic characteristics of vegetation for vegetated waterways. *Agricultural Engineering*, 30:184–189, 1949.

[79] Jeffrey T. Rominger and Heidi M. Nepf. Flow adjustment and interior flow associated with a rectangular porous obstruction. *Journal of Fluid Mechanics*, 680:636–659, 2011.

[80] K. Sand-Jensen. Drag and reconfiguration of freshwater macrophytes. *Freshwater Biology*, 48(2):271–283, 2003.

[81] T. Sarpkaya and M. Isaacson. Mechanics of wave forces on offshore structures. 1981.

[82] T. Sarpkaya and J. L. O'Keefe. Oscillating flow about two- and three-dimensional bilge keels. *Journal of Offshore Mechanics and Arctic Engineering*, 118:1–6, 1996.

[83] K. E. Sawaya, L. G. Olmanson, N. J. Heinert, P. L. Brezonik, and M. E. Bauer. Extending satellite remote sensing to local scales: land and water resource monitoring using high-resolution imagery. *Remote Sensing of Environment*, 88(1-2):144–156, 2003.

[84] L. Schouveiler, C. Eloy, and P. Le Gal. Flow-induced vibrations of high mass ratio flexible filaments freely hanging in a flow. *Physics of Fluids*, 17(4):047104, 2005.

[85] J. Schutten, J. Dainty, and A. J. Davy. Root anchorage and its significance for submerged plants in shallow lakes. *Journal of Ecology*, 93(3):556–571, 2005.

[86] Y. Shimizu and T. Tsujimoto. Numerical analysis of turbulent open-channel flow over vegetation layer using a k-e turbulence model. *Journal of Hydroscience and Hydraulic Engineering*, 11(2):57–67, 1994.

[87] Bernhard Statzner, Nicolas Lamouroux, Vladimir Nikora, and Pierre Sagnes. The debate about drag and reconfiguration of freshwater macrophytes: comparing results obtained by three recently discussed approaches. *Freshwater Biology*, 51(11):2173–2183, 2006.

[88] H. L. Stewart. Hydrodynamic consequences of maintaining an upright posture by different magnitudes of stiffness and buoyancy in the tropical alga turbinaria ornata. *Journal of Marine Systems*, 49(1-4):157–167, 2004.

[89] H. L. Stewart. Morphological variation and phenotypic plasticity of buoyancy in the macroalga turbinaria ornata across a barrier reef. *Marine Biology*, 149(4):721–730, 2006.

[90] J. Stoer and R. Bulirsch. *Introduction to Numerical Analysis*. 1980.

[91] B. M. Stone and H. T. Shen. Hydraulic resistance of flow in channels with cylindrical roughness. *Journal of Hydraulic Engineering-ASCE*, 128(5):500–506, 2002.

[92] A. Sukhodolov. Comment on drag and reconfiguration of macrophytes. *Freshwater Biology*, 50(1):194–195, 2005.

[93] Alexander N. Sukhodolov and Tatiana A. Sukhodolova. Case study: Effect of submerged aquatic plants on turbulence structure in a lowland river. *Journal of Hydraulic Engineering-ASCE*, 136(7):434–446, 2010.

[94] Michal Tal and Chris Paola. Dynamic single-thread channels maintained by the interaction of flow and vegetation. *Geology*, 35(4):347–350, 2007.

[95] Yukie Tanino and Heidi M. Nepf. Laboratory investigation of mean drag in a random array of rigid, emergent cylinders. *Journal of Hydraulic Engineering-ASCE*, 134(1):34–41, 2008.

[96] S. Temmerman, T. J. Bouma, J. Van de Koppel, D. Van der Wal, M. B. De Vries, and P. M. J. Herman. Vegetation causes channel erosion in a tidal landscape. *Geology*, 35(7):631–634, 2007.

[97] F. I. M. Thomas and C. D. Cornelisen. Ammonium uptake by seagrass communities: Effects of oscillatory versus unidirectional flow. *Marine Ecology Progress Series*, 247:51–57, 2003.

[98] S. Vogel. *Life in moving fluids.* Princeton University Press, Princeton, NJ, 2nd edition, 1994.

[99] Yeqiao Wang, Michael Traber, Bryan Milstead, and Sara Stevens. Terrestrial and submerged aquatic vegetation mapping in fire island national seashore using high spatial resolution remote sensing data. *Marine Geodesy*, 30(1-2):77–95, 2007.

[100] Brian L. White and Heidi M. Nepf. Shear instability and coherent structures in shallow flow adjacent to a porous layer. *Journal of Fluid Mechanics*, 593:1–32, 2007.

[101] F. C Wu, H. W. Shen, and Y. J Chou. Variation of roughness coefficients for unsubmerged and submerged vegetation. *Journal of Hydraulic Engineering*, 125(9):934–941, 1999.

[102] J. Yan. Experimental study of flow resistance and turbulence characteristics of open channel flow with vegetation, 2008.

[103] W. Yang. Experimental study of open-channel flows with submerged vegetation, 2008.

[104] C. Y. Zhou and J. M. R. Graham. A numerical study of cylinders in waves and currents. *Journal of Fluids and Structures*, 14(3):403–428, 2000.

[105] R. C. Zimmerman. A biooptical model of irradiance distribution and photosynthesis in seagrass canopies. *Limnology and Oceanography*, 48(1):568–585, 2003.